MReadings
Prostate MRI
Contributions from our MAGNETOM users

Not for distribution in the US

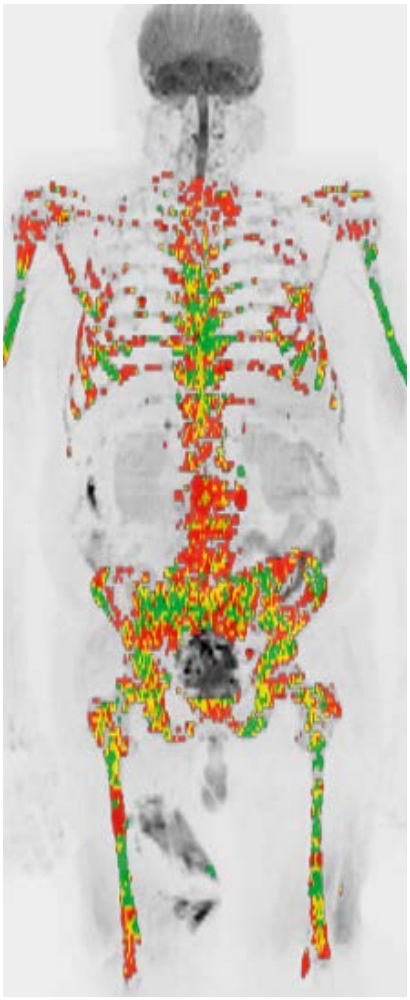

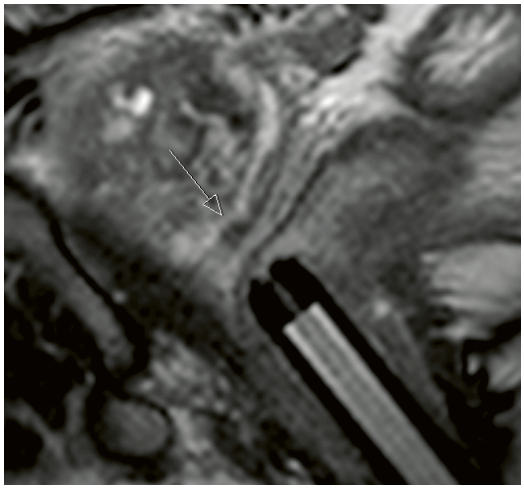

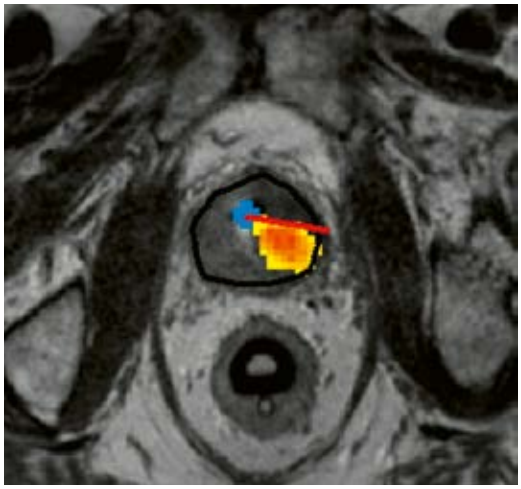

SIEMENS Healthineers

Dear Reader,

Throughout the first decade of the 21st century, MRI was anecdotally heralded as a problem solver in the management of patients with prostate cancer. This is especially true for those who have undergone multiple biopsies and still have increasing PSA levels. However, the examinations were long, and typically involved the use of endorectal coils, and MR spectroscopic techniques. In addition, and perhaps most crucial, there was no generally agreed reporting standard.

With compelling evidence building up over recent years, the release of clear, international recommendations for standardized reading and reporting, as well as bold advances in MR hardware and sequence development, everything has changed. Today, we see the coming of age of MRI in the management of prostatic disease.

MR imaging can help detect or exclude clinically significant prostate cancer with excellent predictive value. It is routinely used by urologists for guiding biopsies for better disease stratification and optimized treatment selection. MR imaging could also play a remarkable future role in the manage-ment of patients with known localized and advanced prostate disease.

This volume of *MReadings* highlights the role of MRI in the management of suspected disease, presents options for image-guided biopsies, while also focusing on the emerging field of 'next-generation imaging' with the aim of providing the right treatment to the right patient at the right time within the framework of precision oncology.

We are grateful to the authors for sharing their expertise, experience, and enthusiasm with other MAGNETOM users.

I wish you an enjoyable read!

Gregor Thörmer, Ph.D.
Global Segment Manager
MR Imaging in Oncology

Content

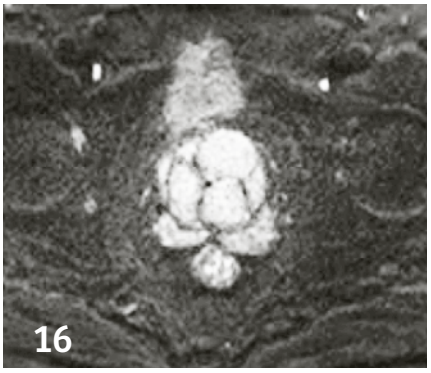

DWI using RESOLVE at 3T

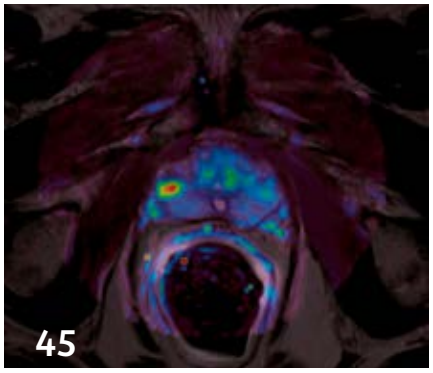

MR-guided biopsies of the prostate

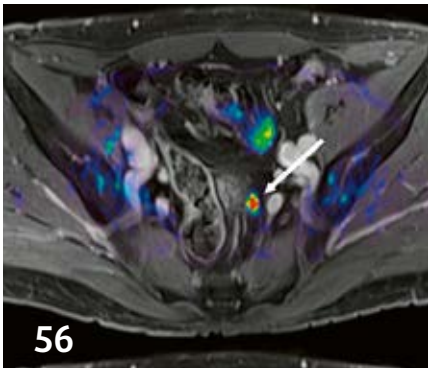

PET/MRI with PSMA-Ligands

Diagnostic Imaging. Detection

MR-guided Intervention. Treatment

Management of Advanced Stages of Prostate Cancer

[1] *syngo*.via Frontier is for research only, not a medical device.

Prostate Cancer – Meeting Clinical Needs by Advanced MRI at Diagnosis and on Follow-Up

Dr. Anwar R. Padhani, M.D.[1,2]; Dr. Clare Allen, M.D.[3]

[1] Paul Strickland Scanner Centre, Mount Vernon Cancer Centre, Northwood, Middlesex, United Kingdom
[2] Synarc Inc., San Francisco, CA, USA
[3] Department of Imaging, University College Hospital, London, United Kingdom

Introduction

Carcinoma of the prostate is the commonest form of human carcinoma, found at autopsy in 30% of men at the age of 50 and in over 80% of men in their 90s. Worldwide, more than 650,000 men are diagnosed with the disease each year accounting for a 10th of all new male cancers. In Europe, the lifetime risk of being diagnosed with prostate cancer is approximately 1 in 13. In 2006, an estimated 234,460 American men were newly diagnosed with prostate cancer, and over 30,000 died of the disease. There is a close association between recent increases in the incidence of prostate cancer and the use of transurethral resection of the prostate (TURP) for treating obstructive lower urinary tract symptoms due to presumed benign prostatic hyperplasia (BPH) and more recently with serum prostatic serum antigen (PSA) testing. Whether there is a real increase in incidence or not, the number of cases of prostate cancer will rise further as the population at risk (older men) grows with lengthening of life expectancy. With the increased use of PSA testing, it has been noted that there has been a gradual downward stage migration (increased incidence of early disease) with the discovery of carcinomas that are possibly not life threatening. Prostate carcinoma thus represents a significant challenge for men's health. This fact has been recently recognized by the US Congress with the recent introduction of the Prostate Research Imaging and Men's Education (PRIME) act. This act, the first to directly support imaging technologies and *in vivo* diagnostics for the detection, diagnosis and treatment of prostate cancer, seeks to authorise an investment of USD 600 million over five years to combat this deadly disease with related educational efforts to raise public awareness. There are considerable limitations in current diagnostic and therapy pathways for prostate cancer patients. Only moderate tumor and nodal staging accuracies of imaging tests has resulted in the patchy adoption of MRI into routine patient management particularly at new diagnosis. The fact that prostate cancer is often multicentric and poorly depicted by non-invasive tests has resulted in whole organ rather than specific tumor-directed therapy. With downward stage migration, it is increasingly unclear whether it is necessary to actively treat all diagnosed cases. There is debate on what constitutes clinically important disease encapsulated by the disparity between the approximate 30–40% prevalence of histological prostate cancer in men older than 50 years of age and the 8% of cancers that become clinically significant or the 3% lifetime risk for death from this disease. Since therapies are not without their sometimes devastating complications, there is increasing patient pressure for more minimally invasive and more effective therapeutic approaches. In this context it is clear that focal ablations (so-called "male lumpectomy") will play increasingly important management roles (examples include photodynamic therapy (PDT), cryotherapy, high-intensity focused ultrasound (HIFU) and high-dose rate brachytherapy). The usage and future success of these treatments will depend on the identification of clinically significant focal disease (the dominant intra-prostatic lesion (DIL) also called index lesion and the absence of extra prostatic disease (see box for additional clarification of these terms). Additionally, new therapeutic approaches include prophylactic nodal radiotherapy with the intensity modulation (IMRT) require the accurate mapping of the location of pelvic lymph nodes for the eradication of metastases. In the future, patient therapy will be more personalized taking into consideration not only the extent of local disease but also assessments of biological aggressiveness as well as patient and physician preferences. It is in these contexts that this paper describes the current and future roles of MRI in prostate cancer patient management. The approach is from the perspective of the patient pathway describing clinical and research requirements at each stage and the authors' opinions on the roles of morphological and functional imaging in order to overcome current bottlenecks in prostate cancer management. The opinions expressed represent the views of the authors based on literature reviews and personal experiences. Recommendations given are partly dependent on our subjective assessments of ease of imaging acquisition, analysis and interpretations.

Roles and current limitations of MRI in clinical practice

From the outset it should be recognised that MRI for newly diagnosed cancer patients is not universally accepted nor used. However, the majority of urological surgeons and

Terminology

Localised prostate cancer can be stratified into risk groups using combinations of clinical findings, histopathology using the Gleason grading system and presenting serum prostate specific antigen level (PSA). General risk categories for prostate cancer are given in table 1. Many readers will be unfamiliar with some of the terminology pertaining to prostate cancer management. These concepts are used in different ways by clinicians and pathologists and the authors' current understanding of these terms is as follows:

Dominant intraprostatic lesion (DIL) also called Index lesion: This is a vague term used in the radiotherapy/ surgical literature referring to the major focus of disease in terms of tumor volume, the goal being to focally ablate these regions as part of whole prostate gland therapy.

Clinically insignificant disease: Small-volume prostate cancers (usually 0.5 ml or less) without elements of Gleason grade pattern 4 or 5. By definition these tumors are non-palpable and confined to the prostate gland.

However, since many prostate cancer deaths occur more than 10 years after the initial diagnosis, the biological behavior of small-volume prostate cancers may become important in patients with relatively long post-diagnosis life expectancies.

Clinically significant disease in non-palpable (T1c) prostate cancer: These tumors are often risk stratified by well-established prognostic factors (Gleason score [GS], pretreatment serum PSA level, and percent positive biopsy findings [% + Bx]) because these factors predict biological aggressiveness. High risk: GS = 8–10 or PSA level > 20 ng/mL; or GS = 7 or PSA level > 10–20 ng/mL and > 50% + Bx – these patients have a historical four-year PSA control of 10% to 30% after definitive therapy. Intermediate risk: GS = 7, PSA level > 10–20 ng/mL, and 34%–50% + Bx. These patients have a historical four-year PSA control of 50% to 60% after definitive therapy. Significant disease can also be based on age and GS. Antiticipated prostate cancer mortality greater than 30% to 50% also includes patients with GS = 7 and age 70 years, and GS = 6 and age 65 years.

radiotherapists agree that the following patients should have MRI at first diagnosis:

1. Symptomatic patients: MRI has an important contributing role in determining tumor extent, detecting complications and planning treatment.
2. Patients at higher risk of local / metastatic spread: a current consensus definition of risk groups for prostate cancer patients is given in table 1.
3. Potential surgical candidates where Partin tables suggest the risk of extra-prostatic disease (level of risk is debated but probably > 30% – depending on radiological expertise).
4. Patients with palpable apical tumors.Patients with advanced or metastatic disease need not always undergo detailed local staging with MRI.

It is to be noted that clinical requirements change at various points of the prostate cancer patient's journey and questions for MRI to address are correspondingly altered (Table 2). So for example when MRI is used for newly diagnosed patients, the objectives for its usage are:

1. To delineate the intra- and extra-prostatic extent of the local disease. Here, the key first distinction is organ confinement versus extra-prostatic disease.
2. Prostatic cancer is often multifocal, and the detection of the dominant prostatic cancer nodule or index lesion is becoming important for therapy planning (for definition see box).
3. To detect the presence of cancer at the prostatic apex; this is an important consideration for patients being considered for surgical therapy.
4. To detect the presence and location (intra- versus extra-pelvic) of metastatic nodal involvement.
5. To detect the presence of bone metastases.
6. To detect the presence of complications of urinary tract obstruction.

Years of experience show that morphological (T2-weighted) MRI has many limitations for the evaluation of the prostate gland. We have come to recognize that tumor volume and distribution is often underestimated because not all tumors are visible and small tumors are not consistently shown. Confounding effects occur because there are other causes of low signal intensity in the peripheral gland (scars, prostatitis, haemorrhage and therapy effects) and central gland tumors can be particularly difficult to see in the presence of benign prostate hyperplasia (BPH). Conventionally it was thought that these were unimportant limitations as key therapeutic decisions were based on tumor extent (simply organ confinement or not) but we know that MRI also has a restricted ability to distinguish organ confined disease from early T3 disease resulting in great staging variability from center to center. Furthermore the clinical situation has changed because it is now increasingly important to depict the index lesion/DIL for the application of minimally invasive treatments which may (or may not) be used in combination with conventional approaches. As we move into the arena of personalised patient-oriented therapy, imaging assess-

Low Risk	T1-T2a and Gleason Score 2–6 and PSA < 10 ng/ml
Intermediate Risk[1]	T2b-T2b or Gleason Score 7 or PSA 10–20 ng/ml
High Risk[1]	T3a or Gleason Score 8–10 or PSA > 20 ng/ml

Table 1: UK National Comprehensive Cancer Network (NCCN) definitions of risk for prostate cancer (2005)

[1]Patients with multiple adverse factors may be shifted into the next higher group. Note: T3a/b and T4 disease is not organ confined.

Clinical Journey begins here	Suspect cancer	Stage known cancer	Treatment of initial disease[1]					Monitoring effectiveness of therapy	Surveillance of treated disease	Suspect relapse	Treatment of relapsed disease	
			Initial observation (deferred therapy)	Curative intent			Palliative				Local salvage	Palliative
				Surgery	Ablative therapies (HIFU, PDT, cryotherapy, brachytherapy)	External beam radiotherapy to prostate ± pelvic nodes						
Clinical scenario	Raised PSA with negative biopsy TRUS and or biopsies	Cancer diagnosed and confirmed by biopsy	Small volume Low aggressiveness	Organ confinement No tumor at prosatic apex No metastases	Organ confinement No metastases	Usually includes neo adjuvant hormones	Usually hormonal therapy ± RT	Usually after focal therapies	Rare to use imaging in this role (Serum PSA surveillance)	Significant rise in serum PSA	Disease is localised and salvage is possible	Disease is not localised and salvage is impossible
Clinical (C) or Research (R) requirements	Define tumor location and size for targeted biopsy (C)	TNM stage (C) Define dominant lesion (C) Define lesion aggressiveness (C/R) Therapy planning (C)	Confirm organ confinement (C) Document size (C) Depict lesion aggressiveness (C/R)	Detect adverse features (C) Target pelvic nodal dissection (C)	Define dominant lesion location and size (C/R)	Confirm confinement to pelvis (C) Nodal mapping (C/R)	Define extent of modal & distant metastases (C) Requirements for local palliation (C)	Treatment verfication (R) Define volume and extent of residual disease (R)	Detect active disease in absence of significant PSA rise (R)	Identify site and volume of recurrence (C)	Define extent of local disease and absence of metastases (C)	Define extent of relapsed disease and complications (C) Requirements for local metastases (C)
Contribution made by MRI[2]												
Morphology	+++	+++	+++	+++	+++	+++	++	+++	++	+++	+++	+++
Additional MRI biopsy	+	0	+	0	0	0	0	+	+	++	++	0
Lymphography	0	++	+++	+++	+++	+++	+	0	0	++	++	0
MRSI	+++	+	++	++	+	+	+	0	+++	++	+	0
DW-MRI	+++	++	+++	++	++	++	+	+	++	+++	++	0
Data fusion	++	++	+	++	++	++	0	0	+	+	++	0
DCE-MRI	+++	+	+++	++	+	+	0	+++	+++	+++	+++	0
BOLD-MRI	0	+	0	0	+	+	+	+	0	+	0	0

Table 2: The prostate cancer patient journey and contribution of MRI in patient care

[1] The imaging recommendations are for the purpose of planning therapy.
[2] These authors' opinions are based on literature reviews, personal experiences and recommendations are partly dependent on subjective assessments of ease of imaging data acquisition, analysis and interpretations.
0 = No requirement; + = possible requirement; ++ = probably indicated; +++ = definite indication

ments will need to become more comprehensive and accurate, depicting not only the extent of local disease but also assessing biological aggressiveness (by depicting tumor grade other biological important features such as the presence and extent of tumor hypoxia, increased vascularisation and proliferation rate). Beyond local tumor assessments, our current ability to accurately depict nodal metastatic disease is also limited by the use of morphol-ogical criteria based mainly on size evaluations. There is a high incidence of reactive pelvic lymph node enlargement and it is well described that adenocarcinoma prostate metastases are of small volume (microscopic) and therefore may be found in normal sized lymph nodes. There is a high incidence of nodal spread to surgically non-sampled sites at pelvic lymph node dissection (PLND). Therefore future assessments of prostate cancer patients will also include more accurate depiction of the presence and extent of nodal metastatic disease.

Overcoming limitations with advanced MRI techniques

Over recent years tremendous experience has been gained in functional MRI techniques and it is becoming increasingly clear that they may be able to address some of the bottlenecks in prostate cancer patient management. New techniques which include dynamic contrast enhanced MRI (DCE-MRI), diffusion-weighted MR imaging (DW-MRI), proton MR spectroscopic imaging (MRSI) and blood oxygen level dependent MR imaging (BOLD-MRI) are making the transition from academic investigation to routine clinical usage. The progress made by each technique in the transition to clinical practice varies, but important lessons on their potential uses and limitations are known. With the advent of faster sequences performed on high-performance, high field strength MRI scanners it is possible to combine morphological and multiple functional prostatic imaging into a more comprehensive evaluation with only a small additional time penalty. Since the limitations of each technique are often non-overlapping it is recommended that multiple functional imaging techniques are used for making diagnoses and therapeutic decisions at various stages of the clinical cancer journey as recommended in tables 2 and 3. The biological basis of observations on these techniques is discussed briefly with appropriate references for interested readers. Examples of multifunctional imaging use in clinically suspected cancer at diagnosis and after definitive treatment are shown in the figures. **Dynamic contrast enhanced MRI** (DCE-MRI) using small molecular weight gadolinium chelates enables non-invasive imaging characterization of prostatic vascularity. Established clinical roles in prostate gland include lesion detection and localization, for tumor staging and for the detection of suspected tumor recurrence [1]. **Diffusion-weighted MRI** (DW-MRI) is a technique that displays information about the extent and direction of random water motion in tissues. DW-MRI provides information on extracellular space tortuosity, tissue cellularity and the integrity of cellular membranes. Clinical data indicates a number of potential roles in prostate cancer including lesion localisation and characterisation and determination of the lesion aggressiveness [2]. Diffusion MRI images should always be interpreted by integration of morphology, high b-value (> 750 sec/mm^2) signal appearances and on ADC maps. This is because the calculated ADC values are dependent on the range of b-values used with additional errors arising from noise in very high b-value images. **MR spectroscopic imaging** (MRSI) of the prostate depicts the altered metabolism associated with prostate cancer. Normal prostatic glandular tissues shows high citrate levels whereas prostate cancer is characterised by high levels of choline. Studies to date suggest that MRSI might provide information that could be used to increase staging accuracy for less experienced readers and thereby reduce inter-observer variability, improve the non-invasive assessment of tumor location (although a recent American College of Radiology Imaging Network (ACRIN) study was inconclusive) and provides guidance for directing biopsies and focal therapies [3, 4]. The primary source of image contrast on **Blood Oxygen Level Dependent** MRI is endogenous, para-magnetic deoxyhaemoglobin which increases the transverse relaxation rate (R2*) of water in blood and surrounding tissues and thus BOLD-MRI is sensitive to pO2 within and in tissues adjacent to perfused vessels. BOLD-MRI does not measure pO2 directly and in order to be able to correctly interpret BOLD images it is necessary to know or to deter-mine the distribution of blood volume in tissues. Recent data suggests that BOLD-MRI can be used to generate probability biomaps of prostate tumor hypoxia and when combined with DW-MRI and DCE-MRI may be used to target hypoxic prostate tumor regions with focal therapies such as high dose rate brachytherapy, cryotherapy as well as HIFU [5, 6]. **MR lymphography** using the intravenously administered contrast agent Ferumoxatan-10 has emerged as a powerful new tool for the evaluation of nodal involvement. Much research attesting to its accuracy for nodal characterisation (including the detection of micrometastases) has appeared in the literature, although efficacy data relating to changing patient management and altering clinical outcomes remains generally lacking [7, 8]. Approval of this contrast agent in Europe is expected soon. Two basic strategies have been explored for **MRI guided prostate gland biopsy**:

1. Co-registration of previously acquired diagnostic MR imaging to interventional TRUS or open scanner MR images, and
2. stereotactic needle interventions within conventional diagnostic scanners using careful patient positioning or the aid of simple manipulators. Such techniques can be used for needle-based interventions for prostate cancer, including biopsy, brachytherapy, and thermal therapy.

Figure 1: Rising PSA levels with repeated negative TRUS biopsies.
This 56-year-old male patient had 3 negative transrectal ultrasound (TRUS) guided biopsies for rising serum PSA levels over 2–3 years. In May 2006 the PSA level was 5.8 and now it had risen to 14.6 ng/ml. A multifunctional study was undertaken. Morphology, DW-MRI, DCE-MRI and MRSI examinations were all obtained within a 1-hour examination time on Siemens 1.5T MAGNETOM SATS – Symphony scanner with Tim (Total imaging matrix) capability using surface coils only. Evaluations of data obtained were done on Siemens Leonardo Workstation (MMWP) using Viewing, MRP with fusion, MeanCurve and Spectroscopy Taskcards.

Figure 1A: **Viewing TaskCard.**
Top-Left:
T2-weigthed image shows some low signal in the peripheral zone at the base of the prostate gland in the midline. No central gland abnormality is shown.
Top-right: ADC map (calculated from b-value 0t, 50t, 100t, 250t, 500t and 750t images) shows restricted diffusion in the left central gland measuring 1.3 cm (arrow).
Bottom-left: Fusion image (b 1200 trace + T2-weighted) with 50% opacity confirms that the restricted diffusion is co-located in the left central gland indicating high cellularity.

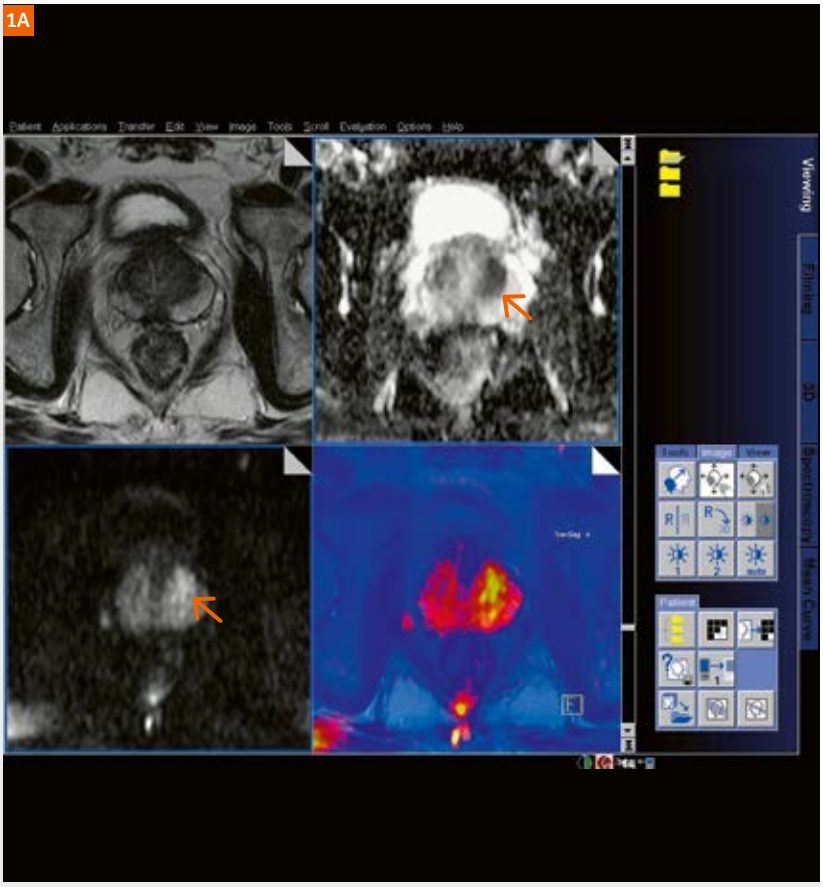

Figure 1B: MPR TaskCard.
Anatomical and functional images are co-localised using advanced, non-rigid software algorithms with false colour overlays of high b-value (b1200t) images. The TaskCard shows the prostate in 3 planes and indicates the site of high cellularity which can be used to indicate where to biopsy and can guide focal therapies.

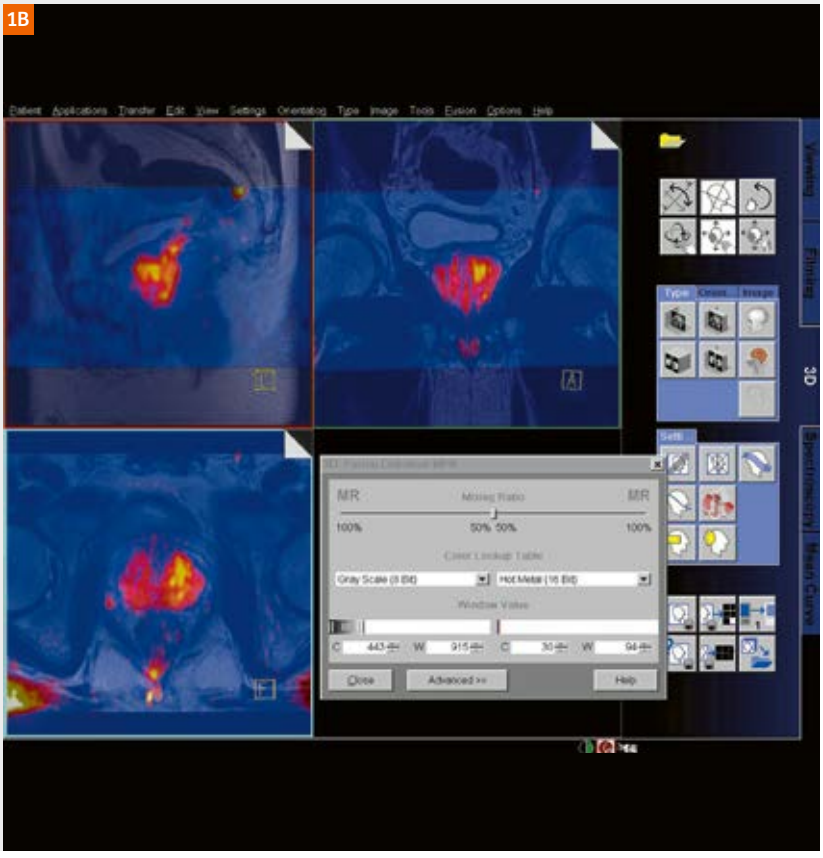

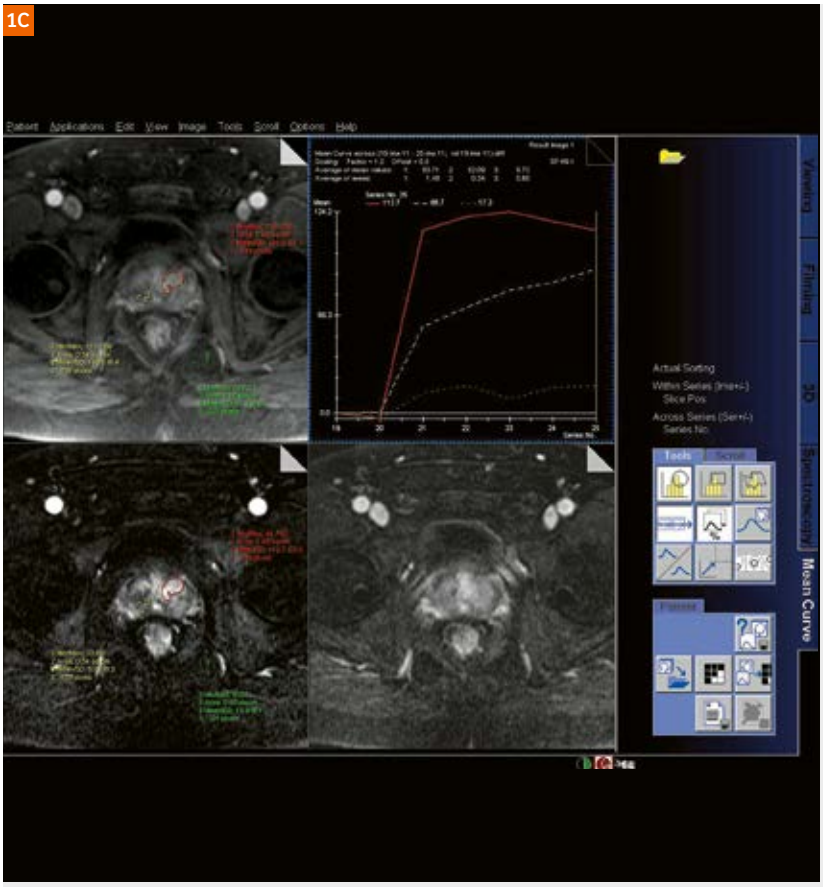

Figure 1C: The MeanCurve TaskCard can be used to analyze dynamic contrast enhanced images (DCE-MRI). High spatial resolution DCE-MRI data were acquired every 30 seconds (twice before and 5 times post 0.1 mmol/kg Gd-DTPA).
Top-left: Regions of interest (ROIs) are placed in the region of the restricted diffusion (red ROI), in the right peripheral zone (yellow ROI) and in ischio-rectal fat.
Top-Right: Graphic depiction of contrast-enhancement with time shows marked early enhancement of the mass in the left central zone with some wash-out (red line).
Bottom-left: Subtraction image depicts more clearly the enhancing regions and can be used to place ROIs.
Bottom-right: Late post contrast enhanced T1-weighted image with fat-suppression.
The area of high enhancement is difficult to see.

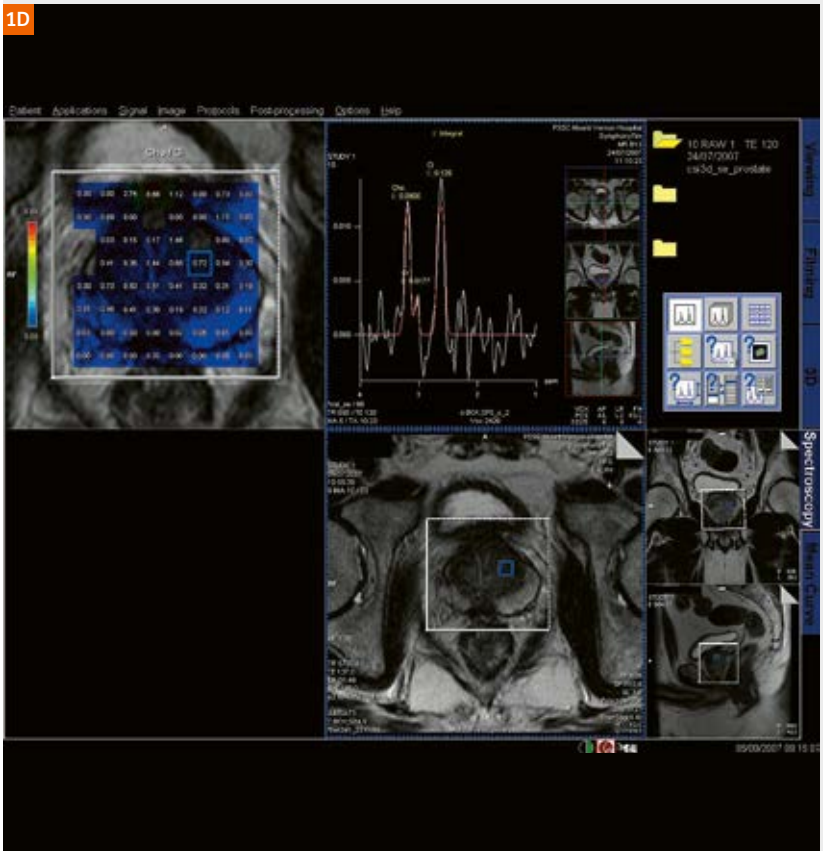

Figure 1D: Spectroscopy TaskCard.
MR spectroscopic imaging (5 x 5 mm voxel) from the left central gland lesion shows abnormal spectrum with high choline and low citrate levels (Choline: citrate ration: 0.72). The information obtained with these tools indicates a highly suspicious lesion suggestive of prostate cancer in the left central gland (mass, high cellularity, high perfusion and abnormal metabolism). This area was specifically targeted for biopsy and a cancer was diagnosed.

Figure 2: Tumor recurrence following radiotherapy
72-year old male patient with prostate cancer previously treated (4 years prior) with radiotherapy for prostate cancer for T3a/b disease but now with rising serum PSA levels (5.4 ng/ml).

Figure 2A:
Top-Left: T2-weighted image showing a 2 cm mass posterior arising from the peripheral gland of the prostate breaching the mesorectal fascia indenting but not invading the rectum.
Top-Right: ADC map (from b0-750t images) showing marked restriction of water diffusion in relation to the mass behind the prostate.
Bottom-right: b 1200 trace image shows hyperintensity of the tumor recurrence; note that the treated prostate gland is not hyperintense.
Bottom-left: Fusion image (b1200 trace + T2-weighted) with 50% opacity confirms that the restricted diffusion is co-located in the recurrent tumor.

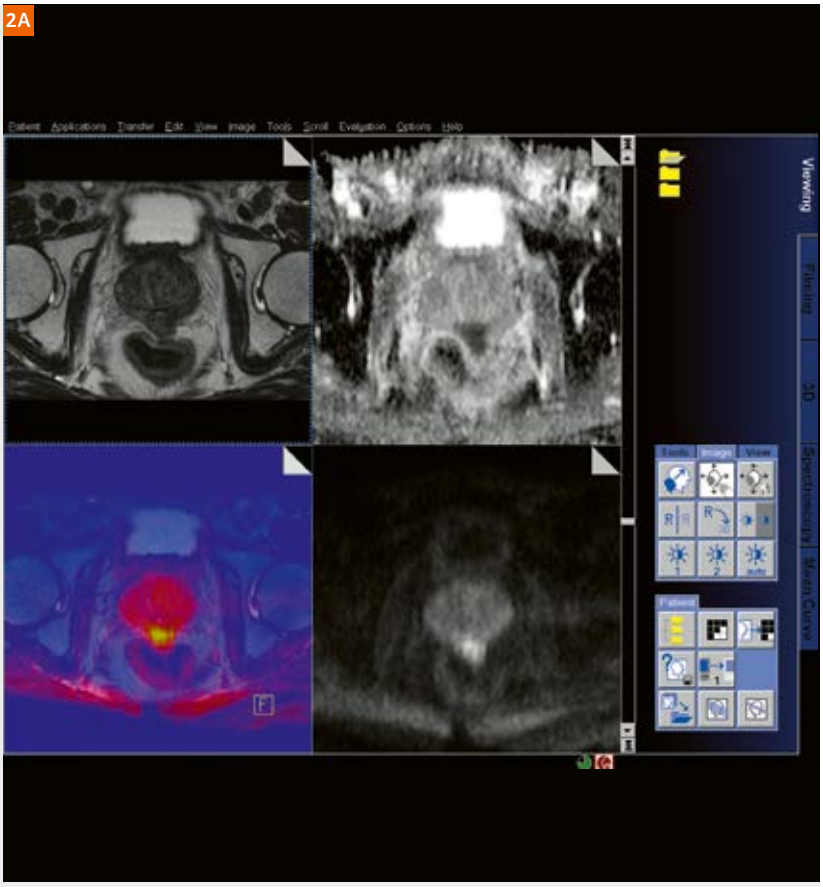

Figure 2B: Anatomical and functional imaging are co-localised using advanced, non-rigid software algorithms with color overlays of high b-value (b1200t) images in the **MPR TaskCard**. The opacity of the color overlays can be adjusted to optimise data display.

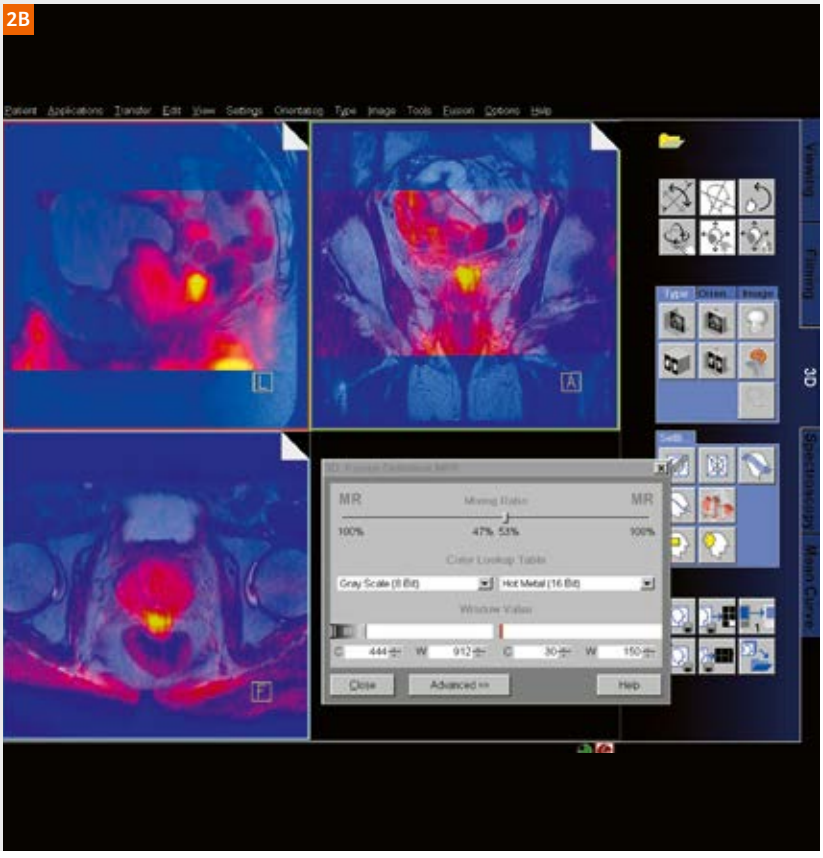

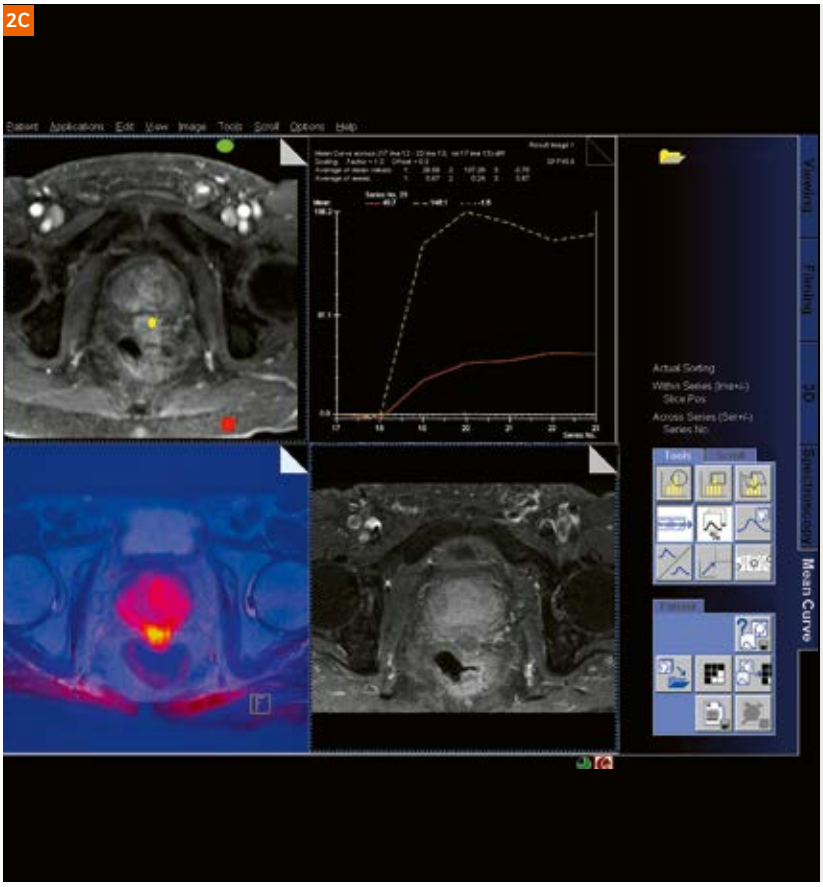

Figure 2C: This is an example of how the **MeanCurve TaskCard** can be used to analyze dynamic contrast enhanced images (DCE-MRI). High spatial resolution DCE-MRI data were acquired every 30 seconds (twice before and 5 times post 0.1 mmol/kg Gd-DTPA).
Top-left: Regions of interest (ROIs) are placed on the edge of the recurrence (yellow), in fat (red) and in air (green) on the 60 seconds post contrast image.
Top-right: Graphic depiction of contrast-enhancement with time shows marked early enhancement of the tumor recurrence with some wash-out (yellow line).
Bottom-left: Axial fusion image (b 1200 trace + T2-weighted) with 50% opacity.
Bottom-right: Late post contrast enhanced T1-weighted image with fat-suppression. The tumor recurrence is difficult to see.

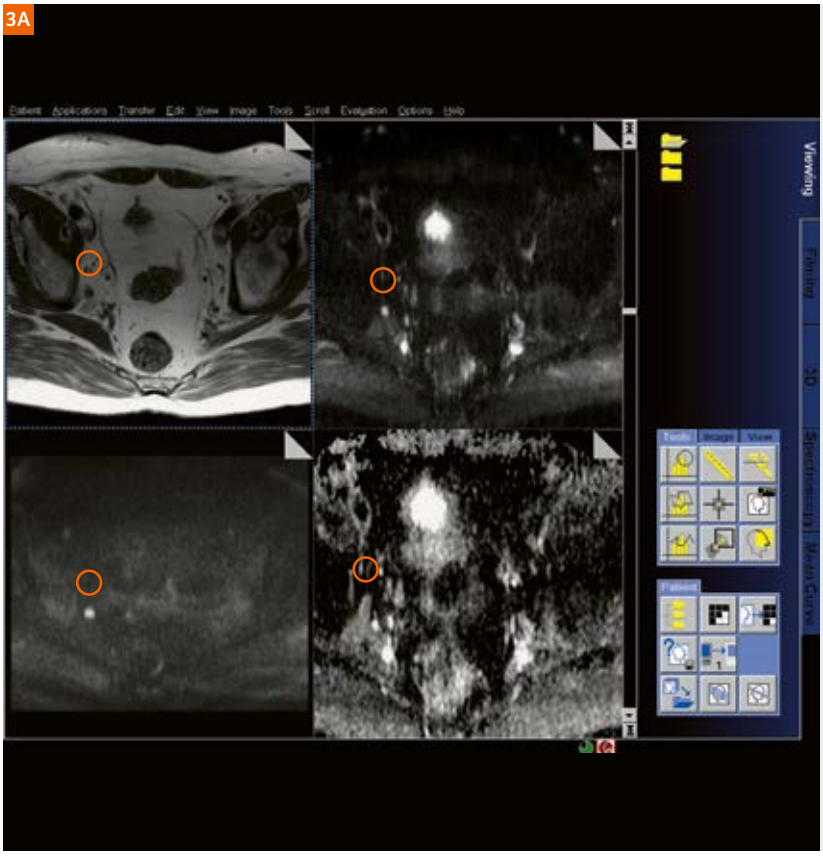

Figure 3: Nodal evaluation with diffusion-weighted MRI
72-year-old male patient with new diagnosis of prostate cancer. This is the same patient as in figure 5.

Figure 3A:
Top-left: There is an equivocally enlarged lymph node (7 mm) in the right internal iliac region (circled).
Top-right: on b0 images, the lymph node is difficult to see because of adjacent hyper-intensity in vascular structures. Note the hyperintense signal in the bladder anteriorly.
Bottom-left: b 1400 trace image shows persistent hyperintensity of the lymph node; all other pelvic structures are no longer hyper-intense.
Bottom-right: ADC maps show moderate restriction of water diffusion in the node (1170×10^{-5} mm^2/s). Taken together these findings are suggestive of metastatic invasion.

Figure 3B:
Top-left and **bottom-right**:
T2-weighted images confirm the anatomical location of the lymph node in the right internal iliac region.
Top-right and **bottom-left:** Fusion images (b 1400 trace + T2-weighted) with 50% and 100% opacities, confirms that the restricted diffusion is co-located in the lymph node.

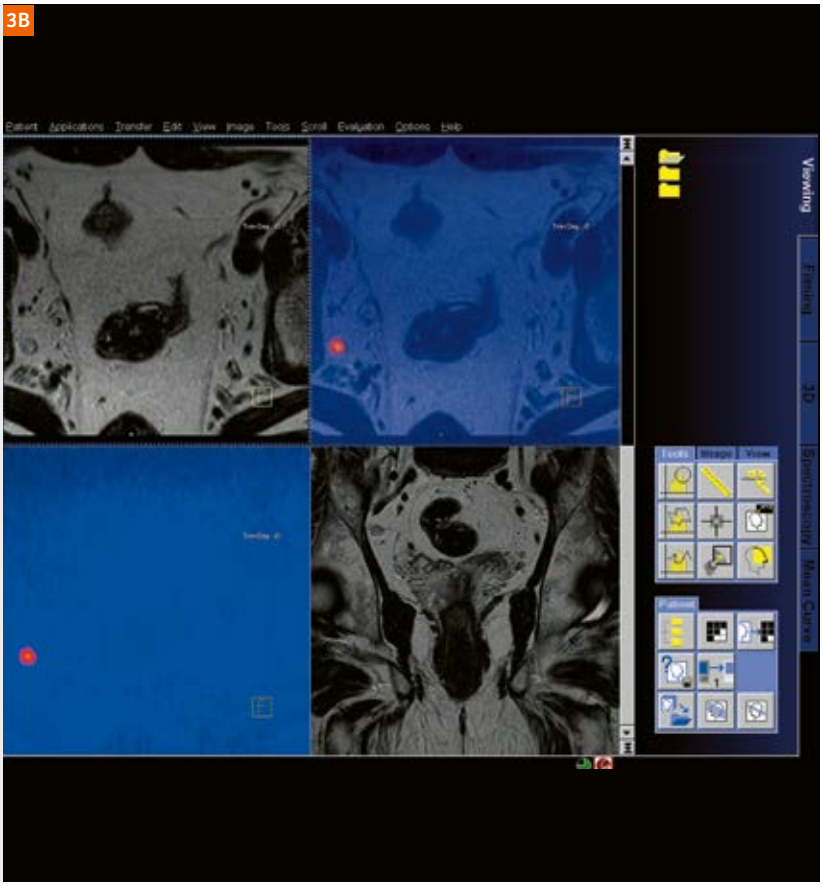

Figure 4: Bone marrow evaluation with diffusion-weighted MRI
75-year-old male patient with prostate cancer previously treated with radiotherapy for prostate cancer but now with rising PSA levels (2.4 ng/ml). The bone scan was negative and no enlarged lymph nodes were seen. The treated prostate gland had normal appearances post radiotherapy. There are 2 equivocal lesions seen in the bone marrow of the right hemipelvis (arrows) with a possible 3rd lesion on the left side shown on the STIR and T1-weighted sequences (**top-left** and **top-right**).
Bottom-left and **bottom-right:** Fusion images (b 1200 trace + T1-weighted) with 50% and 100% opacities (inverted grey-scale), confirms that the restricted diffusion is co-located in the 2 right sided abnormalities (ADC map not shown). These appearances are highly suggestive of cellular tissues within the bone marrow and therefore of metastases as being the cause of rising PSA levels.

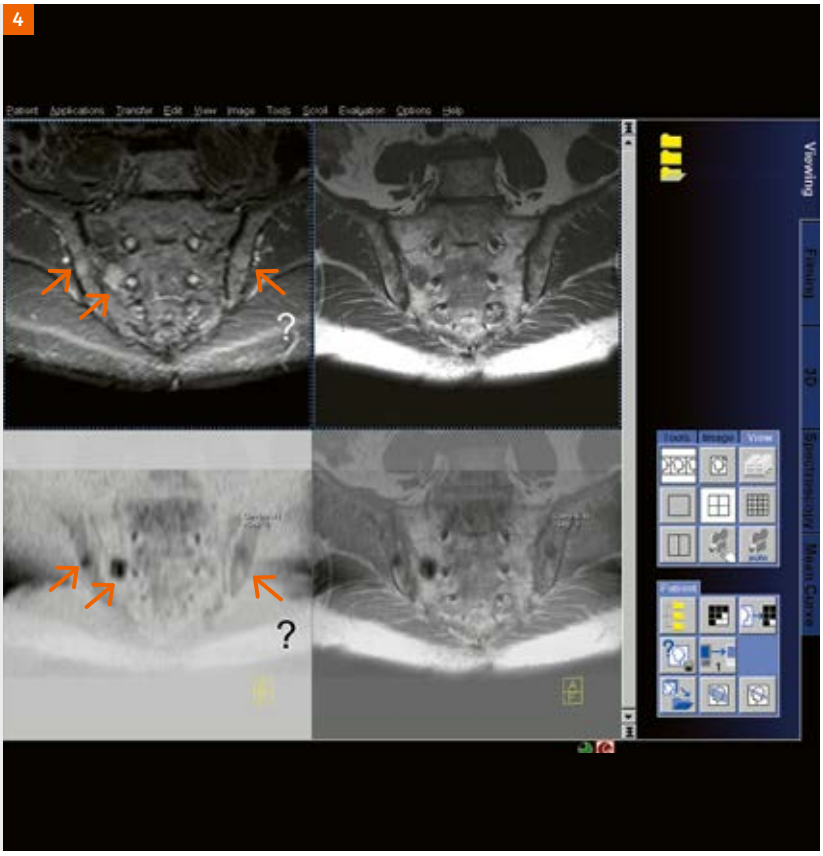

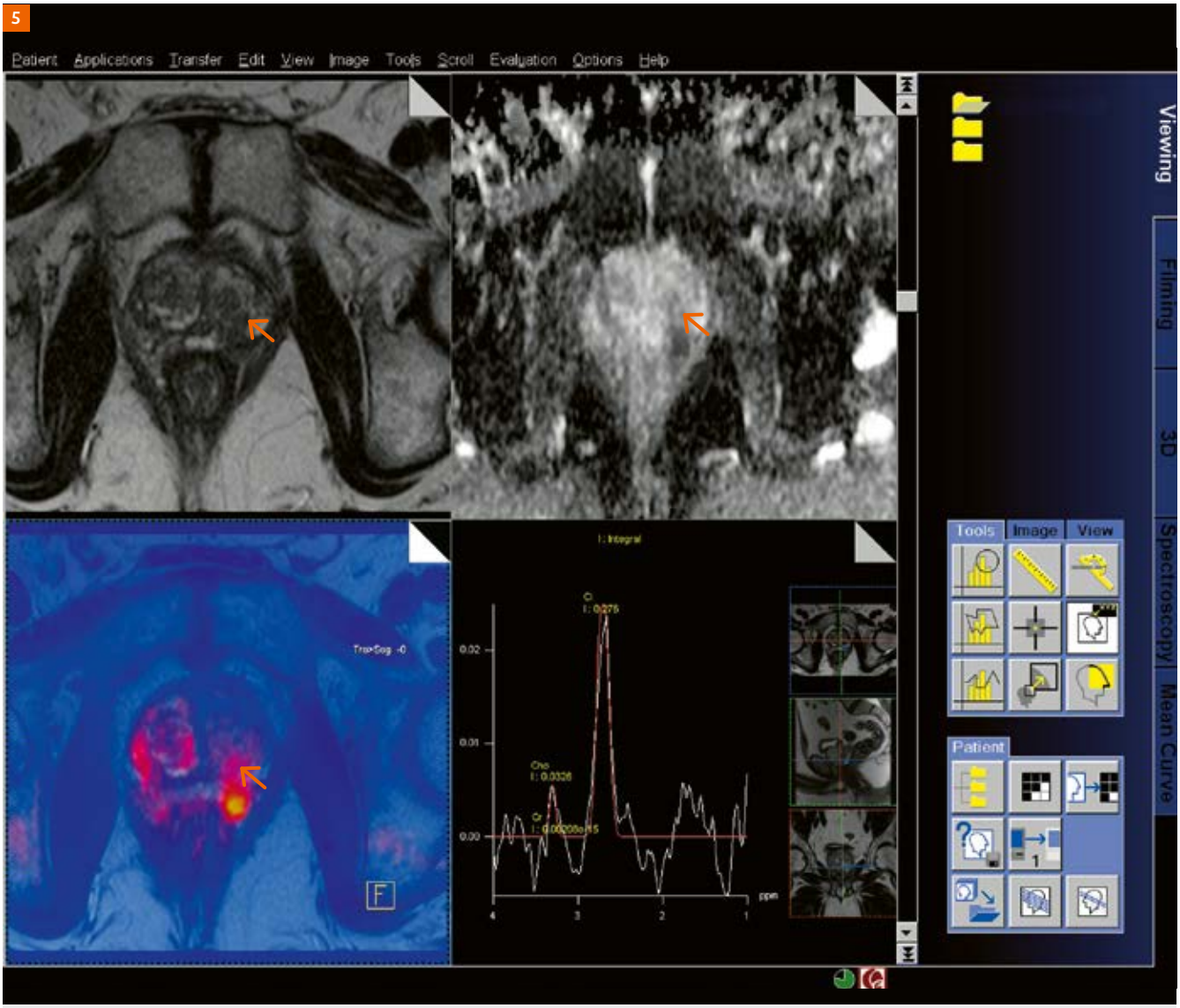

Figure 5: Discordance between DW-MRI and MRSI
This is the same patient as figure 3. 72-year-old male with new diagnosis of prostate cancer.
Top-left: The T2-weighted image shows moderate volume extra-capsular disease (T3A) with obliteration of the recto-prostatic angle (arrow).
Top-right: ADC map shows marked restriction of water diffusion in the region of the tumor.
Bottom-left: Fusion image (b 1000 trace + T2-weighted) confirms extraprostatic disease.
Bottom-right: MRSI (5 x 5mm voxel) shows normal spectrum with high citrate and low choline peaks in tumor.

Conclusions

As we move into the early 21st century it is clear that the prostate cancer imaging landscape will change radically. One challenge that radiologists will face is how to communicate complex multifunctional information to clinicians looking after patients. One method is to use **fusion tools** which allows anatomical and functional imaging to be co-localised using advanced, non-rigid software algorithms which can also be extremely useful for the purpose of data presentation, analysis, biopsy and therapy planning (examples are shown in figures). Standardized MRI reporting systems depicting graphically the location of abnormalities with the relative confidence of diagnostic radiologists will be needed to accurately convey complex information to clinicians. When using such toolbox multifunctional imaging approaches for prostate cancer it is often found that the results obtained are not always concordant (for example, morphology, DW-MRI, DCE-MRI may suggest the presence of tumor and MRSI does not – see figure 5 for an example case). The latter is not really surprising as these techniques are depicting different biological processes. The relative weighting to be placed on each component of a comprehensive examination in a given clinical situation will require

Technique (Siemens Tools)	Basis of usage	Indications	Authors' opinions on indication[1]
Morphology (Viewing TaskCard)	Depiction of the tumor extent	At almost every stage of the patient journey (not routinely used for very early stage cancers nor for very advanced disease)	+++
MRI biopsy (None specific)	To obtain histological material targeting a lesion/area Rarely to direct focal treatments to a specified region	Not routinely indicated. Used when cancer is suspected, TRUS biopsies are negative and) MRI depicts suspicious lesion(s)	+
Lymphography with lymph node specific contrast agent (Sinerem/Combidex*) (Lymph Node TaskCard) *Contrast agent not yet approved (Dec 07) but expected soon	To improve the accuracy of nodal staging	Remains to be decided but will include one or more of the following: • For newly diagnosed patients who are potentially curable (regardless of therapy modality) taking into account age and volume of disease (including small volume T3 disease) - >15% risk for nodal metastases - Gleason ≥7 (≥ 4+3) - PSA >10 ng/ml regardless of histological grade • For nodal mapping prior to IMRT or for targeted, extended PLND • PSA relapse – provided local relapse is excluded and bone scan is negative **and** in whom salvage pelvic radiotherapy therapy is being considered	+++
Proton MRSI (Spectroscopy TaskCard)	For depicting the intraprostatic tumor extent For assessing lesion aggressiveness (complementary information to DW-MRI and DCE-MRI and should be used together where possible)	• For depicting and confirming the location of the primary prostate cancer • PSA relapse when bone scan is negative and in whom salvage therapy is being considered	++ ++
DW-MRI (ADC tool)	For depicting the intraprostatic tumor extent (complementary information to DW-MRI and DCE-MRI and should be used together where possible)	• For depicting and confirming the location of the primary prostate cancer • PSA relapse when bone scan is negative and in whom salvage therapy is being considered	++ +++
DCE-MRI with mean curve analysis (DCE and mean curve TaskCards)	For depicting the intraprostatic tumor extent (complementary information to DW-MRI and DCE-MRI and should be used together where possible)	• For depicting and confirming the location of the primary prostate cancer • For monitoring response to hormonal therapy • For the assessment of the effectiveness of focal therapies (eg PDT, HIFU) • PSA relapse when bone scan is negative and in whom salvage therapy is being considered	++ + +++ +++
Data fusion (MPR TaskCard with fusion option)	Combining & displaying morphological with functional imaging	To aid in the co-localisation for data presentation purposes and for therapy planning. Very useful when used with proton-MRS and DWI.	+++
BOLD-MRI (No specific task card)	To map prostate cancer hypoxia. Used in combination with techniques that map the location of tumors	Could be used for focal ablative therapies as well as radiotherapy planning for boosting dose delivery to hypoxic regions.	+

Table 3: MRI techniques and their usage in prostate cancer patients

[1] These authors' opinions are based on literature reviews, personal experiences and recommendations are partly dependent on subjective assessments of ease of imaging data acquisition, analysis and interpretations

0 = No requirement; + = possible requirement; ++ = probably indicated; +++ = definite indication

sophisticated bioinformatics approaches where imaging data will be analysed with co-located immunohistochemistry, gene expression profiles and other biomarker data. We anticipate that fusion of functional imaging and other biomarker data will yield more robust and more effective tumor signatures. Thus, multi-spectral analysis of imaging data represents the new bioinformatics challenge of the early 21st century in prostate cancer.

References and suggested reading

1 Alonzi R, Padhani AR, Allen C. Dynamic contrast enhanced MRI in prostate cancer. Eur J Radiol. 2007 Sep;63(3):335-50.
2 Koh DM, Collins DJ. Diffusion-weighted MRI in the body: applications and challenges in oncology. AJR Am J Roentgenol. 2007 Jun;188(6):1622-35.
3 Zapotoczna A, Sasso G, Simpson J, Roach M 3rd. Current role and future perspectives of magnetic resonance spectroscopy in radiation oncology for prostate cancer. Neoplasia. 2007 Jun;9(6):455-63.
4 Claus FG, Hricak H, Hattery RR. Pretreatment evaluation of prostate cancer: role of MR imaging and 1H MR spectroscopy. Radiographics. 2004 Oct; 24 Suppl 1:S167-80.
5 Hoskin PJ, Carnell DM, Taylor NJ, Smith RE, Stirling JJ, Daley FM, Saunders MI, Bentzen SM, Collins DJ, d'Arcy JA, Padhani AP. Hypoxia in prostate cancer: correlation of BOLD-MRI with pimonidazole immunohistochemistry-initial observations. Int J Radiat Oncol Biol Phys. 2007 Jul 15;68(4):1065-71.
6 Padhani AR, Krohn KA, Lewis JS, Alber M. Imaging oxygenation of human tumours. Eur Radiol. 2007 Apr;17(4):861-72.
7 Harisinghani MG, Barentsz J, Hahn PF, Deserno WM, Tabatabaei S, van de Kaa CH, de la Rosette J, Weissleder R. Non-invasive detection of clinically occult lymph-node metastases in prostate cancer. N Engl J Med. 2003 Jun 19;348(25):2491-9.
8 Saksena MA, Saokar A, Harisinghani MG. Lymphotropic nanoparticle enhanced MR imaging (LNMRI) technique for lymph node imaging. Eur J Radiol. 2006 Jun;58(3):367-74

Contact

Professor Anwar R. Padhani
MB, BS, FRCP, FRCR
Paul Strickland Scanner Centre
Mount Vernon Hospital

Rickmansworth Road
Northwood, Middlesex HA6 2RN
United Kingdom
anwar.padhani@
stricklandscanner.org.uk

Watch Cancer Develop Multidrug Resistance

In this video Professor Padhani shows how quantitative whole-body MRI is used to monitor therapy response in metastatic breast cancer. Watch the video at

www.siemens.com/wb-mri

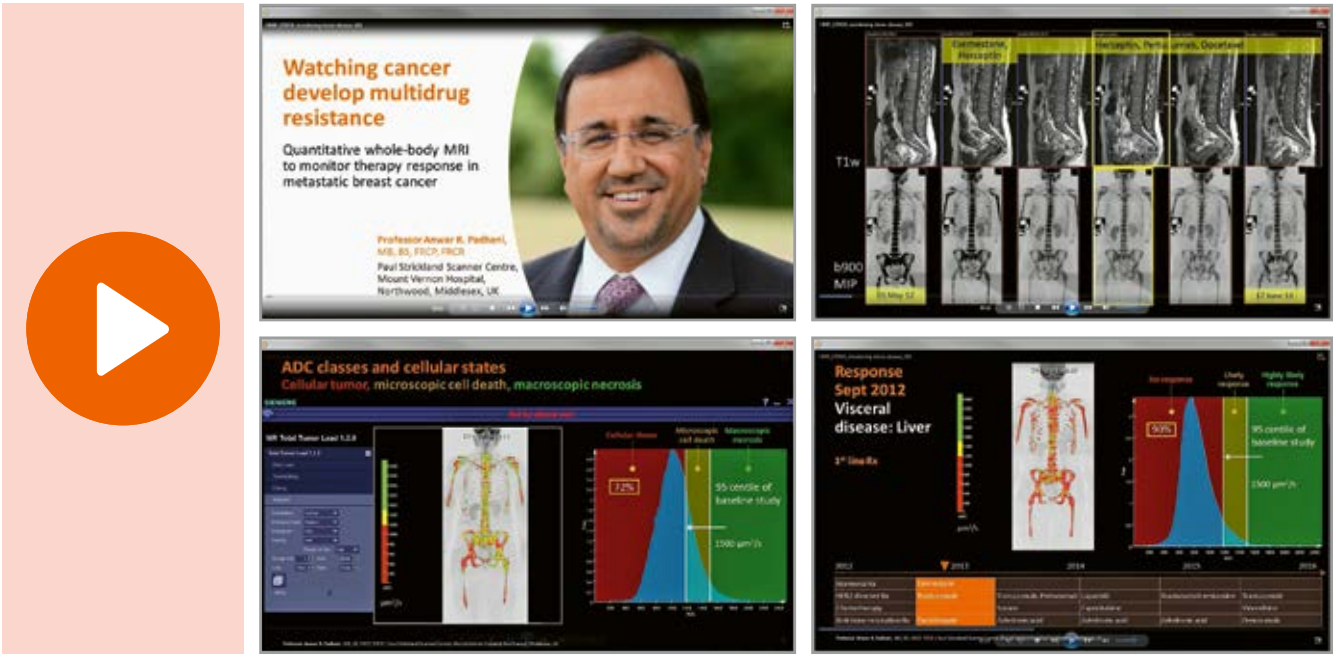

High-Resolution Diffusion-Weighted Imagings of the Prostate Using RESOLVE at 3T

Liang Li[1]; Liang Wang[1]; Hui Liu[2]

[1] Department of Radiology, Tongji Hospital, Tongji Medical College, Huazhong University of Science and Technology, Wuhan, China
[2] MR Collaboration NE Asia, Siemens Healthcare, Shanghai, China

Introduction

Diffusion-weighted imaging (DWI) is becoming an increasingly robust tool in the assessment and exclusion of prostate disease [1]. However, multiple recent studies have raised concerns regarding the anatomical distortion of single-shot DWI. A novel approach to distortion reduction using RESOLVE, resulting in a high-resolution DWI examination, is described [2–5]. In our hospital, we performed hundreds of prostate examinations of patients using RESOLVE. The technique achieves a low level of susceptibility artifact by allowing a very short echo spacing in the EPI echo train and the artifacts are further reduced by combining the technique with parallel imaging using GRAPPA [6].

Protocol

Prostate DWI examinations were performed on a clinical 3T scanner (MAGNETOM Skyra, Siemens Healthcare, Erlangen, Germany) with an 18-channel body-matrix coil placed over, and a spine coil underneath, the pelvis. The patients were positioned in a head-first supine position.

At 3T MRI, RESOLVE images were acquired with the following parameters: parallel imaging using GRAPPA with an acceleration factor of 2, FOV 260 mm, matrix 128 x 176, pixel size 1.2 mm x 1.2 mm, 20 slices, slice thickness 3 mm, number of readout segments 13, TR 4800 ms, TE 60 ms, b-values of 0 s/mm^2 (1 average) and 800 s/mm^2 (2 averages), total scanning time 6 min 11 s.

Case 1

57-year-old man presented to his primary care provider in January 2014 with a 2-month history of increasing urinary frequency and poor stream. He denied any gross hematuria, bone pain, or significant weight loss. Digital rectal examination (DRE) revealed an asymmetrically enlarged, firm, and nontender prostate. Serum prostate-specific antigen (PSA) was 12.8 ng/ml. Tamsulosin hydrochloride (Flomax®, Boehringer, Ingelheim, Germany) 0.4 mg daily was started and the patient was referred for initial urologic evaluation. The patient denied any occupational exposures or family history of prostate cancer or other genitourinary malignancy. On the first day, prostate ss-EPI DWI imaging revealed a lesion in anterior fibromuscular stroma (AFS) region of his prostate. On the second day, we found two lesions in DWI using RESOLVE technology. Transrectal ultrasound (TRUS)-guided prostate biopsy and pathological examinations were performed subsequently. The two lesions were confirmed as prostate adenocarcinoma (left: Gleason 4+4, right: Gleason 3+4).

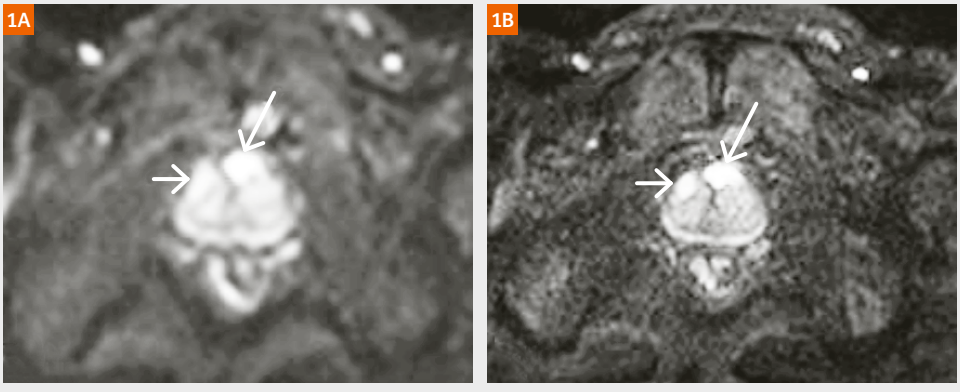

Figure 1A: Conventional ss-EPI DWI revealing only a lesion in the anterior fibromuscular stroma (AFS) region (long white arrow).

Figure 1B RESOLVE EPI DWI showing excellent high-resolution image quality and revealing another lesion (short white arrow) without anatomical distortion.

In addition, our past clinical standard single-shot DWI images were also acquired for comparison using the following parameters: Parallel imaging using GRAPPA with an acceleration factor of 2, FOV 260 mm, matrix 64 x 88, phase partial Fourier factor 6/8, pixel size 2.4 mm x 2.4 mm, 20 slices, slice thickness 3 mm, TR 4500 ms, TE 85 ms, b-values of 0 s/mm^2 (1 average) and 800 s/mm^2 (2 averages), total scanning time 1 min 20 s.

Case 2

A 69-year-old man presented with a chief complaint of refractory urinary retention. DRE was performed with prostate gland of 4 finger breadths, firm consistency and smooth surface. The PSA level was 5.16 ng/ml. A Doppler ultrasound examination demonstrated an enlargement of the prostate volume (48 x 52 x 60 mm^3), asymmetric shape, with multiple hypointense nodules. The biopsy sample confirmed benign prostatic hyperplasia (BPH) and chronic prostatitis.

Figure 2A: Conventional ss-EPI DWI displaying a low-resolution prostate image.

Figure 2B: RESOLVE EPI DWI showing clearly excellent high-resolution image with multiple hyperplastic nodules.

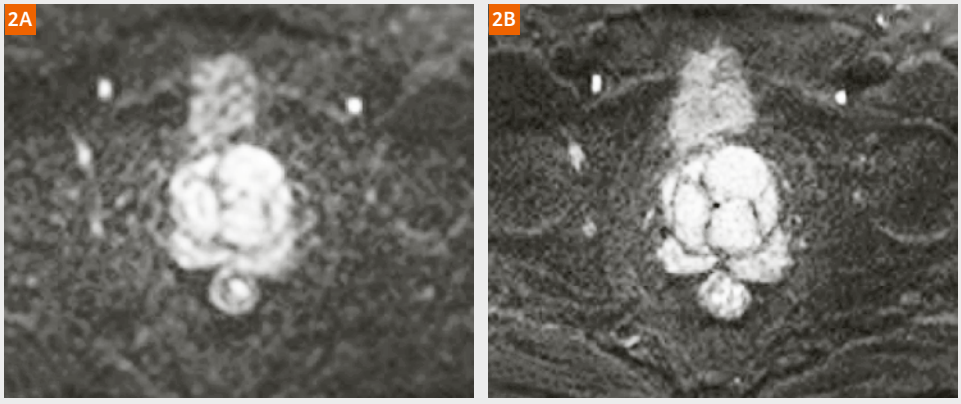

Case 3

A 70-year-old man suffered from acute urinary retention requiring urethral catheterization, with no evidence of hematuria or fever. He had a history of chronic urinary retention, which was treated with oral medicine (Flomax®) for 2 months, but no history of urinary trauma or infection. Laboratory testing such as blood count, serum biochemistry, and urinalysis were in the normal range. A urine culture was negative, and the serum level of PSA was 3.1 ng/ml. The single-shot DWI revealed a nodular lesion with focal high signal-intensity in the right peripheral zone of his prostate, while RESOLVE DWI examination found no abnormal lesions. TRUS-guided prostate biopsy confirmed benign prostatic hyperplasia (BPH).

Figure 3A: Conventional ss-EPI DWI revealing a suspicious lesion in the right peripheral zone (long white arrow).

Figure 3B: RESOLVE EPI DWI showing no abnormal lesions. The suspicious lesion being misdiagnosed as prostate cancer due to susceptibility effect.

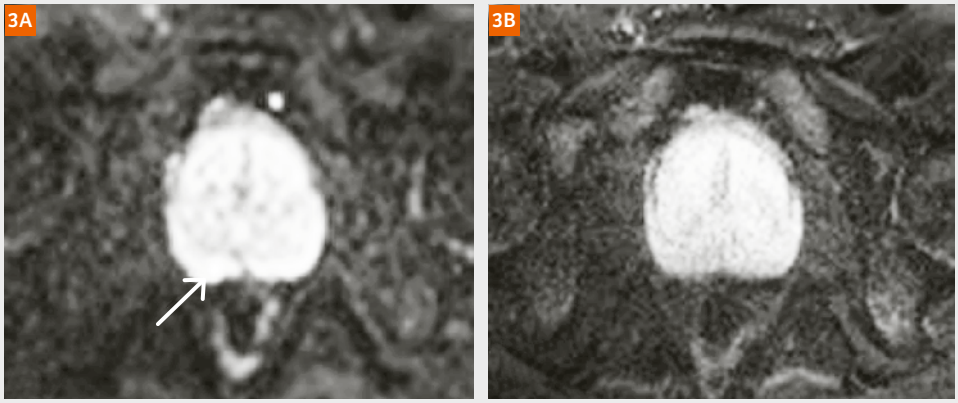

Conclusion

Results from hundreds of examinations of our prostate patients indicate that anatomic depiction and overall image quality were improved with the RESOLVE sequence when compared with the single-shot DWI sequence. Prostate DWI applications with RESOLVE demonstrated reduced artifacts and improved lesion detection.

In our previous unpublished study, we had obtained a number of diagnostic-quality prostate DWIs based on RESOLVE. For image sharpness, anatomical distortion, imaging contrast, lesion conspicuity, detailed anatomical visualization and diagnostic confidence, RESOLVE EPI was considered the to be overall superior in 90% of the cases. In the past, to assist workflow, we needed to have rectum preparation in a certain number of patients where the susceptibility artifacts coming from the rectum was strong. However, we have now eliminated the need for this preparation when using RESOLVE, because of less susceptibility impact on the prostate imaging.

In summary, the new high-resolution RESOLVE protocol provides significant benefits compared with the mostly clinically used single-shot DWI. The higher spatial resolution results in better lesion conspicuity, better defined internal architecture, and better overall image quality. In the future, this method may have potential as a tool to predicate prostate cancer at an earlier stage or to obtain an image-guided prostate biopsy.

References

1 Jin G, Su DK, Luo NB, et al. Meta-analysis of diffusion-weighted magnetic resonance imaging in detecting prostate cancer. J Comput Assist Tomogr. 2013;37(2): 195-202.
2 Holdsworth SJ, Skare S, Newbould RD, Bammer R. Robust GRAPPA-accelerated diffusion-weighted readout-segmented (RS)-EPI. Magn Reson Med. 2009; 62(6): 1629-40.
3 Frost R, Porter DA, Miller KL, Jezzard P. Implementation and assessment of diffusion-weighted partial Fourier readout-segmented echo-planar imaging. Magn Reson Med. 2012;68(2):441-51.
4 Yeom KW, Holdsworth SJ, Van AT, et al. Comparison of readout-segmented echo-planar imaging (EPI) and single-shot EPI in clinical application of diffusion-weighted imaging of the pediatric brain. AJR Am J Roentgenol. 2013;200(5):W437-43.
5 Bogner W, Pinker-Domenig K, Bickel H, et al. Readout-segmented echo-planar imaging improves the diagnostic performance of diffusion-weighted MR breast examinations at 3.0 T. Radiology. 2012;263(1):64-76.
6 Griswold MA, Jakob PM, Heidemann RM, et al. Generalized autocalibrating partially parallel acquisitions (GRAPPA). Magn Reson Med. 2002;47(6):1202-10.
7 Porter DA, Heidemann RM. High resolution diffusion-weighted imaging using readout-segmented echo-planar imaging, parallel imaging and a two-dimensional navigator-based reacquisition. Magn Reson Med. 2009;62(2):468-75.
8 Holdsworth SJ, Skare S, Newbould RD, et al. Readout-segmented EPI for rapid high resolution diffusion imaging at 3 T. Eur J Radiol. 2008;65(1):36-46.

Contact

Professor Liang Wang, M.D., Ph.D.
Vice-Chairman, Department of Radiology
Tongji Hospital, Tongji Medical College
Huazhong University of Science & Technology

Wuhan 430030
China
Phone: +86 (27) 83663737
wangliang2001@gmail.com

Wang Liang

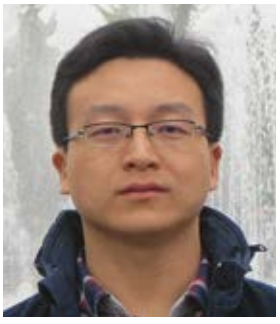

Li Liang

PI-RADS 2
Standardized Prostate MRI Reporting

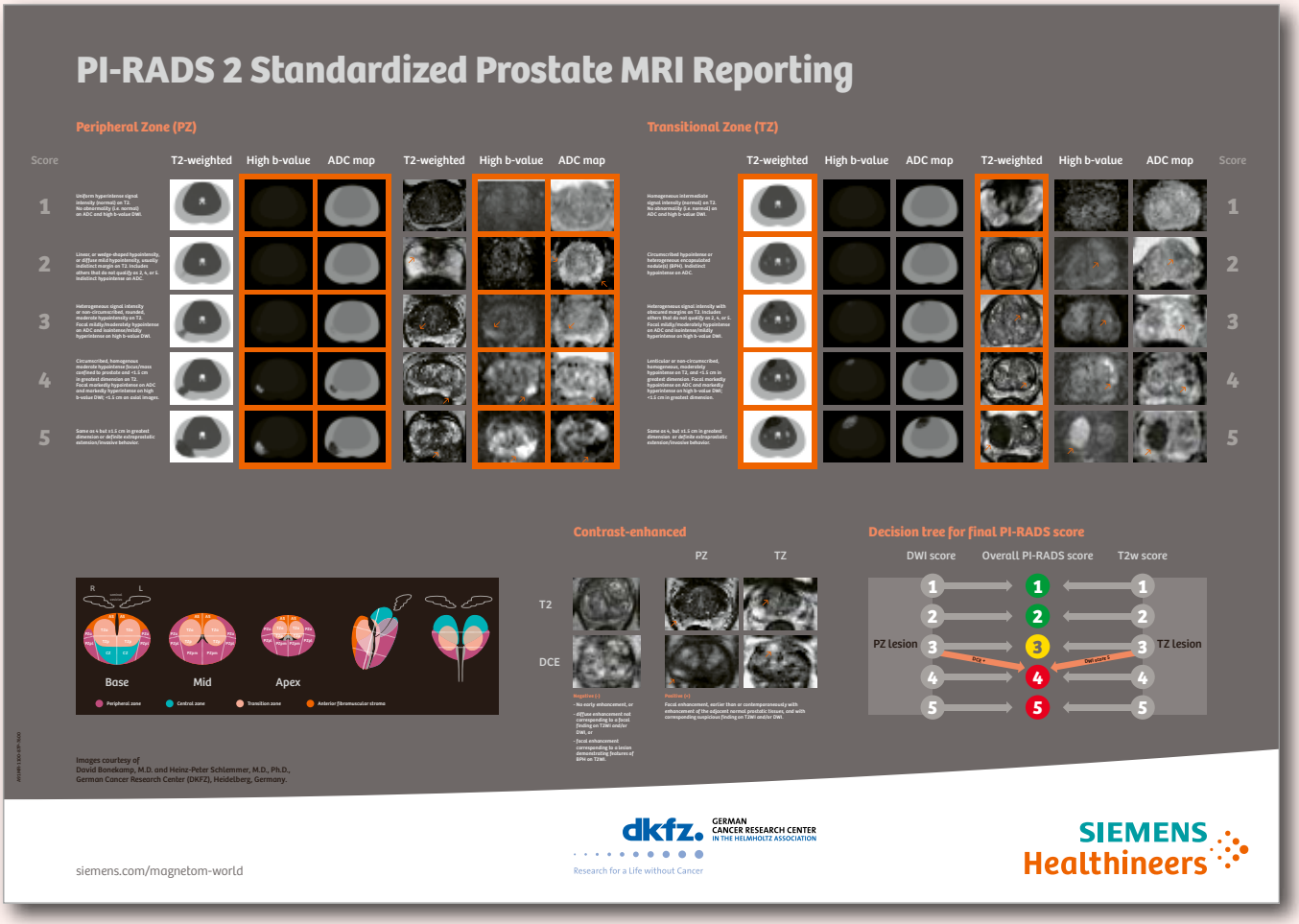

Visit us at **www.siemens.com/magnetom-world**

Go to > **Publications** > **Subscriptions** > **MRI Poster**

Get your free copy of the PI-RADS poster

Functional Prostate MR Including Dynamic Contrast-Enhanced T1-Weighted Imaging at 1.5 Tesla Without Endorectal Coil. First Clinical Experiences with a Study Protocol at Multi-Imagem, Brazil

Leonardo Kayat Bittencourt, M.D.; Thomas Doring, MSc; Marcio Bernardes, RT; Emerson Gasparetto, M.D., Ph.D.; Romeu Cortês Domingues, M.D.

CDPI Clínica de Diagnóstico Por Imagem, Multi-Imagem, UFRJ – Federal University of Rio de Janeiro, Rio de Janeiro, Brazil

Introduction

Reviewing the current literature on prostate MR, most authors rely on the use of 3T scanners that reveal better diagnostic and staging accuracy than the previous studies using older 1.5T and 1T machines in the 90's. However, in most countries 1.5T MR scanners are still more widely available than 3T machines. Looking at new developments in coil technology this new generation of 1.5 Tesla superconducting MR scanners potentially provides an acceptable performance on the management of prostate cancer (PCa) patients.

Moreover, the continuing improvement of functional sequences, namely diffusion-weighted imaging (DWI) and dynamic contrast enhancement (DCE) T1w imaging and the development of new post-processing tools (i.e., image-fusion and pharmacokinetic maps) could further contribute on the diagnostic and staging accuracy of MRI including 1.5T MR scanners. Based on the literature, multi-modal imaging of the prostate at 1.5 Tesla includes the usage of an endorectal coil. However, in clinical routine the application of such a coil can be restricted by various reasons such as proctitis. However, it should also be taken into account that the procedure of placing an endorectal coil can result in low acceptance of the exam and potentially reduces patient compliance significantly. Therefore it is of high clinical interest to better understand the potential but also the limitations of prostate MRI at 1.5 Tesla without application of an endorectal coil.

In this article, we describe in detail our prostate MR protocol and post-processing parameters at 1.5 Tesla without endorectal coil with special focus on DCE T1w imaging, and briefly present the preliminary results, with illustrative cases.

Materials and methods

This protocol was developed in 2009, as part of an ongoing long-term prostate MR research project. The study was approved by the local Ethics and Research Committee, and all patients signed an informed consent.

Thirteen consecutive patients were submitted to prostate MR examinations, prior to prostatectomy. Patients' age ranged between 51 and 77 years (average 63 years), their PSA levels varying between 3.4 and 42.0 ng/mL (median 8.6 ng/mL). Examinations (table 1) were done on an 18-channel 1.5T scanner (MAGNETOM Avanto, Siemens Healthcare, Erlangen, Germany), with a combination of the 6-channel phased-array surface coil (Body Matrix) combined with up to 6 elements of the integrated spine coil. Prior to the examinations, the patients were given 10 mg of n-methil-scopolamine bromide (Buscopan®, Boehringer Ingelheim, Brazil), in order to attenuate peristalsis. The study protocol consisted of high-resolution T2-weighted turbo spin echo (TSE) sequences in the axial (TR 4750 ms, TE 101 ms, no PAT, FOV (160 x 160) mm^2, matrix (256 x 230) px^2, slice thickness 3 mm, no gap, 3 averages, acquisition time 5:47 min),

Feature	Prostate MR	Histopathology
Unilateral Involvement	3	2
Bilateral Involvement	10	11
Extra-prostatic extension	3	4
Seminal Vesicle extension	1	1
Positive Lymph Nodes	0	0

Table 1: Examinations performed on a 1.5T MAGNETOM Avanto.

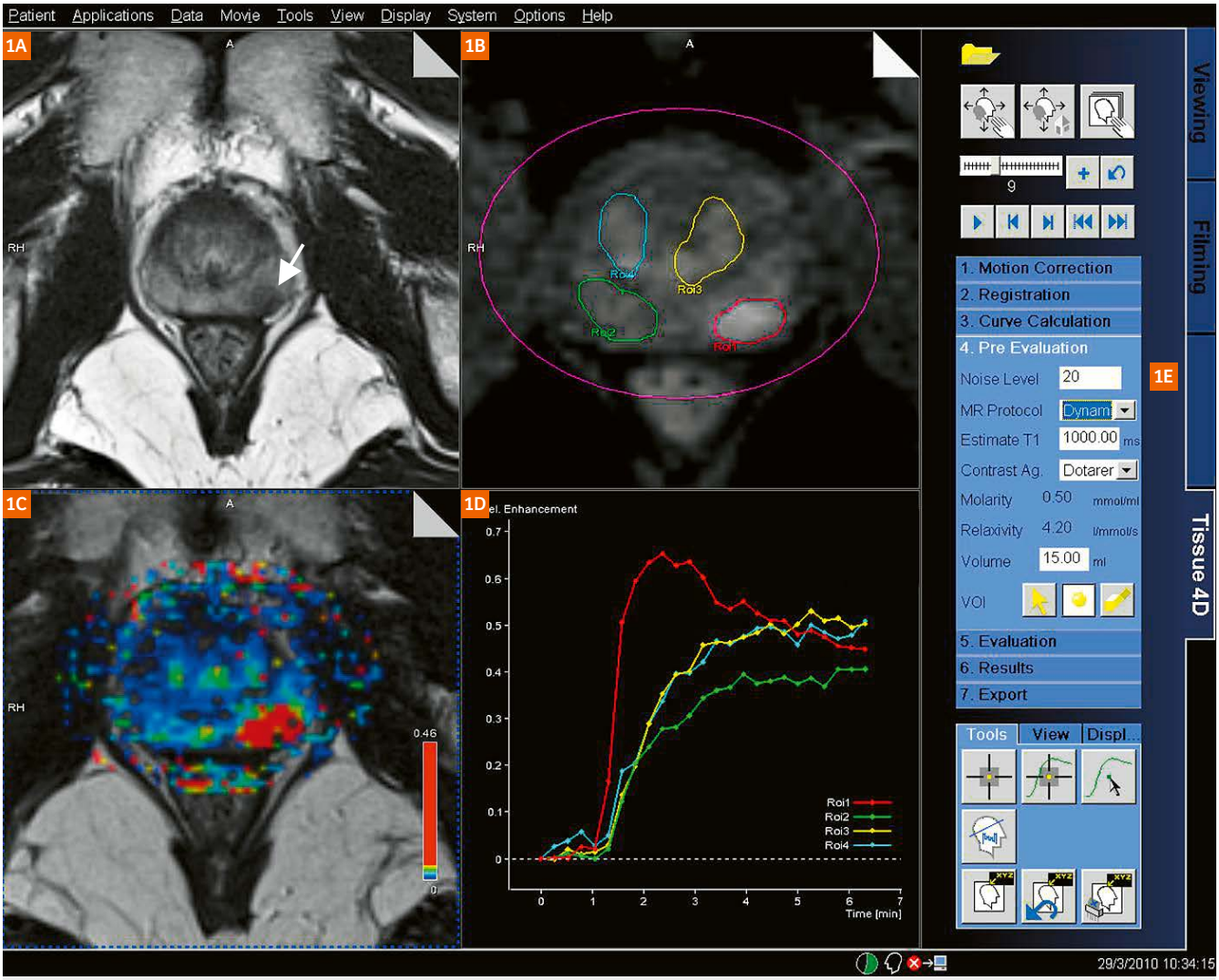

Figure 1: *syngo* Tissue 4D screen capture, depicting its four panels, with anatomical (T1w or T2w) images in **1A,** (subtracted) image of dynamic data set in **1B,** parametric maps (K_{trans}, Kep, Ve, iAUC) overlaid on anatomy in **1C,** and relative enhancement curves in **1D.** Note that the suspicious T2w hypointense area in **1A** (arrowhead) corresponds to the red ROI in **1B,** the focally increased K_{trans} area in **1C** and early/intense enhancing curve with washout in **1D.**

coronal (TR 3000 ms, TE 101 ms, no PAT, FOV (160 x 160) mm², matrix (256 x 230) px², slice thickness 3.5 mm, 20% gap, 2 averages, acquisition time 2:15 min) and sagittal (TR 3800 ms, TE 100 ms, no PAT, FOV (170 x 170) mm², matrix (320 x 240) px², slice thickness 3 mm, 10% gap, 2 averages, acquisition time 3:21 min) planes, high-resolution axial dark fluid T1-weighted sequence (TIRM; TR 2100 ms, TE 20 ms, TI 829.7 ms, PAT factor 2 (*syngo* GRAPPA), FOV (200 x 180) mm², matrix (256 x 200) px², slice thickness 3 mm, 10% gap, 2 averages, acquisition time 3:09 min), DWI (*syngo* REVEAL) in the axial plane (ep2d_diff; TR 3000 ms, TE 88 ms, b-values 0, 500, 1000 mm/s², 3-scan trace, ADC map Inline, noise level set to 0, PAT factor 2 (*syngo* GRAPPA), FOV (200 x 200) mm², matrix (150 x 150) px², slice thickness 3.5 mm, no gap, 8 averages, acquisition time 2:57 min), thick-slice T2-weighted sequence in the axial plane covering lymph node stages from the renal veins down to the pubic bone (HASTE; TR 700 ms, TE 38 ms, PAT factor 2 (*syngo* GRAPPA), FOV (350 x 317) mm², matrix (512 x 440) px² (interpolated), slice thickness 5 mm, 100% gap, 1 average, acquisition time 0:30 min), and DCE T1w images acquired with a 3D gradient echo (GRE) sequences (VIBE; TR 4.08 ms, TE 1.43 ms, PAT factor 2 (*syngo* GRAPPA), no fat saturation, FOV (280 x 280) mm², matrix (192 x 192) px², slice thickness 3 mm, 1 average, 40 measurements, 6.8 seconds per measurement, total

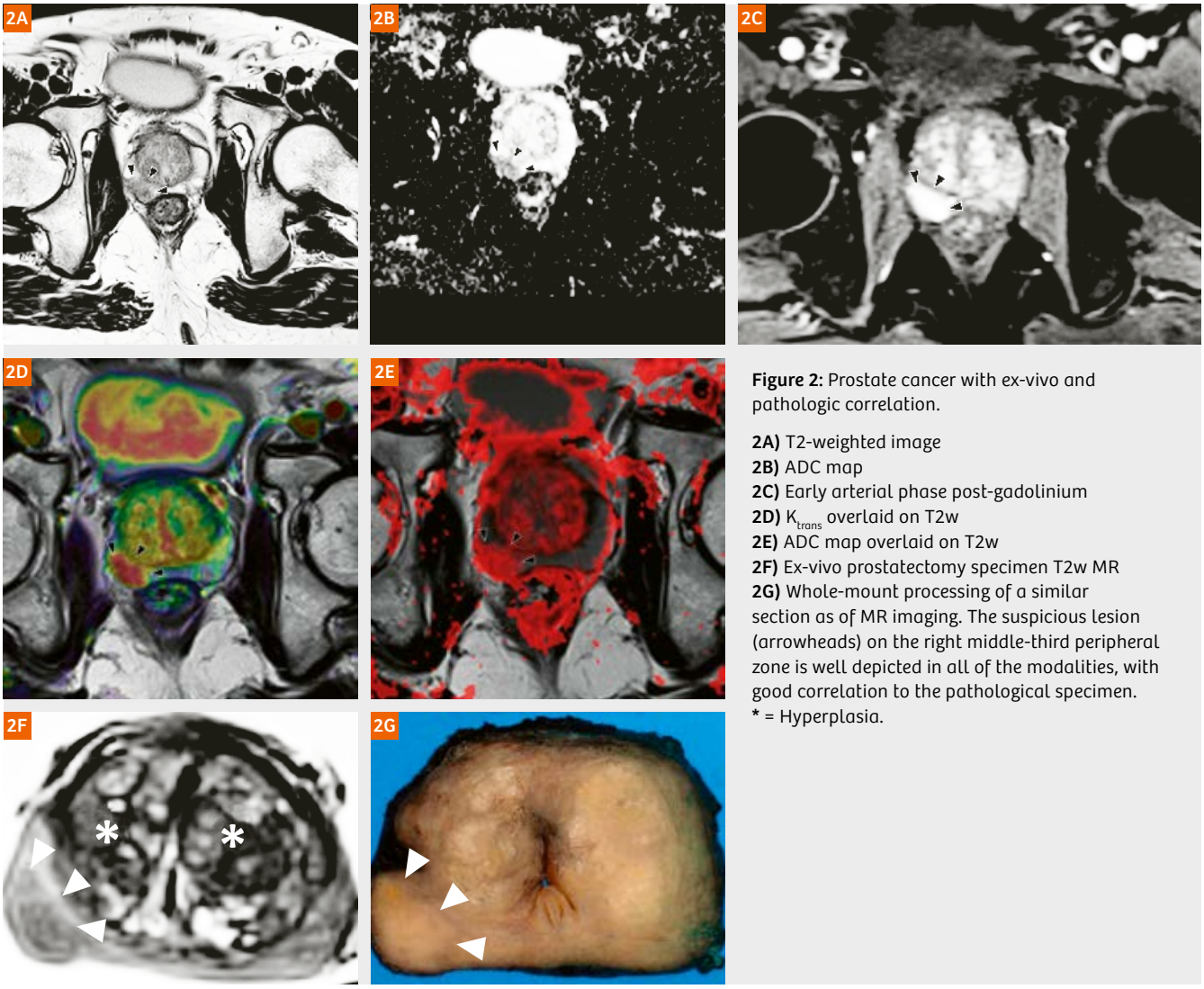

Figure 2: Prostate cancer with ex-vivo and pathologic correlation.

2A) T2-weighted image
2B) ADC map
2C) Early arterial phase post-gadolinium
2D) K_{trans} overlaid on T2w
2E) ADC map overlaid on T2w
2F) Ex-vivo prostatectomy specimen T2w MR
2G) Whole-mount processing of a similar section as of MR imaging. The suspicious lesion (arrowheads) on the right middle-third peripheral zone is well depicted in all of the modalities, with good correlation to the pathological specimen.
* = Hyperplasia.

acquisition time 4:33 min) (cubital intravenous application of 0.2 mmol/kg of gadolinium-chelate (DOTAREM, Guerbet, Aulnay-sous-Bois, France) on an MR-compatible power injector (Injektron 82 MRT, Medtron, Saarbrücken, Germany) between the second and third measurements). The whole examination took about 30 minutes. Recently, we also added multi-flip angle volumetric T1w sequences (VIBE, same parameters as above, 1 measurement each, respectively 2°, 5°, 8°, and 15° flip angle) prior to contrast injection, in order to estimate the T1 value, so as to enable accurate transfer constant (k_{trans}) calculation on DCE post-processing.

DCE images were post-proccessed using a work-in-progress package of the *syngo* Tissue 4D application. The *syngo* Tissue 4D applications allows pharmacokinetic modeling according to the Tofts-model including parameter calculations, namely transfer constant (k_{trans}), volume constant (Kep), extra-cellular volume of distribution (Ve) and integral area under the curve (iAUC). In addition, parametric color-maps can be generated and fused over MR morphology to allow accurate and fast assessment of the prostate parenchyma, and also to enable accurate measurements of pharmacokinetic parameters on suspected areas (Fig. 1). There is a built-in function to correct for movement between acquisition phases, which we use whenever required. The curve calculation is based on the placement of regions-of-interest (ROIs) (for evaluation of data, four ROIs were evaluated in our study: ROI 1: suspected lesion, ROI 2: contralateral peripheral zone, ROI 3: ipsillateral central gland, ROI 4: contralateral central gland). For calculation of parameters, the software requires input by the user; pre-evaluation parameters used in this study are as follow: noise level: 20, MR protocol: T1 and Dynamic, Contrast agent: Dotarem, volume: variable. The volume-of-interest (VOI) is defined by an elliptical area – drawn by the user – which encompasses the whole prostate volume. The parametric maps are generated from the full VOI, using the Tofts-model. For this, an arterial input function has to be selected; in most of our patients, a "slow"

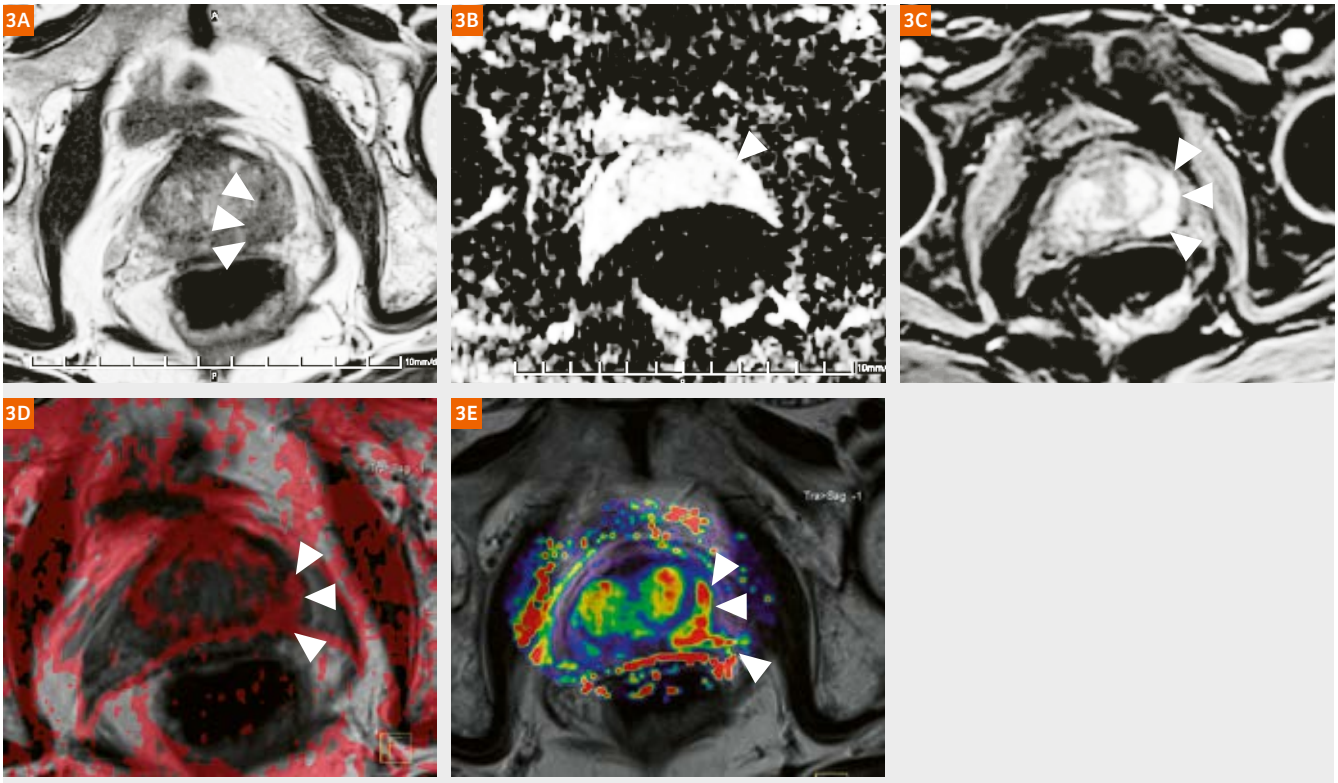

Figure 3: Extra-prostatic extension.

3A) T2w image showing a nodular T2 hypo-intense area on the left base (arrowheads), focally bulging the capsular contour.
3B) On the ADC map, there is restricted diffusion on the same spot, but further anatomical information.
3C) Early arterial phase post-gadolinium image, depicting intense and early enhancement on the suspicious area (arrowheads).
3D) ADC map overlaid on T2w image, confirming good correlation with both anatomical and functional findings.
3E) K_{trans} map overlaid on T2w image, showing that the focal permeability abnormalities (black arrowheads) extend outside the prostate contour (white arrowhead), strengthening the suspicion for extra-prostatic extension. This was the only sequence that depicted abnormal findings outside of the prostate parenchyma, showing the importance of multimodality imaging on the evaluation of prostate cancer.

arterial input function has been chosen. K_{trans} and iAUC maps are saved as DICOM series, for further post-processing.

Post-processed images are afterwards overlaid on transverse T2w images, using *syngo* 3D-FUSION® (Siemens Healthcare, Erlangen, Germany), using PET-Rainbow and Descending Red Ramp color look-up tables, respectively for the k_{trans} and the ADC map.

For evaluation of findings within the study setting, one reader (LKB, 5 years of experience, 2 years on prostate MR) evaluated all of the examinations and imaging findings were registered on a dedicated evaluation sheet. Focused on the evaluation of capsular penetration of prostate cancer for planning of radical prostatectomy, suspected lesions were characterized by laterality (left x right x bilateral), presence of local extra-prostatic extension and seminal vesicle involvement. Prostatectomy specimens were submitted to routine histopathological evaluation, except for one, submitted to whole-mount processing.

Results

Prostatectomy showed prostate adenocarcinoma in all 13 cases, with Gleason grades varying between 6 (3+3) and 9 (4+5) (median 6).

In all 13 cases the main tumor focus was correctly identified by MR imaging. The laterality of the lesion was correctly determined by MR in 12 patients (sensitivity: 90%, specificity: 100%), eleven of which had bilateral tumors. There was one false negative, in a patient with bilateral involvement substaged as unilateral tumor by MR.

Four patients had extra-prostatic tumoral extension, three of them being identified by MR imaging (sensitivity: 75%, specificity: 100%).

Only one patient had seminal vesicle tumoral invasion, also seen on MR imaging.

No patient had tumor-positive pelvic lymph nodes, neither was it suspected by MR in any of them.

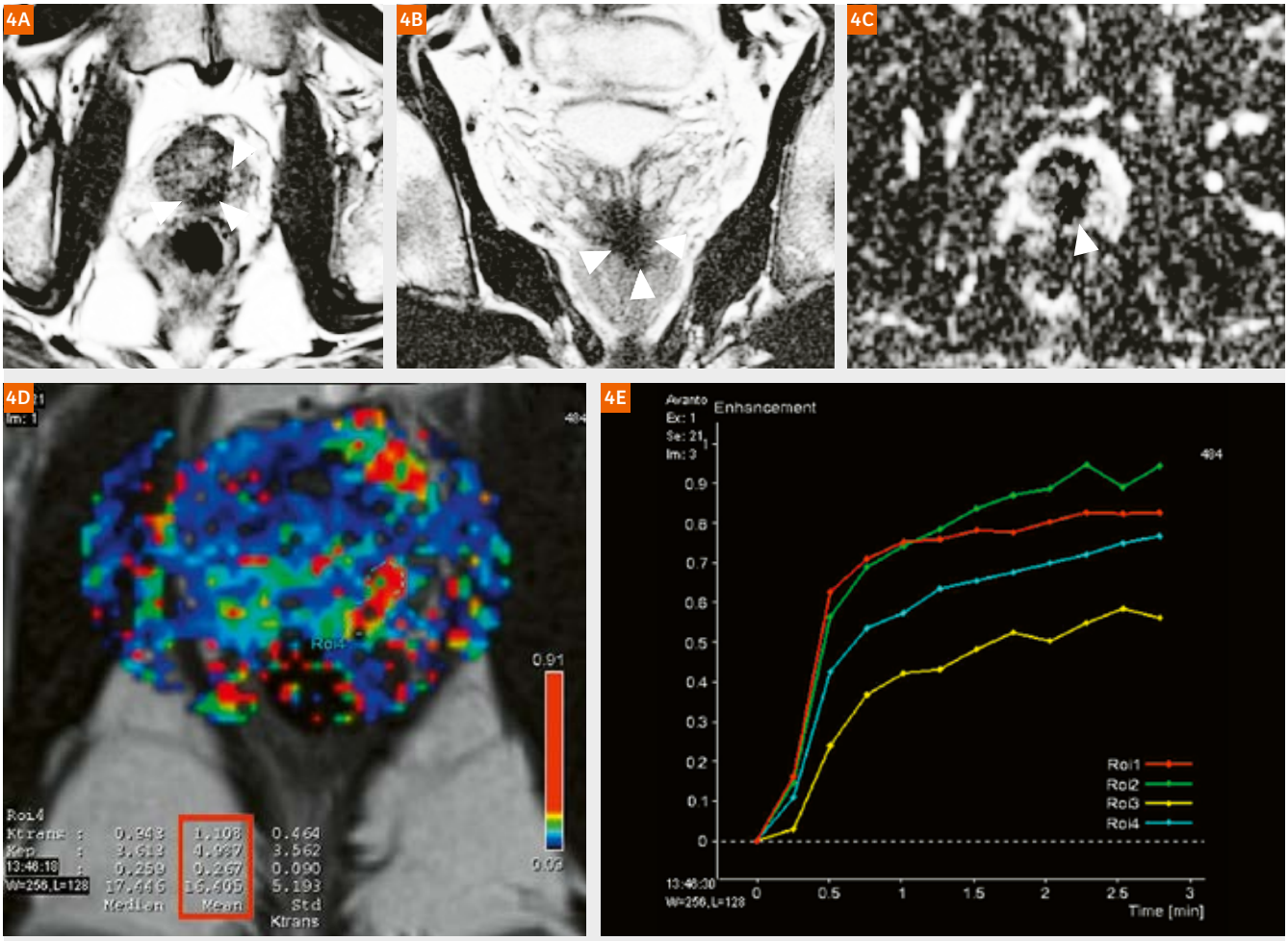

Figure 4: Seminal vesicle involvement.

4A) Axial T2w image, showing a diffusely T2 hypointense prostate parenchyma, which lowers the accuracy for finding focal suspicious areas. There is although an overtly hypointense focus involving the proximal ejaculatory ducts (arrowheads), raising awareness for seminal vesicle extension.
4B) Coronal T2w image, nicely showing the suspicious area, with clear involvement of both seminal vesicles.
4C) ADC map, showing restricted diffusion on the same area.
4D) K_{trans} map overlaid in T2w image, where a focal area of increased permeability (light-blue ROI) is seen, in keeping with the T2 hypointense lesion seen in 4A, also showing quantitative data (red rectangle).
4E) The lesion enhancement curve (red) is the steeper, with tendency to form a plateau rather than to keep on increasing.

Discussion

Functional prostate MR imaging, including DWI, DCE, and 3D multi-voxel spectroscopy, is largely turning into the mainstay in prostate cancer detection, staging and follow-up. The results among various institutions bear good to optimal correlation with histopathology, depending on the scanner's field strength (1.5T x 3T), the kind of coil employed (surface only x surface + endorectal), and also the gold standard utilized (biopsy x routine histopathology x whole-mount histopathology).

In this context, there's a tendency pointing towards studies on 3T prostate MR, with the combination of surface and endorectal coils, compared with whole-mount histopathology, in order to ally the most recent technology with the highest theoretical spatial resolution achievable.

However, this approach creates a potential dilemma for health care providers, public health authorities and general radiology departments, considering that PCa is the most prevalent neoplasm in men, and the availability of 3T scanners worldwide still does not match the demand for diagnosis, staging and follow-up for this condition. Despite the most recent technological advances, an alternative should be pursued for MR imaging of PCa, that allies cost-effectiveness and scanner availability with acceptable diagnostic accuracy, in order to extend the benefits of the

technique to the overall population, which is still being managed based on PSA and rectal exam alone.

Also, the endorectal coil (ERC) is another barrier to the acceptance of prostate MR. Although being of undisputedly better performance than surface coil alone on tumor localization, patient refusal due to cultural identity is still a major issue, most notably in Latin and Asian/Arabic countries. It requires specially trained personnel for proper placement, and considerably increases table time, not to mention the deformation produced on the prostate, that compromises radiotherapy planning and follow up studies. Particularly in Brazil, there is also an economical problem, for the ERC, which is disposable and for one use only, is not reimbursed by any of the health insurance companies or the public health system.

Giving those circumstances, and considering that our institutions are localized in a developing country, we initiated a long-term prospective research project aiming to create a prostate MR protocol that is feasible in most of the already worldwide installed 1.5T scanners, without the need of an endorectal coil or specially trained personnel, with optimized table time, and bearing acceptable diagnostic accuracy for relevant staging parameters, to be applied in large populational studies.

We also believe that newer post-processing tools for functional sequences, producing parametric color maps and fusions of functional and anatomic images, may further add to the diagnostic performance and to the communication of results to the referring physicians. Preliminary results indicate a promising performance of this protocol on presurgical staging of PCa. Further patients will be included, and the upcoming results will be accordingly published.

Contact

L. Kayat Bittencourt, M.D.
CDPI & Multi-Imagem

Rio de Janeiro
Brazil
lkayat@gmail.com

References

1 Ross R, Harisinghani M. Prostate cancer imaging – what the urologic oncologist needs to know. Radiol Clin North Am 2006; 44:711-722, viii.
2 Somford DM, Futterer JJ, Hambrock T, Barentsz JO. Diffusion and perfusion MR imaging of the prostate. Magn Reson Imaging Clin N Am 2008; 16:685-695, ix.
3 Jung JA, Coakley FV, Vigneron DB, et al. Prostate depiction at endorectal MR spectroscopic imaging: investigation of a standardized evaluation system. Radiology 2004; 233:701-708.
4 Futterer JJ, Heijmink SW, Scheenen TW, et al. Prostate cancer localization with dynamic contrast-enhanced MR imaging and proton MR spectroscopic imaging. Radiology 2006; 241:449-458.
5 Bloch BN, Furman-Haran E, Helbich TH, et al. Prostate cancer: accurate determination of extracapsular extension with high-spatial-resolution dynamic contrast-enhanced and T2-weighted MR imaging – initial results. Radiology 2007; 245:176-185.
6 Weinreb JC, Blume JD, Coakley FV, et al. Prostate cancer: sextant localization at MR imaging and MR spectroscopic imaging before prostatectomy – results of ACRIN prospective multi-institutional clinicopathologic study. Radiology 2009; 251:122-133.
7 Langer DL, van der Kwast TH, Evans AJ, Plotkin A, Trachtenberg J, Wilson BC, Haider MA. Prostate tissue composition and MR measurements: investigating the relationships between ADC, T2, K(trans), v(e), and corresponding histologic features. Radiology. 2010 May;255(2):485-94.
8 Turkbey B, Pinto PA, Mani H, Bernardo M, Pang Y, McKinney YL, Khurana K, Ravizzini GC, Albert PS, Merino MJ, Choyke PL. Prostate cancer: value of multiparametric MR imaging at 3 T for detection – histopathologic correlation. Radiology. 2010 Apr;255(1):89-99.
9 Groenendaal G, Moman MR, Korporaal JG, van Diest PJ, van Vulpen M, Philippens ME, van der Heide UA. Validation of functional imaging with pathology for tumor delineation in the prostate. Radiother Oncol. 2010 Feb;94(2):145-50.
10 Langer DL, van der Kwast TH, Evans AJ, Trachtenberg J, Wilson BC, Haider MA. Prostate cancer detection with multi-parametric MRI: logistic regression analysis of quantitative T2, diffusion-weighted imaging, and dynamic contrast-enhanced MRI. J Magn Reson Imaging. 2009 Aug;30(2):327-34.
11 Franiel T, Lüdemann L, Rudolph B, Rehbein H, Stephan C, Taupitz M, Beyersdorff D. Prostate MR imaging: tissue characterization with pharmacokinetic volume and blood flow parameters and correlation with histologic parameters. Radiology. 2009 Jul;252(1):101-8.
12 Ren J, Huan Y, Wang H, Ge Y, Chang Y, Yin H, Sun L. Seminal vesicle invasion in prostate cancer: prediction with combined T2-weighted and diffusion-weighted MR imaging. Eur Radiol. 2009 Oct;19(10):2481-6.
13 Fütterer JJ, Barentsz JO, Heijmink SW. Value of 3-T magnetic resonance imaging in local staging of prostate cancer. Top Magn Reson Imaging. 2008 Dec;19(6):285-9.
14 McMahon CJ, Bloch BN, Lenkinski RE, Rofsky NM. Dynamic contrast-enhanced MR imaging in the evaluation of patients with prostate cancer. Magn Reson Imaging Clin N Am. 2009 May;17(2):363-83.

Tissue 4D on *syngo*.via

Anja Fernandez Carmona; Radim Chrastek

Siemens Healthineers, Erlangen, Germany

Introduction

The Tissue 4D workflow facilitates the detection of tumors in organs, including the liver and prostate. It is a *syngo*.via workflow for reading and post-processing of dynamic contrast-enhanced 3D datasets. Tissue 4D describes the exchange of contrast agents between blood and tissue.

The MR Tissue 4D workflow provides two methods of evaluation:

1) A quantitative method following the Tofts model [1]. The Tofts model is based on the following parameters:

- K^{trans} (transfer constant)
- V_e (extra-vascular extra-cellular volume fraction)
- K_{ep} (reflux constant)

2) A qualitative evaluation method to retrieve the following parameters:

- **In** (Wash-in: enhancement in the tissue due to contrast uptake in a defined time interval)
- **Out** (Wash-out of contrast agent in a defined time interval)
- **TTP** (Time-to-Peak: time until the contrast enhancement reaches the highest concentration and wash-out starts)
- **AT** (Arrival time: time point when contrast enhancement starts)
- **PEI** (Positive Enhancement Integral: Value of concentration when the contrast enhancement reaches its highest concentration and wash-out starts)
- **iAUC** (initial Area Under Curve in 60 seconds)

Precondition and preparation

To evaluate and read data with the Tissue 4D workflow, the following series are required or recommended:

- Dynamic contrast-enhanced images with fixed flip angle (required)
- Pre-contrast series with variable flip angle to calculate the T1-map (recommended)
- Corresponding morphological images (recommended)

To start the evaluation, the images need to be assigned to a specific workflow template. The workflow template offers a sequence of pre-configured workflow steps. The workflow template can be selected according to the anatomical region.

Currently, there are two options for opening the image data:

- Tissue 4D only
- Prostate reading workflow with integrated Tissue 4D tab card

Post-processing steps can be highly automated if the steps have been properly pre-configured. To do so you have to be locked in as clinical administrator.

1

Morphological image: (optional)
- TSE for prostate
- Can be anything T1 or T2-weighed

→ Anatomical **orientation**

Pre-contrast measurement: (optional)
- VIBE with at least 2 different flip angles

→ Estimation of pixelwise **T1**

Dynamic measurement:
- VIBE or
- TWIST
- TWIST-VIBE
- GRASP-VIBE

→ With T1 and contrast agent relaxivity: yields **concentration**

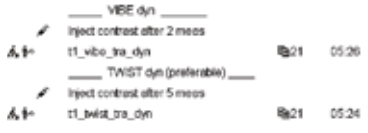

Figure 1: Acquisition protocol.

For the initial configuration open the Tissue 4D workflow with data in 'read only' mode. Once the case is opened, select the wrench icon in the workflow area for the Tissue 4D properties.

The configuration dialog 'Data Definition' allows to specify a series description for all data types, i.e. morphology, pre-contrast and dynamic series. All series that contain the given string are considered for automated case preparation. If there is more than one matching series for a data type, the latest series is used first.

Hint: The more precise the data type selection string is defined, the potentially shorter the case preparation time. This is because the case preparation is applied to all matching series, although the latest series is presented first.

After a reassignment of the Tissue 4D workflow the configuration settings are applied.

An advanced functionality of Tissue 4D is automated alignment of data types, configurable in the 'Preprocessing' and 'Alignment' dialog. Automatically selected reference time phase of the dynamic data type serves as a reference for all alignment algorithms. For all three data types, there is an option 'None'. The option deactivates the alignment for the given data types.

All alignment algorithms, including motion correction for the dynamic data types, are based on an elastic registration. This kind of registration provides transformation for each individual pixel. The advantage of the approach is that local changes, e.g. due to breathing, can be mapped correctly without having to correct organ or bone positions not affected by the local motion. Generally, the registration provides a transformation of one data type to the other, so that the image pixels are displayed in the same geometrical position for both data sets. The image pixel values are interpolated if they do not match the grid of the original image. The 'Alignment' configuration dialog serves for expert settings and it is not recommended to change these configuration values.

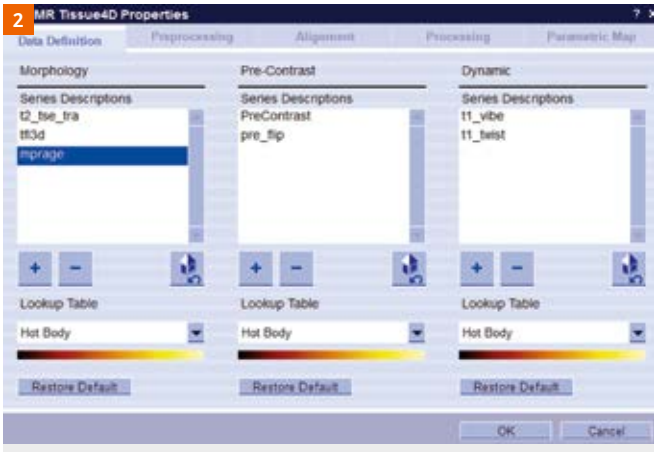

Figure 2: MR Tissue 4D properties.

'Preprocessing' allows the choice between two pharmacokinetic models: 'Qualitative' or 'Tofts'. The latter requires the type of the Arterial Input Function (AIF), see below. Since the automated case preparation might take long for entire 3D datasets, the calculation is constrained to a 'volume-of-interest' (VOI). The VOI is defined by the center and radius for each direction, i.e. x, y, z. The center is given by the percentage of the 3D volume size. The default values are 50% for all three directions, i.e. the x, y, and z coordinates are exactly in the middle of the 3D volume. The radius is also given by the percentage of the 3D volume size. The smaller the VOI, the potentially faster the pharmacokinetic model calculation, especially for the Tofts model.

Evaluation and reading

Once the Tissue 4D properties have been configured, the case can be assigned and opened with the specific workflow template. Here is what you will see:

Motion correction step
You can use this step to verify the automatic alignment of the dynamic data set to a defined reference volume.

Time point slider

The time point slider visualizes the available time points in the dynamic data set. The current reference time point (reference volume) for motion correction is indicated by a small blue triangle.

Selecting a new reference time point:

In the **Case Navigator**, click the slider and move it to the required time point. Click this icon to confirm the new reference time point. The blue triangle jumps to the new reference time point and the display in the image segments is updated accordingly.

Hint: Before you can change the reference time point you have to turn off motion correction.

The Motion Correction step is used to align the dynamic dataset to a defined reference volume.

In the **Case Navigator**, click this icon to turn the motion correction on or off. Motion correction is applied in all other volumes of the dynamic data set according to the reference time point.

You can delete time points from the current data set if, for example, the quality is not sufficient for the evaluation.

In the **Case Navigator**, click the slider and move it to the required time point. Click this icon to delete a specific time point.

Or click this icon to delete all time points after the selected time point (to the right side).

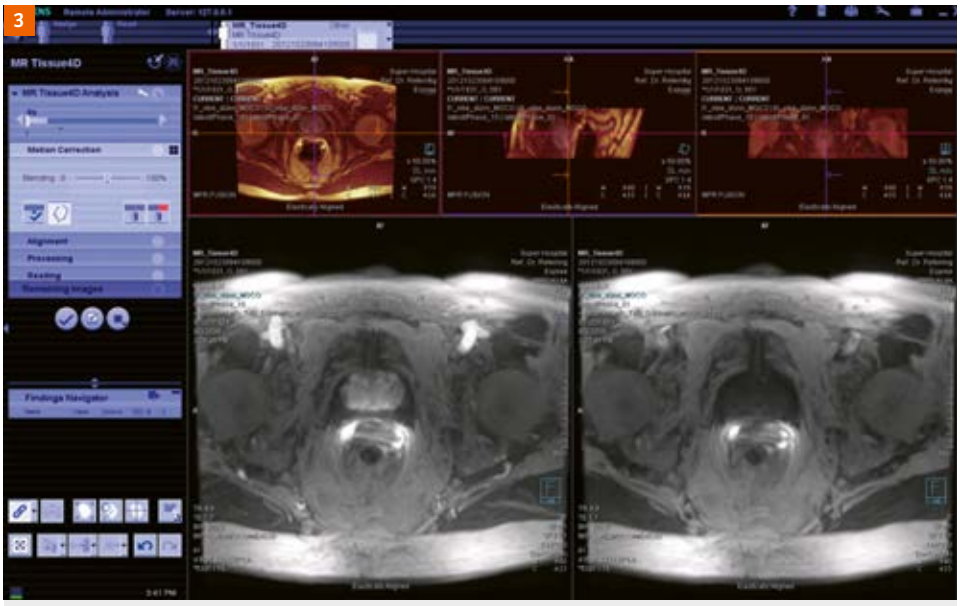

Figure 3: The top row shows the fusion of current phase and reference phase. The images are displayed using the multi-planar reconstruction (MPR) volume rendering technique. If you navigate to the reference phase, only this reference phase is shown, without fusion.

The bottom row shows the reference phase (left) and the current phase (right) using mean intensity projection (MIP) volume rendering technique.

Alignment step
Here you see only the configured and available series. On a single monitor configuration the upper part shows the morphology aligned to the dynamic and the lower part the pre-contrast to the dynamic series.

In most cases the automatic alignment works fine and you can proceed directly to the next step. If, however, you are not satisfied with the alignment you can change it by using the visual alignment tool in the upper left corner menu.

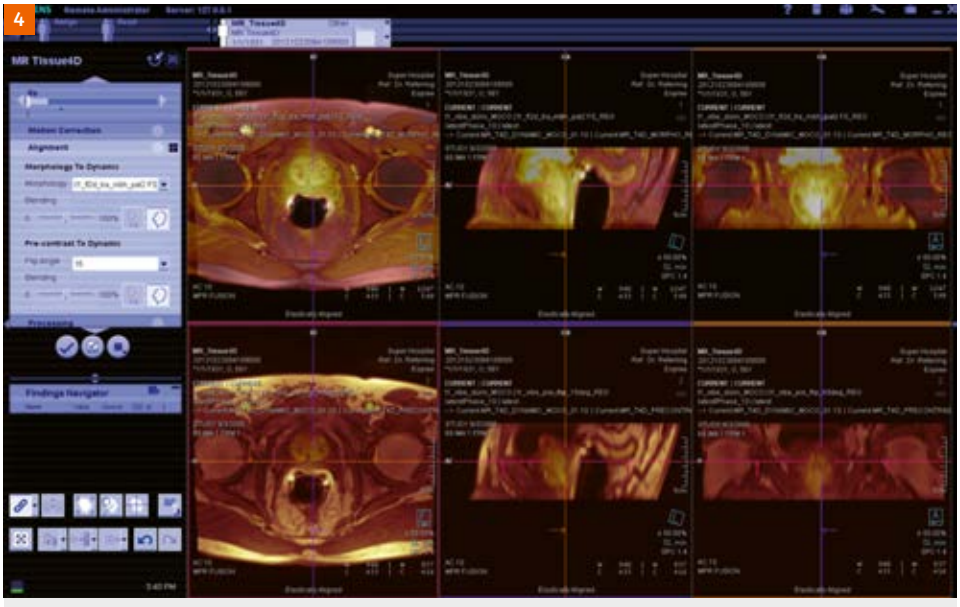

Figure 4: Alignment.

Figure 5: Alignment menu.

To verify the correctness of the alignment you can use the blending mode. Move the slider to the left and right side.

Before you can change the alignment you have to turn motion correction off.

 Moco on

 Moco off

There are different alignment modes:

- Automatic rigid: the entire volume is transformed. The transformation obtained by the registration algorithm is the same for all pixels. No local deformation can be compensated (such as breathing)
- Visual: you can shift and rotate the volumes
- Elastic: can compensate local deformations

Processing step

Here you can modify the pharmacokinetic modeling. You can change between Tofts and qualitative model, and also define the evaluation volume.

The qualitative model matches three lines to the measured concentration curve for each voxel within the VOI. It does not require any parameters. The first line fits the baseline phase, i.e. before contrast agent arrival. The second line fits the wash-in phase, i.e. it displays the enhancement in the tissue due to contrast uptake in a defined time interval t. The third line fits the wash-out phase. The graph in the top right-hand corner shows the mean concentration curve for the entire VOI, together with the correspondingly fitted three lines.

The Tofts model matches a mathematical model defined by [1] to the measured concentration curves for each voxel within the VOI. Also for this model, a graph with the mean curve for the entire VOI is displayed in the top right-hand corner.

The selectable parameter for the Tofts modeling, the AIF, is based on mathematical simulation, slow [4], intermediate [3], and fast [2]. If you are not sure which AIF to use, the chi2 parameter might help. The chi2 parameter is an error measure of the fit. The smaller the parameter, the better the fit.

Recommendation: keep the size of the VOI as small as possible. The larger the VOI, the potentially longer the pharmacokinetic model calculation, especially for the Tofts model.

Figure 6: Processing step qualitative.

Figure 7: Processing step quantitative.

Figure 8A: Measurement icons.

Figure 8B: Description icons.

Figure 9A: To create findings in Tissue 4D you need to enable 'AutoCollect'.

Figure 9B: Export icon.

Reading step

The last step enables you to read the resulting maps and create findings for your report.

Here are different Tissue 4D reading tools available to evaluate the mean and the standard deviation in a selected area.

In the upper right segment these curves are displayed.

To create findings in Tissue 4D workflow you need to enable the 'AutoCollect' button. Manual findings creation is only possible via snapshots.

Export of results:
You can export reading results as text file (csv-files). The export icon (Fig. 9B) is context sensitive and exports the results of the selected segment.

Summary

This article describes the current version of the Tissue 4D for DCE evaluation. Case preparation can be highly automatized, allowing you to concentrate on the reading. The automatic case preparation takes care of the selection of the data types, their alignment to the reference phase of the dynamic data type and pharmacokinetic model calculation. You only have to verify the results of the automatic case preparation. Once done, you can immediately start reading. The results can be then exported to csv format. All documented findings, i. e. collected in the Findings Navigator, are automatically stored as DICOM Structured Report once the workflow has been completed.

References

1 Tofts P. T1-weighted DCE Imaging Concepts: Modelling, Acquisition and Analysis. MAGNETOM Flash 2010;3:31-39.
2 Orton MR, d'Arcy JA, Walker-Samuel S, Hawkes DJ, Atkinson D, Collins DJ, Leach MO. Phys Med Biol. 2008 Mar 7;53(5):1225-39. Computationally efficient vascular input function models for quantitative kinetic modelling using DCE-MRI.
3 Parker GJ, Roberts C, Macdonald A, Buonaccorsi GA, Cheung S, Buckley DL, Jackson A, Watson Y, Davies K, Jayson GC. Magn Reson Med. 2006 Nov;56(5):993-1000. Experimentally-derived functional form for a population-averaged hightemporal-resolution arterial input function for dynamic contrast-enhanced MRI.
4 Weinmann H, Laniado M, Mutzel W. Physiol Chem Phys Med NMR. 1984; 6(2):167-72. Pharmacokinetics of GdDTPA/dimeglumine after intravenous injection into healthy volunteers.

Contact

Anja Fernandez Carmona
Siemens Healthcare
HC DI MR R&D SW VIA-APM

91050 Erlangen
Germany
Phone: +49 (9131) 84-3566
anja.fernandez_carmona@siemens-healthineers.com

The Metabolite Ratio in Spectroscopic Imaging of Prostate Cancer

Alan J. Wright; Thiele Kobus; Arend Heerschap; Tom W. J. Scheenen

Radboud University Nijmegen Medical Centre, Radiology Department, Nijmegen, The Netherland

Introduction

Prostate cancer is the second leading cause of cancer related death in Western countries [1]. The prevalence of the disease is very high, but many men diagnosed with the disease will die from unrelated causes. This is because prostate cancer very often is a disease of old age that grows slowly. Common treatment for prostate cancer in clinical practice involves radical resection of the entire gland or radiotherapy with a dose distributed over the whole organ. Provided that the cancer has not metastasized, these therapies are curative, though concern over their side effects has led to patients and their doctors delaying this treatment and, instead, entering into active surveillance or watchful

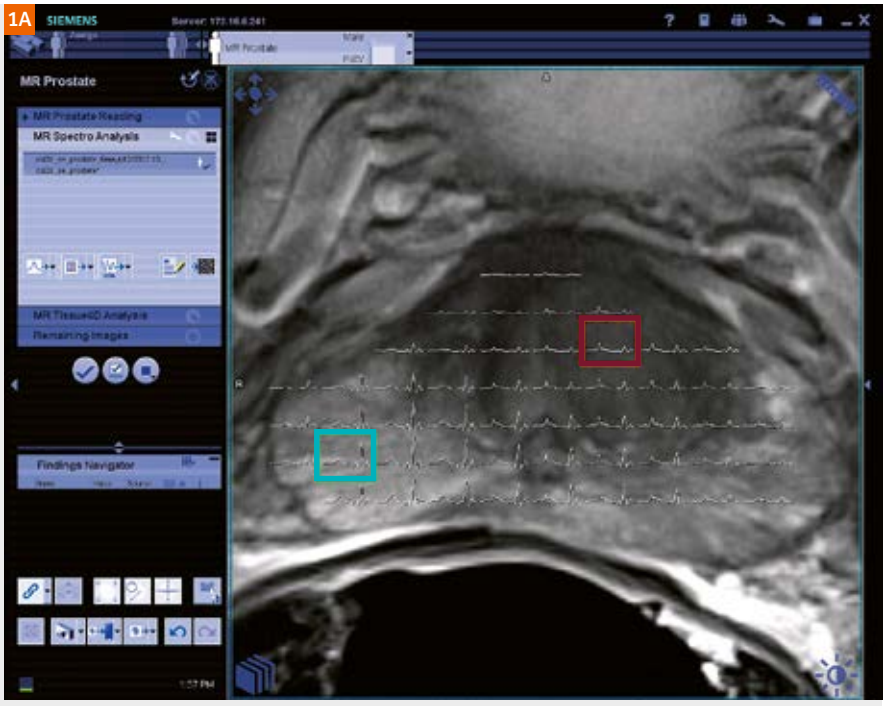

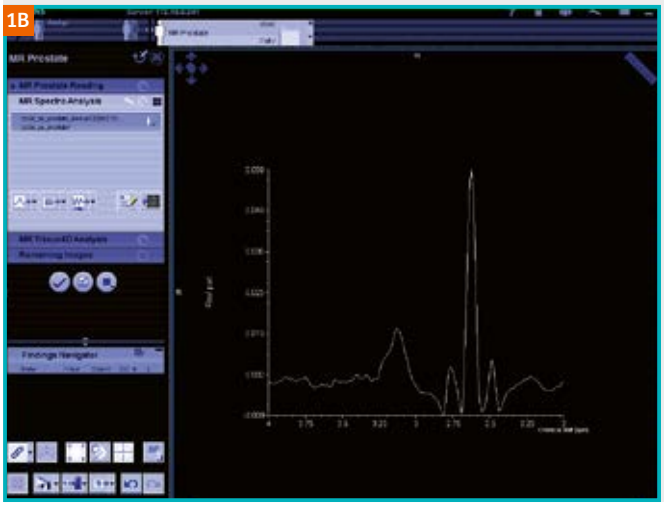

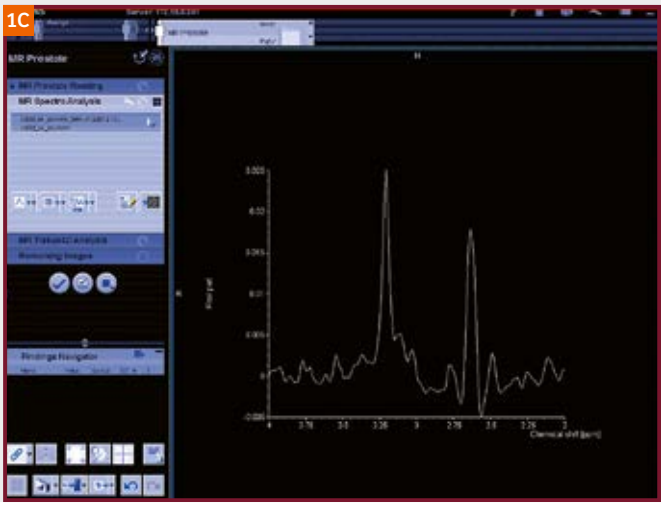

Figure 1A: T2-weighted MR image of a transverse section through a prostate with an overlaid grid of MRSI spectra from voxels within the prostate.

Figure 1B: One example spectrum shown on a ppm scale from a region of benign prostate tissue.

Figure 1C: A spectrum from another voxel that, in this case, co-localises to a region of tumor.

waiting programs. In order for patients to safely forgo curative treatment, it is essential to characterize their disease: to determine that it is sufficiently benign that growth will be slow and metastasis improbable. Selecting these patients, with low risk disease, that are appropriate for active surveillance requires accurate diagnosis of not just the presence of tumor, but how aggressive it is: i.e. how fast it is growing and how likely it is to metastasise to the lymphatic system. Magnetic resonance imaging (MRI) is an emerging technique for making this patient selection. It can diagnose the presence of tumor, localize it in the organ and provide information as to how aggressive it is. The MRI exams employed for this purpose usually involve multiple imaging sequences including a T2-weighted sequence, diffusion-weighted imaging (DWI) and one or more further techniques such as dynamic contrast enhanced MRI (DCE-MRI) or Proton Magnetic Resonance Spectroscopic Imaging (^{1}H MRSI) [2]. Radiologists can read the different imaging modalities to decide the location, size and potential malignancy of the tumor which are all indicators of its metastatic potential. Acquiring and reporting imaging data in this way is known as multiparametric (mp) MRI. MRSI is the only mpMRI methodology that acquires data from molecules other than water [19]. A three dimensional (3D) ^{1}H MRSI data set consists of a grid of spatial locations throughout the prostate (see Fig. 1) called voxels. For each voxel a spectrum is available. Each spectrum consists of a number of peaks on a frequency axis, corresponding to resonances from protons with a certain chemical shift in different molecules. The size of a peak at a certain frequency (chemical shift) corresponds to the amount of the metabolite present in the voxel. In this way MRSI measures the bio-chemicals in regions of tissue *in vivo* without the need for any external contrast agent or invasive procedures. Examples of spectra from two voxels, acquired at a magnetic field strength of 3 Tesla (3T), are given in figure 1B, C, which clearly shows the differing profiles that are characteristic of benign prostate tissue and its tumors.

Important metabolites in prostate MRSI

The initial papers on *in vivo* prostate MRSI were performed at a magnetic field strength of 1.5T [3–5], and three assignments were provided for the observed resonances: choline, creatine and citrate (Fig. 2). The small number of these assignments reflected the simplicity of the spectrum, which contained two groups of resonances: one in the region of 3.3 to 3 ppm, which will be referred to as the choline-creatine region, and another at 2.55–2.75 ppm, which shall be called the citrate group. These assignments related to what were believed to be the strongest metabolite resonances. People should be aware however, that the assignments are representative of multiple similar molecules. The choline assignment reflects the methyl resonances from multiple compounds containing a choline group (Fig. 4): choline, phosphocholine and glycerophosphocholine. Similarly, creatine refers to both creatine and phosphocreatine. In between the choline and creatine signals another group of resonances are present: the polyamines (mainly spermine and spermidine). The citrate resonances are from citrate only but can have a complicated shape, although *in vivo* at 1.5T they give the appearance of a single peak. Nowadays a magnetic field strength of 3T is used more and more for prostate spectroscopic imaging, which gives opportunities to better resolve the choline, polyamines, creatine resonances, but also changes the shape of the citrate signal.

Larger choline signals are associated with tumor in nearly all cancers [6]. High choline signals are interpreted as being evidence of rapid proliferative growth and, more directly, the increased membrane turnover required for cell division. Membranes contain phospholipids: phosphatidyl choline and phosphatidyl ethanolamine, which are synthesised by a metabolic pathway involving choline-containing metabolites known as the Kennedy pathway. It is in the synthesis and catabolism of these products, upregulated in proliferative tumor growth, that causes the increase in these signals.

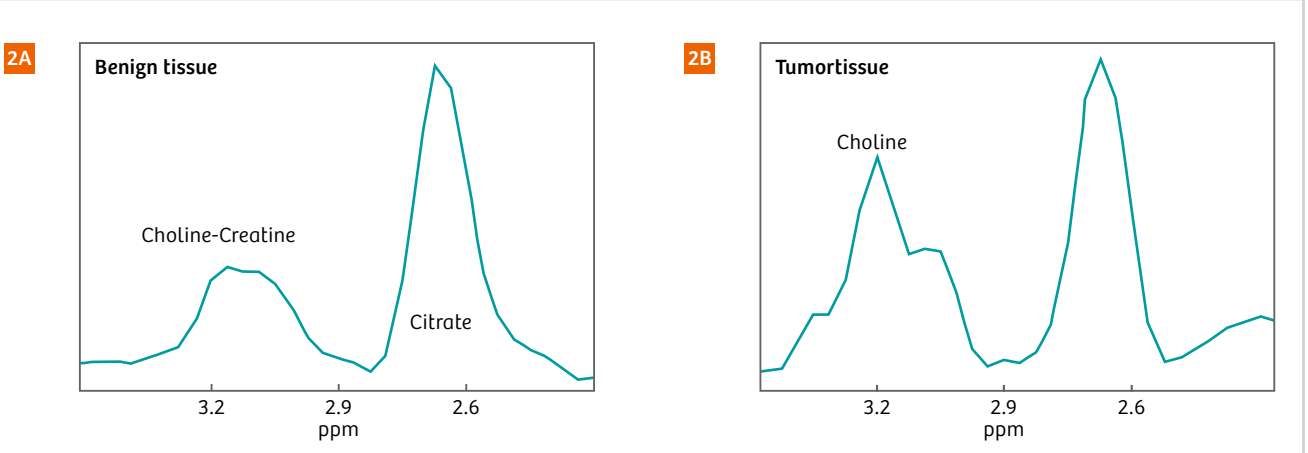

Figure 2: Examples of ^{1}H MRSI spectra acquired from benign prostate tissue and tumor at 1.5T.

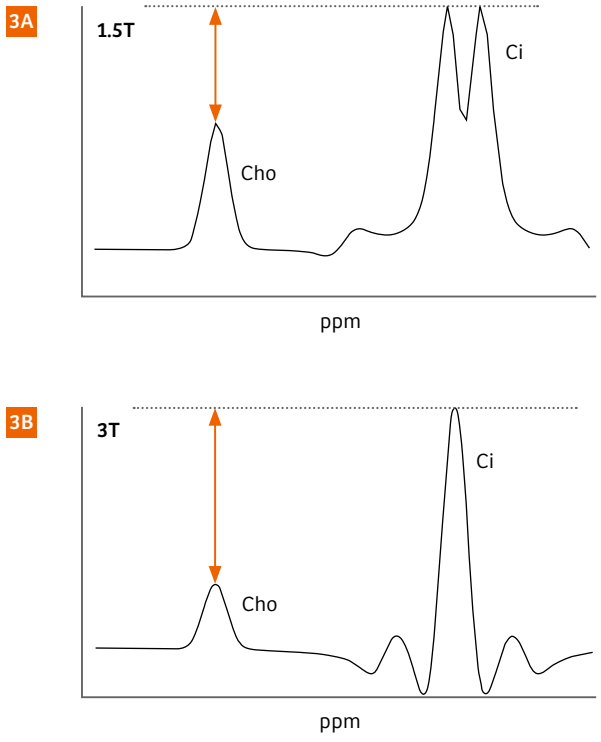

Figure 3: Simulated spectral shape of Cho and Ci for typical echo times (120 ms at 1.5T, 145 ms at 3T). Identical concentrations, i.e. scale factors, are applied, but different line broadening of the signals (4 Hz at 1.5T; 8 Hz at 3T). Note the difference in the spectral shape of Ci and the different peak amplitude ratios for Cho/Ci.

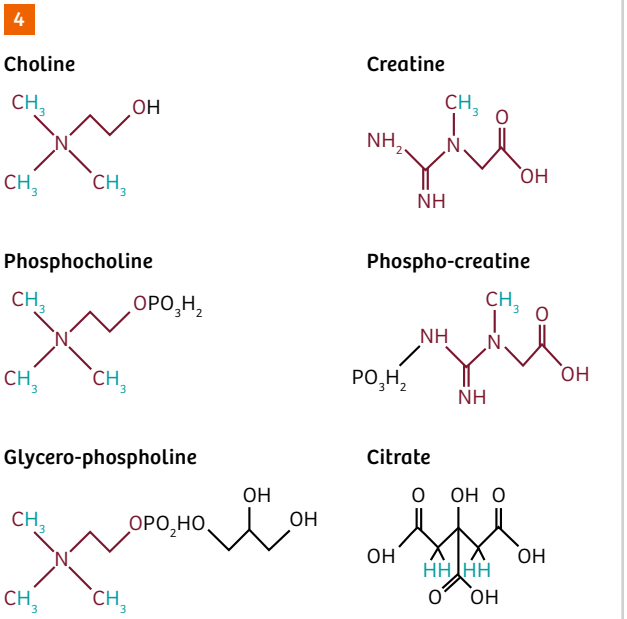

Figure 4: Structural formulas of the key small molecule metabolites observed in the spectra of prostate tissue. For each group, cholines and creatines, the common moiety is highlighted in red. The protons that give the MR spectral resonances present in the choline-creatine region are indicated in petrol. Choline-containing metabolites have 9 co-resonant protons in the region 3.2–3.25 ppm. Creatines have three co-resonant protons at 3.05 ppm. Citrate has four protons that resonate at two chemical shifts (2.6 and 2.7 ppm), one for each proton in a pair bonded to the same carbon. This pair also has a coupling between them and the symmetry of the whole molecule ensures that two protons co-resonate at each frequency.

The large amplitude of citrate resonances observed in prostate tissue is due to an altered metabolism particular to this gland. Prostate tissue accumulates high concentrations of zinc ions which inhibit mitochondrial aconitase, leading to a build up of citrate in the prostate's epithelial cells [7]. This citrate is further secreted into the ductal spaces of the prostate as part of prostatic fluid, which has a high concentration of this metabolite. Prostate carcinomas do not accumulate zinc ions, so they do not have this high citrate concentration. The increased presence of tumor cells within a ^{1}H MRSI voxel can, therefore, have two diminishing effects on the observed citrate signals: epithelial cells that accumulate citrate can transform into, or be replaced by, tumor which has low citrate, or the lesion can grow through the ductal spaces, thus displacing the prostatic fluid. The relative contribution of each of these two physiological changes, whether we are observing tumor formation and malignant progression or a histological change in tumor invasion of ductal structure, is not yet known. It is, however, clear that there is an inverse correlation of the levels of citrate metabolite and tumor cell density with some evidence to support a similar correlation with the aggressiveness of the tumor as well [8].

The introduction of a metabolite ratio

To transform the described changes in choline and citrate signals between benign (high citrate) and tumorous tissue (low citrate, high choline) into a marker for prostate cancer, the metabolite ratio was introduced [3–5]. The signal intensities of the different spectral peaks were quantified by simple integration of the two groups of resonances (the choline-creatine region and the citrate group), and the results were expressed as a ratio of the two. This gave the choline plus creatine over citrate ratio (abbreviated to CC/C [4]) or its inverse (with citrate as the numerator, [3, 5]). With choline in the numerator and citrate in the denominator, it became a positive biomarker for the presence of cancer.

Acquiring the MRSI data sets

As the prostate is embedded in lipid tissue, and lipids can cause very strong unwanted resonance artefacts in prostate spectra, the pulse sequence to acquire proton spectra is equipped with five properties to keep lipid signals out and retain optimal signals-of-interest in the whole prostate [9].

1. Localization of the signal with slice-selective pulses. The point resolved spectroscopy sequence (PRESS) is

a combination of one slice selective excitation pulse and two slice selective refocusing pulses leading to an echo at the desired echo time. The three slices are orthogonal, producing an echo of the volume-of-interest (crossing of three slices) only.

2. Weighted acquisition and filtering. Proton MRSI data sets are acquired using a phase encoding technique where the gradients across spatial dimensions are varied with each repeat of the pulse sequence. By using weighted averaging of these phase encoding steps (smaller gradient steps are averaged more often than larger gradient steps) and adjusted filtering of the noise in these weighted steps, the resulting shape of a voxel after the mathematical translation of the signal into an image (Fourier Transform) is a sphere. Contrary to conventional acquisition without filtering, the spherical voxels after filtering are not contaminated with signals from non-neighboring voxels.
3. Frequency-selective water and lipid suppression. The pulse sequence has two additional refocusing pulses that only touch upon water and lipid signals. Together with strong crushing gradients, signals from water and lipids are suppressed.
4. Outer volume suppression. Around the prostate, slice-selective pulses can be positioned to suppress all signals in the selected slabs. These slices can be positioned quite close to the prostate, even inside the PRESS-selected volume-of-interest.
5. Long echo time. To accommodate all localization and frequency selective pulses, the echo time of ^{1}H MRSI of the prostate is around 120 ms at 1.5T and 145 ms at 3T. At longer echo times, lipid signals decay due to their short T2 relaxation time.

The prostate is small enough (< 75 cubic centimetres) to allow a 3D ^{1}H MRSI data set to be acquired, with complete organ coverage, within 10 minutes of acquisition time. The nominal voxel size is usually around 6 x 6 x 6 mm, which after filtering as described above results in a true voxel size of 0.63 cm^{3}.

Spectral patterns

Due to multiple different protons in the molecule, a single metabolite can have multiple resonances. If interactions exist between protons within a metabolite, the shape of a spectral peak can be complicated. A resonance group of protons that has a mixture of positive and negative parts is said to have a dispersion component in its shape; a symmetrical-positive peak is referred to as an absorption shape. Choline and creatine resonances appear as simple peaks (singlets), although they very often cannot be separated from each other as they overlap within *in vivo* spectral linewidths. The structure of citrate, given in figure 4, results in protons at two different chemical shifts, with coupling between each proton and one other (a strongly coupled spin system). The spectral shape of these protons depends on their exact chemical shift, the coupling constant between them, the pulse sequence timing and the main magnetic field strength. At an echo time of 120 ms at 1.5T (and a very short delay between excitation and first 180 degree refocusing pulse), the spectral peaks of citrate are close to a positive absorption mode. The spectral shape consists mainly of an inner doublet with small side lobes on the outer wings. Together with line broadening the citrate protons quite closely resemble a single, somewhat broadened peak. The small side lobes around this peak are hardly detectable over the spectral noise *in vivo*. At 3T with an echo time of 145 ms (examples given in Fig. 1), the negative dispersion components of the citrate shape cannot be ignored. Its side lobes are substantially larger and reveal also some negative components [10]. Therefore the area under the curve, the integral, is substantially smaller at 3T than at 1.5T. Because of its complicated shape, it is essential at 3T to incorporate this shape in quantification of the signal.

Signal quantification by integration or metabolite fitting

The size of the peaks of the individual resonances represent the amount of the metabolite present in the voxel. Integration provides a simple method to quantify the spectra, as long as all signals have an absorption shape. Although it cannot discriminate between overlapping resonances, as long as overlapping signals (choline and creatine) are summed in a ratio this does not matter. With clear separation between citrate resonances and the choline-creatine region, the CC/C ratio can be calculated. However, as pointed out earlier, the spectral shape of citrate is not straightforward, and ignoring the small satellites at 1.5T, or simply integrating the large dispersion parts of the signal at 3T, would inevitably lead to underestimation of the total citrate signal intensity. An alternative is to fit the spectra with models of the citrate resonances with their expected shape. The shape can either be measured, using a solution of citrate placed in the MRI system and a spectrum acquired with the same sequence as the *in vivo* data, or it can be calculated using a quantum mechanical simulation (Fig. 3). By this process of spectral fitting, models of each metabolite's spectral peaks are fit to the total spectrum and the intensities of each fitted model are calculated. A linear combination of the metabolite models is found by the fitting routine such that

$$\text{Data} = C_1 * \text{choline model} + C_2 * \text{creatine model} + C_3 * \text{citrate model} + \text{baseline} \quad \text{Eqn1.}$$

The coefficients C_{1-4} give the relative concentrations of the individual metabolites.

When fitting with *syngo*.via, the result of a fit to a spectral peak can be expressed in two ways: as an integral value, which describes the area under the fitted spectral peak, or as a relative concentration (incorporating the number of protons in the corresponding peak) of the metabolite, called the scale factor (SF) of the metabolite.

Figure 5A: T2-weighted MRI image of a transverse section through a prostate as shown in figure 1 with an overlaid grid of MRSI-voxel data displayed as fitted spectra.

Figure 5B, C: Two spectra (shown previously in figure 1) with their fitted model metabolite signals.

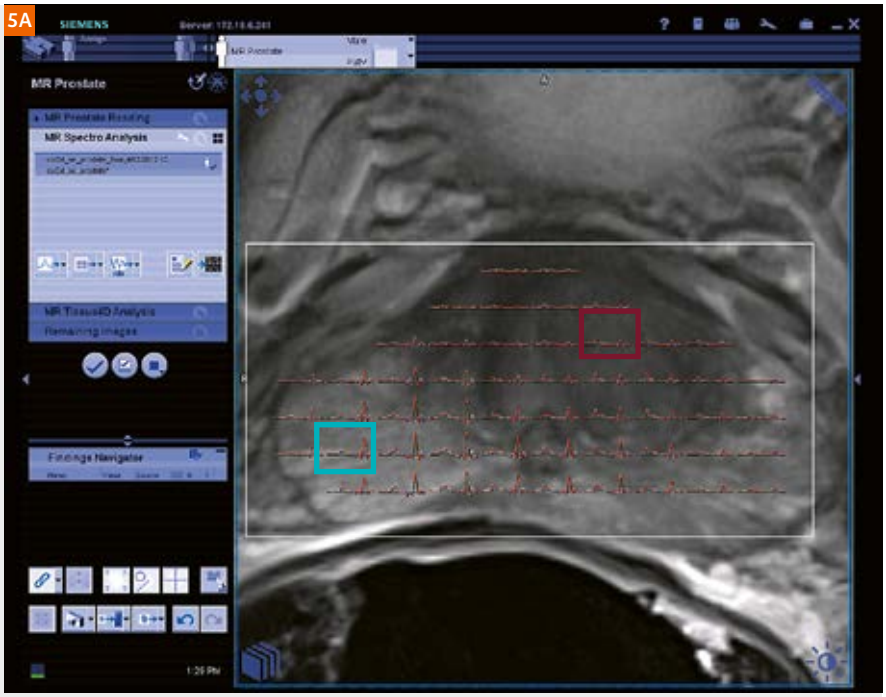

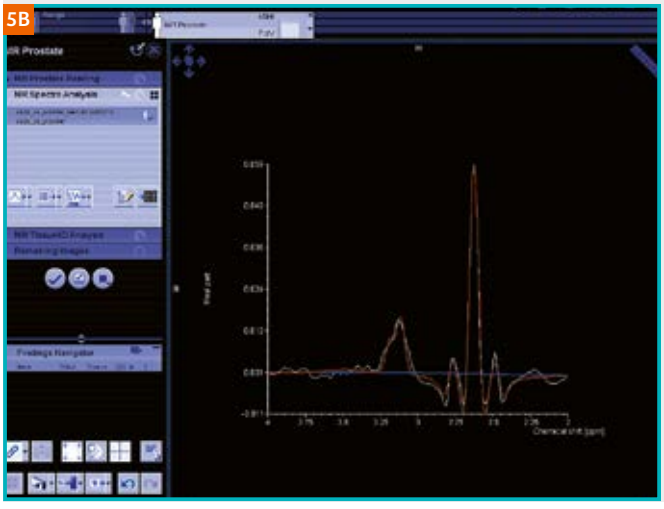

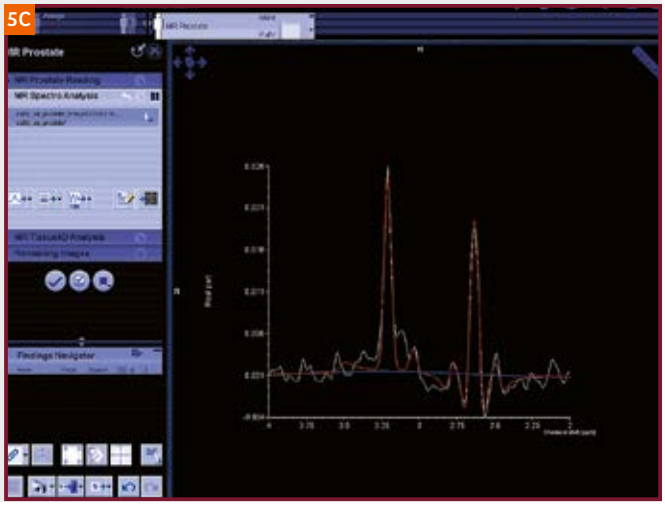

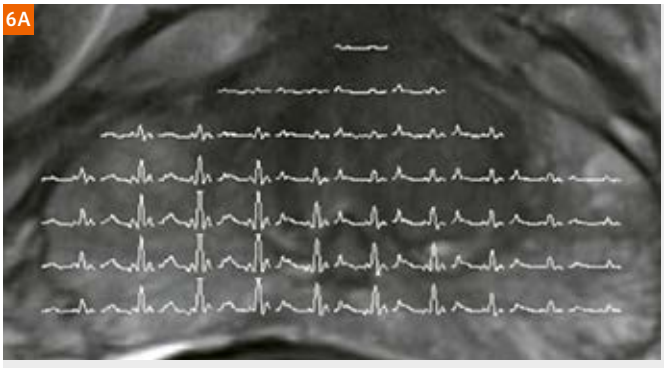

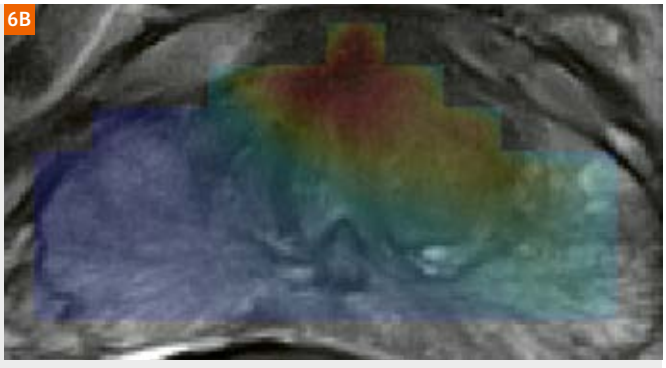

Figure 6: T2-weighted MR image of a transverse section through a prostate as shown in figure 1 with an overlaid grid of MRSI-voxel data displayed as spectra **(6A)** and as the pseudo integral CC/C ratio **(6B)** from metabolite fitting of the spectra. The ratio data points are interpolated and shown on a color scale of values from 0 (blue) to 3 (red). The tumor containing region of the prostate corresponds to the higher ratio values: the cyan-red area in the image.

As noted earlier, the integral value of citrate is different for 1.5 vs. 3 Tesla due to the different spectral patterns and would also change if pulse sequence timing other than standard would be used. If the scale factor is multiplied with the number of resonating protons (#H), it represents the intensity of a signal, in relation to the integral value of a pure singlet of one resonating proton in absorption mode. We call this entity pseudo integral, which is calculated as A.

pseudo integral (Metabolite) = #H * SF (Metabolite).

For citrate this pseudo integral is perhaps best described as the numerical integral of the magnitude (all negative intensity turned positive) of the citrate spectral shape, ignoring signal cancellations of absorption and dispersion parts of the shape.

The spectral fits are shown for the two spectra in figure 5 with model spectra of the three metabolites choline, creatine and citrate. It can be seen from these spectra that the relative amplitudes of the metabolites vary between the benign and the tumor spectrum. As expected, the benign spectrum has a higher citrate amplitude while the tumor has a greater choline amplitude, relative to the other metabolites. Combined in the CC/C ratio, the positive biomarker for the presence of tumor in the prostate is calculated.

Depending on the used quantification (spectral integration without fitting (a), fitted relative concentrations (b) or pseudo integrals (c)) the CC/C can be calculated by:

(a) {Integral(Choline) + Integral (Creatine)} / Integral(Citrate)

(b) {SF(Choline) + SF(Creatine) } / SF(Citrate)

(c) {9*SF(Choline) + 3*SF(Creatine)} / 4*SF(Citrate), respectively.

The numbers in the last equation correspond to the number of protons of the different signals. Generally, use of the pseudo integral ratio is strongly preferred, as it is least sensitive to large variations in individual metabolite fits in overlapping signals (choline and creatine). Note (again) that this pseudo integral ratio does not aim to provide a ratio of absolute metabolite concentrations, as this is very difficult with overlapping metabolite signals, partially saturated metabolite signals due to short TR (T1 effects), and variation in signal attenuation due to the use of a long echo time (T2 effects).

Now, what could be the effect on the ratio if further metabolites are included in the fitting? Could even polyamines be incorporated in the analysis [11]? After separate fitting, the main focus of the analysis could just be on choline and citrate, which have opposite changes in intensity with cancer, to make a simpler and potentially more sensitive choline/citrate ratio. Various metabolite ratios have been proposed [12, 13], and there is certainly value in using choline over creatine as a secondary marker of tumor malignancy that can give complementary information to the CC/C ratio [14–16]. However, any of these interpretations are limited by how well the individual metabolite resonances can be resolved. At 3T the choline, polyamines and creatine resonances all overlap (Figs. 1 and 5). In practice this lack of resolution in the spectrum translates to errors in the model fitting where one metabolite can be overestimated at the expense of another. For example a choline over citrate ratio could be underestimated if the polyamines fit was overestimated and accounted for some of the true choline signal. While acquisition and fitting methods are being actively researched to improve the individual quantification of these metabolites, it is more reliable to stick to the pseudo-integral CC/C ratio.

Once reliably calculated, the CC/C ratio combines the essence of the observable spectroscopic data into a single quantity that can be displayed on an image (Fig. 6), combining the key information into a simple to read form for radiological reporting.

Published values of the ratios for tumor and benign tissue, which are calculated in a similar way to the *syngo*.via fitting, are listed in table 1.

Future perspective of MRSI for prostate cancer

The CC/C ratio is the most used method for interpreting ^{1}H MRSI data of prostate and prostate cancer. It remains, essentially, the integral of the choline-creatine region divided by the citrate region, a simple combination of the metabolite information in a single-value marker that is sensitive to the presence of tumor. The use of areas under

Tissue	1.5 Tesla[1]	3 Tesla[2]
Non-cancer peripheral zone	0.28 (0.21– 0.37)	0.22 (0.12)
Non-cancer central gland[3]	0.36 (0.28–0.44)	0.34 (0.14)
Cancer	0.68 (0.43–1.35)	1.3 (3.7)

Table 1: Typical integral values of the CC/C ratio in prostate tissue at 1.5T [17] and pseudo integral values of CC/C at 3T [18].

[1] median and 25th and 75th percentile
[2] mean and standard deviation
[3] combined transition zone and central zone

the resonances in the ratio has the implication that the absolute value of this biomarker is largely dependent on the acquisition sequence used. Any change in field strength, the pulses or pulse timings will change resonance amplitude and shape due to T1 and T2 relaxations and the scalar couplings of especially citrate. Values of the ratio quoted in the literature for tumor or benign tissues depend strongly on how the ratio is actually calculated and are, therefore, often not directly comparable. However, using the Siemens-supplied default protocols for acquisition and *syngo*.via postprocessing enables one to make use of published values as given in table 1, and incorporate ^{1}H MRSI of the prostate into their clinical routine.

References

1 Siegel R, Naishadham D, Jemal A. Cancer statistics, 2012. CA Cancer J Clin 2012; 62(1):10-29.
2 Hoeks CMA, Barentsz JO, Hambrock T, Yakar D, Somford DM, Heijmink SWTPJ, Scheenen TWJ, Vos PC, Huisman H, van Oort IM, Witjes JA, Heerschap A, Fütterer JJ. Prostate Cancer: Multiparametric MR Imaging for Detection, Localization, and Staging. Radiology 2011; 261: 46 –66.
3 Heerschap A, Jager GJ, van der Graaf M, Barentsz JO, Ruijs SH. Proton MR spectroscopy of the normal human prostate with an endorectal coil and a double spin-echo pulse sequence. Magn Reson Med 1997;37(2):204-213.
4 Kurhanewicz J, Vigneron DB, Hricak H, Parivar F, Nelson SJ, Shinohara K, Carroll PR. Prostate cancer: metabolic response to cryosurgery as detected with 3D H-1 MR spectroscopic imaging. Radiology 1996;200(2):489-496.
5 Kurhanewicz J, Vigneron DB, Nelson SJ, Hricak H, MacDonald JM, Konety B, Narayan P. Citrate as an in vivo marker to discriminate prostate cancer from benign prostatic hyperplasia and normal prostate peripheral zone: detection via localized proton spectroscopy. Urology 1995;45(3):459-466.
6 Glunde K, Bhujwalla ZM, Ronen SM. Choline metabolism in malignant transformation. Nat Rev Cancer;11(12): 835-848.
7 Costello LC, Franklin RB. Novel role of zinc in the regulation of prostate citrate metabolism and its implications in prostate cancer. The Prostate 1998; 35(4):285-296.
8 Giskeodegard GF, Bertilsson H, Selnaes KM, Wright AJ, Bathen TF, Viset T, Halgunset J, Angelsen A, Gribbestad IS, Tessem MB. Spermine and citrate as metabolic biomarkers for assessing prostate cancer aggressiveness. PloS one;8(4):e62375.
9 Scheenen TW, Klomp DW, Roll SA, Futterer JJ, Barentsz JO, Heerschap A. Fast acquisition-weighted three-dimensional proton MR spectroscopic imaging of the human prostate. Magn Reson Med 2004;52(1):80-88.
10 Scheenen TW, Gambarota G, Weiland E, Klomp DW, Futterer JJ, Barentsz JO, Heerschap A. Optimal timing for in vivo 1H-MR spectroscopic imaging of the human prostate at 3T. Magn Reson Med 2005;53(6):1268-1274.
11 Shukla-Dave A, Hricak H, Moskowitz C, Ishill N, Akin O, Kuroiwa K, Spector J, Kumar M, Reuter VE, Koutcher JA, Zakian KL. Detection of prostate cancer with MR spectroscopic imaging: an expanded paradigm incorporating polyamines. Radiology 2007;245(2):499-506.
12 Garcia-Martin ML, Adrados M, Ortega MP, Fernandez Gonzalez I, Lopez-Larrubia P, Viano J, Garcia-Segura JM. Quantitative (1) H MR spectroscopic imaging of the prostate gland using LCModel and a dedicated basis-set: correlation with histologic findings. Magn Reson Med; 65(2):329-339.
13 Heerschap A, Jager GJ, van der Graaf M, Barentsz JO, de la Rosette JJ, Oosterhof GO, Ruijter ET, Ruijs SH. In vivo proton MR spectroscopy reveals altered metabolite content in malignant prostate tissue. Anticancer research 1997; 17(3A): 1455-1460.
14 Jung JA, Coakley FV, Vigneron DB, Swanson MG, Qayyum A, Weinberg V, Jones KD, Carroll PR, Kurhanewicz J. Prostate depiction at endorectal MR spectroscopic imaging: investigation of a standardized evaluation system. Radiology 2004;233(3):701-708.
15 Futterer JJ, Scheenen TW, Heijmink SW, Huisman HJ, Hulsbergen-Van de Kaa CA, Witjes JA, Heerschap A, Barentsz JO. Standardized threshold approach using three-dimensional proton magnetic resonance spectroscopic imaging in prostate cancer localization of the entire prostate. Investigative radiology 2007;42(2):116-122.
16 Kobus T, Hambrock T, Hulsbergen-van de Kaa CA, Wright AJ, Barentsz JO, Heerschap A, Scheenen TW. In vivo assessment of prostate cancer aggressiveness using magnetic resonance spectroscopic imaging at 3 T with an endorectal coil. European urology;60(5):1074-1080.
17 Scheenen TWJ, Fütterer J, Weiland E and others. Discriminating cancer from noncancer tissue in the prostate by 3-dimensional proton magnetic resonance spectroscopic imaging: A prospective multicenter validation study. Invest Radiol 2011;46(1):25-33.
18 Scheenen TW, Heijmink SW, Roell SA, Hulsbergen-Van de Kaa CA, Knipscheer BC, Witjes JA, Barentsz JO, Heerschap A. Three-dimensional proton MR spectroscopy of human prostate at 3 T without endorectal coil: feasibility. Radiology 2007;245(2):507-516.
19 Kobus T, Wright AJ, Scheenen TW, Heerschap A. Mapping of prostate cancer by 1H MRSI. NMR Biomed. 2013 Jun 13. doi: 10.1002/nbm.2973. [Epub ahead of print] PMID:23761200.


Alan Wright


Arend Heerschap


Thiele Kobus


Tom Scheenen

Contact

Tom Scheenen, Ph.D.
Radboud University Nijmegen Medical Centre
Radiology Department

P.O. Box 9102
6500 HC Nijmegen
The Netherlands
Tom.Scheenen@radboudumc.nl

Case Series: 3T Prostate MRI With and Without the Use of an Endorectal Coil

Josephin Otto, M.D.; Harald Busse, Ph.D.

Department of Diagnostic and Interventional Radiology, Leipzig University Hospital, Leipzig, Germany

Introduction

Magnetic resonance imaging (MRI) has become a reliable technique for the detection, localization and local staging of prostate cancer [1]. Over the last decade, prostate MRI has clearly benefitted from advances in MRI hardware, most notably the introduction of 3 Tesla systems, and from the increased use of complementary functional imaging techniques in a multiparametric approach [2]. The use of endorectal coils will clearly improve the signal-to-noise ratio in the prostate, but the potential diagnostic gain is still open to debate [3]. Other factors that have to be considered are the extra time and effort needed, overall patient comfort, and reimbursement issues.

It is generally agreed that surface coils alone are sufficient for the detection and localization of significant prostate cancer [4], while local staging should ideally be performed with an endorectal coil or at a 3 Tesla system [5]. In an attempt to shed some light on that issue, the following three cases show axial, T2-weighted turbo spin-echo and diffusion-weighted images of the prostate at 3T (MAGNETOM Trio, A Tim System, Siemens Healthcare, Erlangen, Germany) that were acquired within the same patients, both with and without the use of an endorectal coil (eCoil, Medrad, Pittsburgh, PA, USA). Acquisition parameters were not adjusted between scans to facilitate comparison.

References

1 Dickinson L, Ahmed HU, Allen C, et al. Magnetic resonance imaging for the detection, localisation, and characterisation of prostate cancer: recommendations from a European consensus meeting. Eur Urol. 2011;59:477-94

2 Giannarini G, Zazzara M, Rossanese M, et al. Will Multi-Parametric Magnetic Resonance Imaging be the Future Tool to Detect Clinically Significant Prostate Cancer? Front Oncol. 2014;4:294

3 Somford DM, Hamoen EH, Fütterer JJ, et al. The predictive value of endorectal 3 Tesla multiparametric magnetic resonance imaging for extraprostatic extension in patients with low, intermediate and

Case 1

59-year-old patient with prostate-specific antigen (PSA) level of 13 ng/ml and Gleason score (GS) 7 (3+4) prostate cancer in the apex with a diameter of about 1 cm. T2-weighted images acquired with surface coils only (Figs. 1A–C), combining a 6-channel body matrix coil placed ventrally at the pelvic level and selected elements of a 24-channel spine matrix coil integrated into the MR table, and with the addition of an endorectal coil (Figs. 1D–F) show focal hypointense MRI signals at the level of the apex. Diffusion-weighted images acquired with a b-value of 800 s/mm^2 reveal hyperintense focal areas (Figs. 1B, E) with a corresponding reduction of the apparent diffusion coefficient (ADC) (Figs. 1C, F).

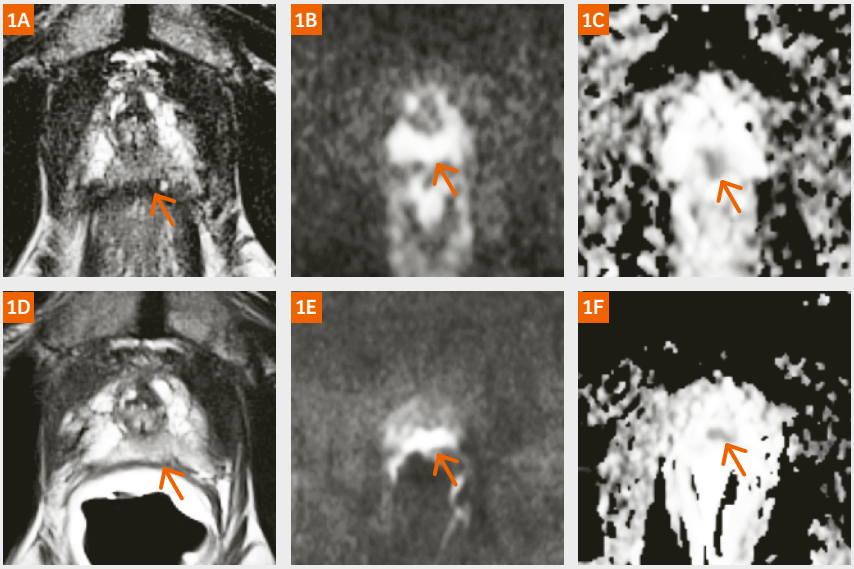

Figure 1: 3T prostate MRI (MAGNETOM Trio, A Tim System). Images were acquired with surface coils only **(1A–C)** and in combination with an endorectal coil **(1D–F)**. **(1A, D)** Axial, T2-weighted fast spin-echo sequences with repetition time TR 4,400 – 4,600 ms, echo time TE 126 ms and flip angle FA 120 – 135°. **(1B, E)** Axial diffusion-weighted imaging (DWI) was performed with a single-shot echo planar imaging sequence with TR 3,000 ms, TE 85 ms, FA 90° and b-values of 50, 500, 800 and 1,500 s/mm^2. **(1C, F)** ADC maps were calculated from DWI images at b-values 50, 500 and 800 s/mm^2.

Case 2

65-year-old patient with PSA level of 56 ng/ml and GS 7 (3+4) prostate cancer with a diameter larger than 1.5 cm, mainly located in the right peripheral zone. The whole-mount histopathological section analysis revealed stage pT3b disease.
The tumor is visible as a hypointense mass on T2-weighted images (Figs. 2A, D). The prostate capsule of the dorsolateral mid-gland shows an irregular bulging (Fig. 2D). Features on diffusion-weighted images (Figs. 2B, E) are less pronounced while ADC maps indicate a small corresponding region with restricted diffusion independent of the choice of imaging coils (Figs. 2C, F).

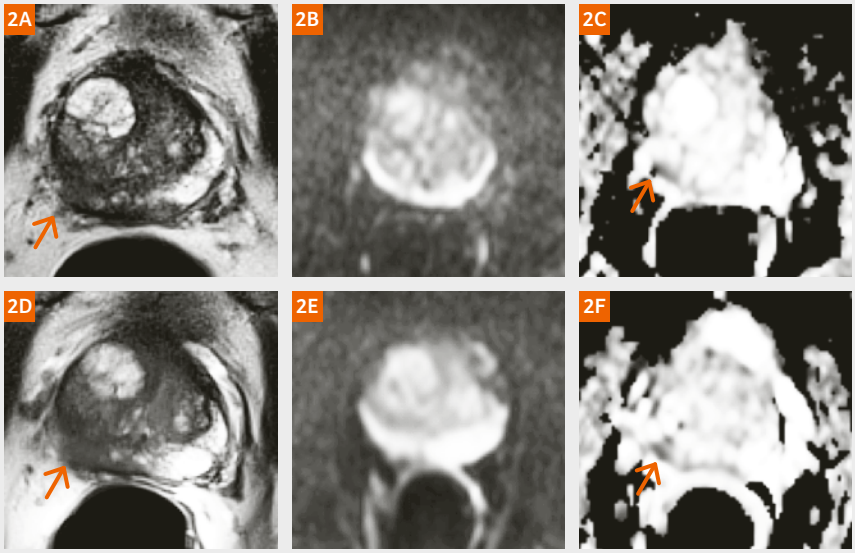

Figure 2: 3T prostate MRI using axial, T2-weighted fast spin-echo and diffusion-weighted imaging (see figure 1 for MR imaging parameters).

Case 3

71-year-old patient with PSA level of 8.2 ng/ml and GS 7 (3+4) prostate cancer in the left transitional zone, ventrolateral. The tumor is visible as an irregular hypointense mass on (Figs. 3A, D) T2-weighted images with (Figs. 3B, E) focal signal increase on DWI with b-value of 800 s/mm^2 and (Figs. 3C, F) corresponding low values on ADC maps. The prostate capsule shows an irregular bulging ventrolaterally and the length of the tumor contact is larger than 1 cm, suggesting extracapsular tumor growth, which was confirmed by histopathology (stage pT3a).

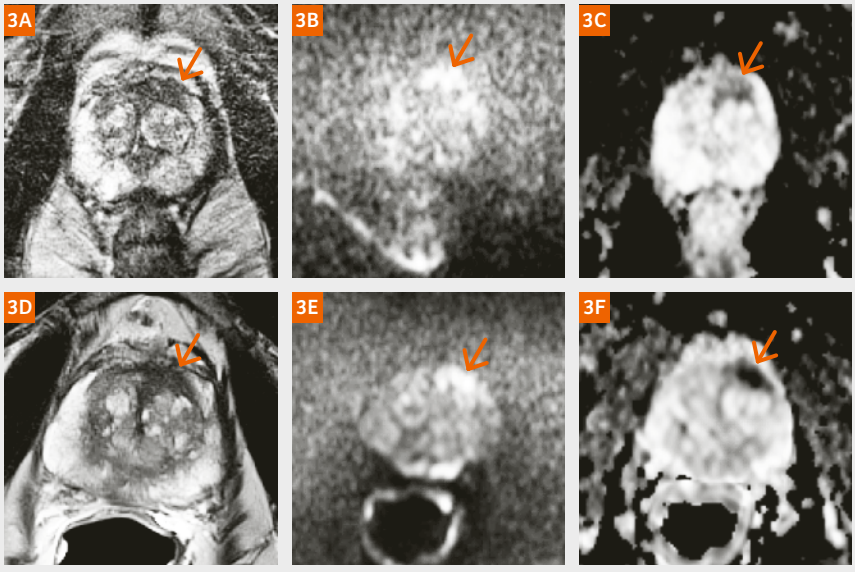

Figure 3: 3T prostate MRI using axial, T2-weighted fast spin-echo and diffusion-weighted imaging (see figure 1 for MRI parameters).

high risk prostate cancer. J Urol. 2013;190:1728-34
4 Abd-Alazeez M, Kirkham A, Ahmed HU, et al. Performance of multiparametric MRI in men at risk of prostate cancer before the first biopsy: a paired validating cohort study using template prostate mapping biopsies as the reference standard. Prostate Cancer Prostatic Dis. 2014;17:40-46.
5 Otto J, Thörmer G, Seiwerts M,et al. Value of endorectal magnetic resonance imaging at 3T for the local staging of prostate cancer. Rofo. 2014;186:795-802


Harald Busse


Josephin Otto

Contact

Josephin Otto, M.D.
Department of Diagnostic and Interventional Radiology
Leipzig University Hospital

Liebigstraße 20
04103 Leipzig
Germany
josephin.otto@medizin.uni-leipzig.de

The Role of Biomarkers in Prostate Cancer Management

Monet N. Sayegh, M.D., MS, BS, MT (ASCP) SH, CLS

Siemens Healthineers, Laboratory Diagnostics, Tarrytown, NY, USA

Since the introduction of serum prostate specific antigen (PSA) thirty years ago, prostate cancer diagnosis and management have been guided by this biomarker. Yet, PSA has proven controversial as a diagnostic assay due to its limitations.

PSA has persisted in clinical practice owing in large part to the public's demand for prostate cancer screening. Indeed, PSA remains an inexpensive and sensitive biomarker for disease detection, monitoring progression and recurrence following curative therapy of local disease. Furthermore, because PSA screening is so common, the clinical evaluation of new biomarkers has only occurred in patient populations previously screened for PSA. Thus, future iterations of prostate cancer biomarkers will most likely retain PSA as a primary clinical tool in conjunction with other tests, unless new biomarkers are shown to be superior to PSA in head-to-head comparisons. In this regard, new biomarker assays will likely complement PSA-based detection of prostate cancer [1, 2].

In 1986, the U.S. Food and Drug Administration (FDA) approved PSA as an adjunctive test to the digital rectal exam (DRE) for the detection of prostate cancer in men over the age of 50. In 1991, Catalona and colleagues demonstrated that the combination of a serum PSA measurement of more than ≥4.0 ng/mL with other clinical findings, such as the results of a DRE, improved detection of prostate cancer in a prospective study of 1653 healthy men with no history of cancer [3]. Numerous groups confirmed that PSA was useful as a diagnostic test for prostate cancer.

There have been numerous efforts to improve the performance of the PSA test, such as normalizing PSA to the size of the gland (the PSA 'density') [4–6] or monitoring the dynamics of PSA change in serum (the PSA velocity and doubling time) [7–11]. In addition, assays measuring alternative molecular traits of PSA have also gained attention, including free and complexed PSA (fPSA and cPSA, respectively) [12–15], and isoforms of the PSA protein (proPSA, most commonly). Among these, cPSA and fPSA have been considered adjunctive tests to total serum PSA rather than replacement assays (Fig. 1). cPSA measurements exploit the molecular interactions of PSA mainly with α-1-antichymotrypsin (ACT) in the blood [13]. Conversely,

1

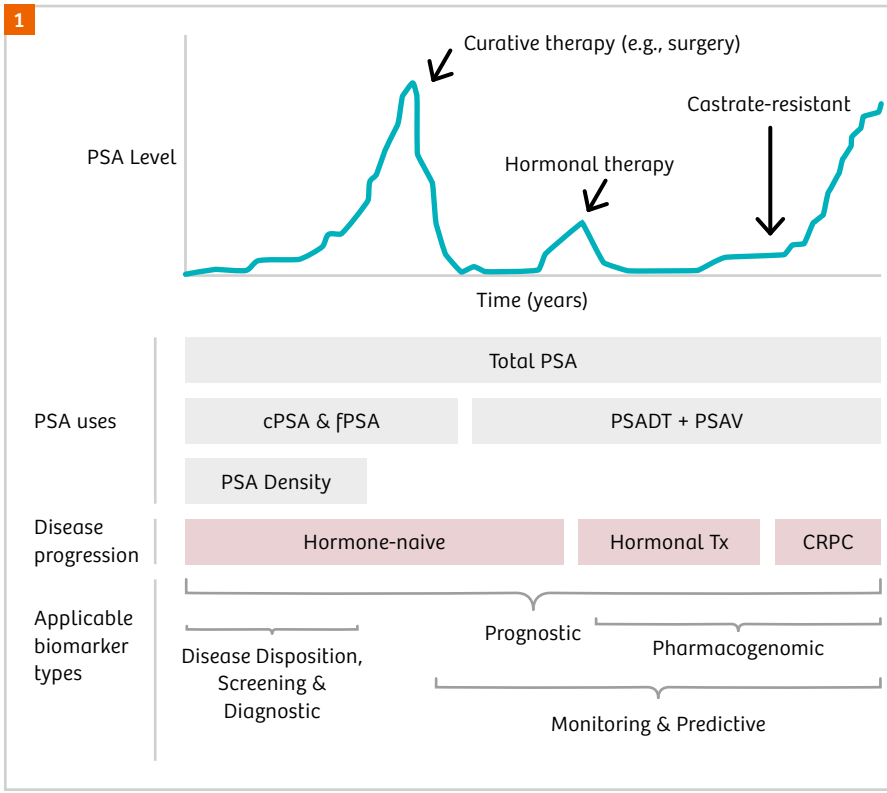

Figure 1: There have been numerous efforts to improve the performance of the PSA test.
Figure reproduced with permission from Sci Transl Med. 2012 Mar 28; 4(127): 127rv3.

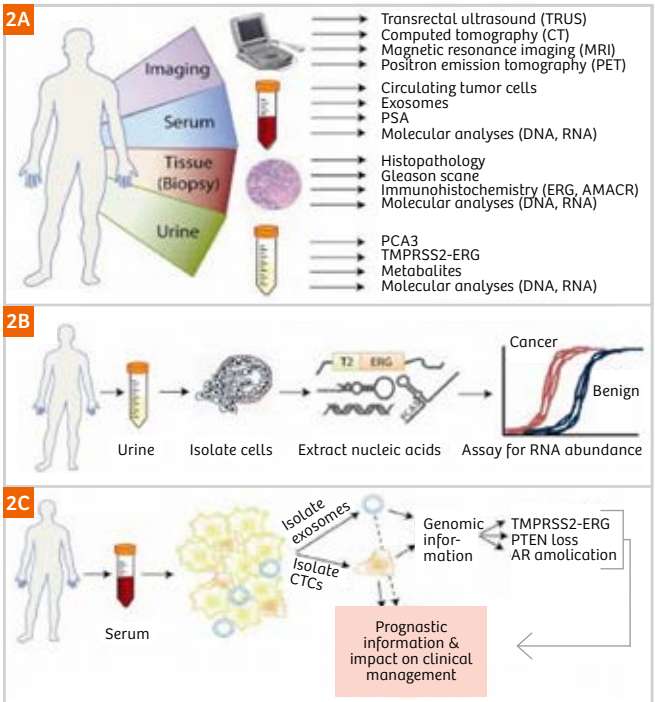

Figure 2: (2A) Biomarker research also includes advances in tissue and imaging-based tools. **(2B)** Promising future directions for biomarker research. **(2C)** One area of expanding investigation is circulating tumor cells.
Figure reproduced with permission from Sci Transl Med. 2012 Mar 28; 4(127): 127rv3.

fPSA measures the percentage of total serum PSA not bound to ACT. This %fPSA decreases in prostate cancer, making it useful in distinguishing men with benign prostatic hyperplasia (BPH) from men with cancer. A %fPSA of less than 25% has been shown to improve the sensitivity and specificity of a total PSA test and to reduce unnecessary biopsies [12, 15]. %fPSA has thus gained FDA approval for use when patients have a total PSA in the 4–10 ng/mL 'gray zone'. Furthermore, combined measurement of pro-PSA (a peptide precursor to mature PSA) with fPSA may help diagnose early prostate cancers with a PSA of 2 to 10 ng/mL [16, 17]. fPSA has several drawbacks, such as the potential instability of the fPSA measurement if sample processing occurs after 24 hours of collection [18]. The %fPSA may also increase following DRE or biopsy procedures [19], confounding its use in those settings.

PSA velocity (PSAV) and doubling time (PSADT) have prognostic value [20]. PSAV is defined as the change in PSA concentration per year, with a high PSAV being strongly associated with prostate cancer and a 9-fold elevated risk of cancer-death follows prostatectomy [7, 8, 21]. PSADT is defined as the time necessary for the serum PSA level to double. PSADT is most commonly used to monitor disease progression following curative therapy for organ-confined disease, as an increasing PSA level following radiotherapy or prostatectomy indicates the presence of residual tumor cells. Numerous studies have demonstrated that a more rapid PSADT (<10 months) is associated with reduced survival [9, 10]. In rare cases, disease may recur in the absence of an elevated PSA [22]. Nevertheless, neither test has been shown to improve over a standard PSA measurement for prostate cancer screening [11]. Taken together, measurement of PSA isoforms and dynamics have modestly improved care but are largely hindered by the same issues confounding PSA itself.

The 30 years since the widespread adoption of PSA have witnessed a remarkable maturation of genomic technologies, such as microarrays and whole-genome sequencing [23]. These advances in DNA sequence and RNA transcriptome profiling have enabled detailed dissections of cancer biology at a level previously unattainable [23, 24]. As a result, the world of biomarker research has shifted to use these '-omics' methods, populating the prostate cancer literature with discoveries based on profiling prostate tumors for aberrations in DNA, RNA, or epigenetic DNA methylation states. The discovery and characterization of emerging urine assays for prostate cancer, including prostate cancer antigen 3 (*PCA3*), the most prominent biomarker emerging as a non-PSA-based diagnostic test for prostate cancer. *PCA3* is a long noncoding RNA (lncRNA) that has been shown to be elevated in >90% of prostate cancer tissues, but not to normal or BPH tissues, an important distinction to serum PSA [25, 26] and the *TMPRSS2-ERG* gene fusion product arising from a translocation of the androgen-induced transmembrane protease, serine 2 (*TMPRSS2*) gene with the transcription factor v-ets erythroblastosis virus E26 oncogene homolog (*ERG*) is one of the most common genetic events in prostate cancer, present in approximately 50% of all cases and accounting for 90% of prostate cancer fusions [27]. *TMPRSS2-ERG* fusions are specific for prostate cancer, and can even be detected in precursor lesions, such as prostate intraepithelial neoplasia (PIN), if these lesions are proximal to, or contiguous with, regions of cancer [28] although the biomarker research also includes advances in tissue and imaging-based tools as well (Fig. 2A).

One area of expanding investigation is circulating tumor cells (CTCs). CTCs are found in the bloodstream and are particularly prevalent in locally aggressive or metastatic disease. CTCs can be both a biomarker for cancer detection and a source of molecular information, such as *TMPRSS2-ERG*, androgen receptor (AR) and phosphatase and tensin homolog (*PTEN*) copy number status (Fig. 2C) [32]. Similar effort has recently focused on developing assays to detect prostate-derived exosomes (also called prostatosomes). Exosomes are small vesicles (50–150 nm in diameter) generated from internalized parts of the cellular membrane that are subsequently secreted into the blood, semen, or urine (Fig. 2B, C) [33]. Prostate cancer patients exhibit increased numbers of exosomes in their serum compared to men with no disease, and elevated levels of exosomes may also correlate with increasing Gleason score (rates cases of prostate cancer on a scale of 2 to 10, with higher scores

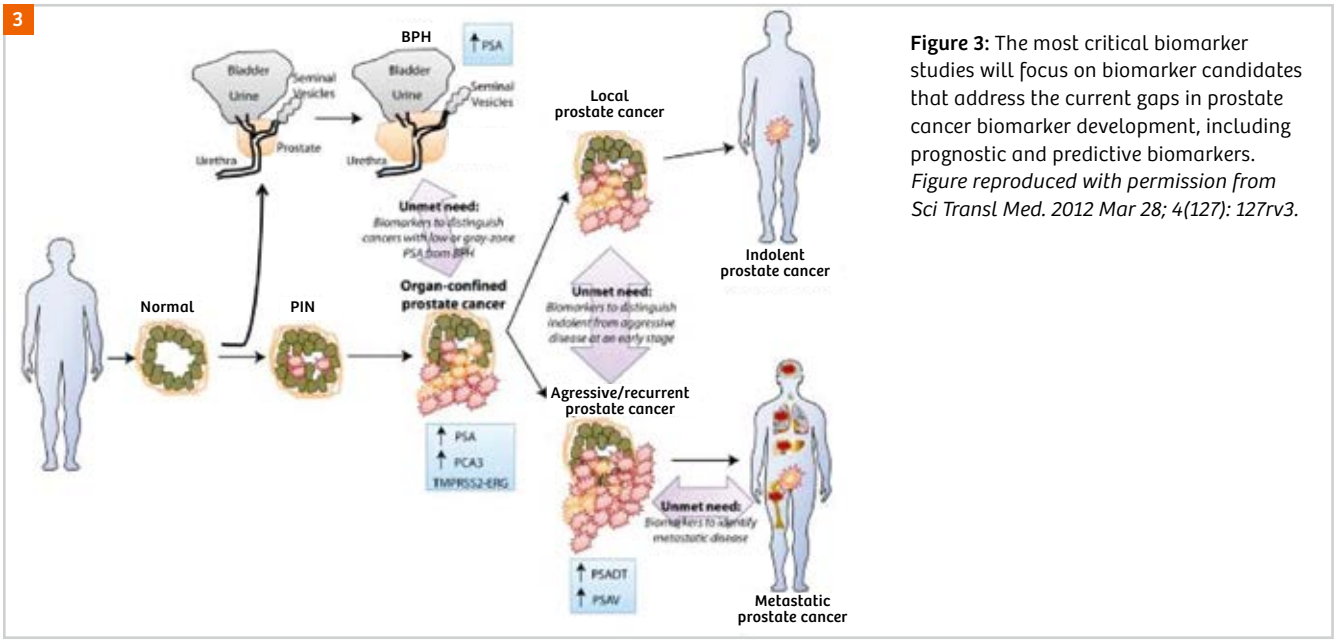

Figure 3: The most critical biomarker studies will focus on biomarker candidates that address the current gaps in prostate cancer biomarker development, including prognostic and predictive biomarkers. *Figure reproduced with permission from Sci Transl Med. 2012 Mar 28; 4(127): 127rv3.*

assigned to cancers that are growing more quickly and score of 7 indicates a moderate growth rate. While doctors are likely to watch and wait when a cancer has a low score of 2 to 6) [34]. Prostate cancer RNA biomarkers, including *PCA3* and *TMPRSS2-ERG*, can also be detected in urine-derived exosomes from prostate cancer patients [35]. Although these efforts remain mainly research-oriented at this time, they provide promising future directions for biomarker research (Fig. 2B).

The most critical biomarker studies will focus on biomarker candidates that address the current gaps in prostate cancer biomarker development, including prognostic and predictive biomarkers (Fig. 3). The utility of PSA as a diagnostic biomarker for prostate cancer is limited by the fact that only about 3% of PSA-screened men with prostate cancer have lethal disease, thus leading to overtreatment of indolent disease [29]. Development of new biomarkers that only identify more prostate cancer cases does not address this discrepancy. It follows, then, that the identification and validation of novel biomarkers to 'rule out' lethal prostate cancer at the point of screening is the greatest unmet clinical need, as this may reduce unnecessary interventions that may cause more harm than good.

A common theme in prostate cancer biomarker development is the desirability of non-invasive assays to replace biopsy as the diagnostic gold standard. Biopsy procedures are associated with increased risk of adverse events, such as bleeding and sepsis, owing to their invasive nature. Studies have routinely shown that biopsies are associated with a 23–25% false negative rate, perhaps owing to inefficient sampling, where normal tissue is biopsied in addition to diseased tissue. Non-invasive bio-markers in serum and urine have the potential to improve the standard tissue biopsy procedure, although they cannot provide direct histopathological or spatiotemporal information. As such, supplementing PSA measurements with urine biomarker analyses may become standard practice in the near future [30, 31].

Finally, these developments also need to be considered in conjunction with tissue biomarkers and imaging technologies, such as transrectal ultrasound (TRUS), computed tomography (CT), magnetic resonance imaging (MRI), and positron emission tomography (PET). Indeed, the role of imaging is crucial to patient management for visualizing and staging both localized prostate cancers and metastatic disease, especially in the bone.

References

1 American Cancer Society. Cancer Facts & Figures 2013. Atlanta: American Cancer Society; 2013. Available at: http://www.cancer.org/docroot/STT/stt_0.asp. Accessed May 8, 2013.
2 Cary KC,Cooperberg MR. Biomarkers in prostate cancer surveillance and screening: past, present and future. The Adv Urol. 2013; 5:318-329.
3 Catalona WJ, Smith DS, Ratliff TL, Dodds KM, Coplen DE, Yuan JJ, Petros JA, Andriole GL. Measurement of prostate-specific antigen in serum as a screening test for prostate cancer. N Engl J Med. 1991;324:1156–1161.
4 Stamey TA, Yang N, Hay AR, McNeal JE, Freiha FS, Redwine E. Prostate-specific antigen as a serum marker for adenocarcinoma of the prostate. N Engl J Med. 1987;317:909–916.
5 Carter HB, Sauvageot J, Walsh PC, Epstein JI. Prospective evaluation of men with stage T1C adenocarcinoma of the prostate. J Urol. 1997;157:2206–2209
6 Kundu SD, Roehl KA, Yu X, Antenor JA, Suarez BK, Catalona WJ. Prostate specific antigen density correlates with features of prostate cancer aggressiveness. J Urol. 2007;177:505–509.
4 Partin AW, Criley SR, Subong EN, et al. Standard versus age-specific prostate specific antigen reference ranges among men with clinically localized prostate cancer: a pathological analysis. J Urol.1996;155:1336-1339.
5 National Comprehensive Cancer Network. NCCN Clinical Practice Guidelines in Oncology (NCCN Guidelines™). Prostate cancer early

detection, v.2.2012. Available athttp://www.nccn.org/professionals/physician_gls/f_guidelines.asp. Accessed May 8, 2013.
6 Carter HB, Albertsen PC, Barry MJ, et al. Early detection of prostate cancer: AUA guideline.http://www.auanet.org/common/pdf/education/clinical-guidance/Prostate-Cancer-Detection.pdf April 2013. Accessed May 8, 2013.
7 Carter HB, Ferrucci L, Kettermann A, Landis P, Wright EJ, Epstein JI, Trock BJ, Metter EJ. Detection of life-threatening prostate cancer with prostate-specific antigen velocity during a window of curability. J Natl Cancer Inst. 2006;98:1521–1527.
8 D'Amico AV, Chen MH, Roehl KA, Catalona WJ. Preoperative PSA velocity and the risk of death from prostate cancer after radical prostatectomy. N Engl J Med. 2004;351:125–135.
9 Makarov DV, Humphreys EB, Mangold LA, Carducci MA, Partin AW, Eisenberger MA, Walsh PC, Trock BJ. The natural history of men treated with deferred androgen deprivation therapy in whom metastatic prostate cancer developed following radical prostatectomy. J Urol. 2008;179:156–161.
10 Pound CR, Partin AW, Eisenberger MA, Chan DW, Pearson JD, Walsh PC. Natural history of progression after PSA elevation following radical prostatectomy. JAMA. 1999;281:1591–1597.
11 Ulmert D, Serio AM, et.al Long-term prediction of prostate cancer: prostate-specific antigen (PSA) velocity is predictive but does not improve the predictive accuracy of a single PSA measurement 15 years or more before cancer diagnosis in a large, representative, unscreened population. J Clin Oncol. 2008;26:835–841
12 Catalona WJ, Partin AW, Slawin KM, Brawer MK, Flanigan RC, Patel A, Richie JP, deKernion JB, Walsh PC, Scardino PT, Lange PH, Subong EN, Parson RE, Gasior GH, Loveland KG, Southwick PC. Use of the percentage of free prostate-specific antigen to enhance differentiation of prostate cancer from benign prostatic disease: a prospective multicenter clinical trial. JAMA. 1998;279:1542–1547.
13 Lilja H, Christensson A, Dahlen U, Matikainen MT, Nilsson O, Pettersson K, Lovgren T. Prostate-specific antigen in serum occurs predominantly in complex with alpha 1-antichymotrypsin. Clin Chem. 1991;37:1618–1625.
14 Partin AW, Brawer MK, Bartsch G, Horninger W, Taneja SS, Lepor H, Babaian R, Childs SJ, Stamey T, Fritsche HA, Sokoll L, Chan DW, Thiel RP, Cheli CD. Complexed prostate specific antigen improves specificity for prostate cancer detection: results of a prospective multicenter clinical trial. J Urol. 2003;170:1787–1791.
15 Prestigiacomo AF, Lilja H, Pettersson K, Wolfert RL, Stamey TA. A comparison of the free fraction of serum prostate specific antigen in men with benign and cancerous prostates: the best case scenario. J Urol. 1996;156:350–354.
16 Catalona WJ, Bartsch G, Rittenhouse HG, Evans CL, Linton HJ, Horninger W, Klocker H, Mikolajczyk SD. Serum pro-prostate specific antigen preferentially detects aggressive prostate cancers in men with 2 to 4 ng/ml prostate specific antigen. J Urol. 2004;171:2239–2244.
17 Sokoll LJ, Chan DW, Mikolajczyk SD, Rittenhouse HG, Evans CL, Linton HJ, Mangold LA, Mohr P, Bartsch G, Klocker H, Horninger W, Partin AW. Proenzyme psa for the early detection of prostate cancer in the 2.5–4.0 ng/ml total psa range: preliminary analysis. Urology. 2003;61:274–276.
18 Piironen T, Pettersson K, Suonpaa M, Stenman UH, Oesterling JE, Lovgren T, Lilja H. In vitro stability of free prostate-specific antigen (PSA) and prostate-specific antigen (PSA) complexed to alpha 1-antichymotrypsin in blood samples. Urology. 1996;48:81–87.
19 Ornstein DK, Rao GS, Smith DS, Ratliff TL, Basler JW, Catalona WJ. Effect of digital rectal examination and needle biopsy on serum total and percentage of free prostate specific antigen levels. J Urol. 1997;157:195–198.
20 Heidenreich A, Aus G, Bolla M, Joniau S, Matveev VB, Schmid HP, Zattoni F. EAU guidelines on prostate cancer. Eur Urol. 2008; 53:68–80.
21 Carter HB, Morrell CH, Pearson JD, Brant LJ, Plato CC, Metter EJ, Chan DW, Fozard JL, Walsh PC. Estimation of prostatic growth using serial prostate-specific antigen measurements in men with and without prostate disease. Cancer Res. 1992;52:3323–3328.
22 Leibovici D, Spiess PE, Agarwal PK, Tu SM, Pettaway CA, Hitzhusen K, Millikan RE, Pisters LL. Prostate cancer progression in the presence of undetectable or low serum prostate-specific antigen level. Cancer. 2007;109:198–204.
23 Berger MF, Lawrence MS,,et.al. The genomic complexity of primary human prostate cancer. Nature. 2011;470:214–220.
24 Prensner JR, Iyer MK, et.al. Transcriptome sequencing across a prostate cancer cohort identifies PCAT-1, an unannotated lincRNA implicated in disease progression. Nat Biotechnol. 2011;29:742–749.
25 Bussemakers MJ, van Bokhoven A, Verhaegh GW, Smit FP, Karthaus HF, Schalken JA, Debruyne FM, Ru N, Isaacs WB. DD3: a new prostate-specific gene, highly overexpressed in prostate cancer. Cancer Res. 1999;59:5975–5979.
26 de Kok JB, Verhaegh GW, Roelofs RW, Hessels D, Kiemeney LA, Aalders TW, Swinkels DW, Schalken JA. DD3(PCA3), a very sensitive and specific marker to detect prostate tumors. Cancer Res. 2002;62:2695–2698.
27 Prensner JR, Chinnaiyan AM. Oncogenic gene fusions in epithelial carcinomas. Curr Opin Genet Dev. 2009;19:82–91.
28 Han B, Mehra R, Lonigro RJ, Wang L, Suleman K, Menon A, Palanisamy N, Tomlins SA, Chinnaiyan AM, Shah RB. Fluorescence in situ hybridization study shows association of PTEN deletion with ERG rearrangement during prostate cancer progression. Mod Pathol. 2009;22:1083–1093.
29 Etzioni R, Cha R, Feuer EJ, Davidov O. Asymptomatic incidence and duration of prostate cancer. Am J Epidemiol. 1998;148:775–785.
30 Daneshgari F, et.al. Computer simulation of the probability of detecting low volume carcinoma of the prostate with six random systematic core biopsies.Urology.1995;45:604-609
31 Rabbani F, et.al. Incidence and clinical significance of false-negative sextant prostate biopsies. J Urol. 1998;159: 1247-1250.
32 Attard G, Swennenhuis JF, et.al. Characterization of ERG, AR and PTEN gene status in circulating tumor cells from patients with castration-resistant prostate cancer. Cancer Res. 2009;69:2912–2918.
33 Duijvesz D, Luider T, Bangma CH, Jenster G. Exosomes as biomarker treasure chests for prostate cancer. Eur Urol. 2011;59:823–831.
34 Tavoosidana G, Ronquist G, et.al. Multiple recognition assay reveals prostasomes as promising plasma biomarkers for prostate cancer. Proc Natl Acad Sci U S A. 2011;108:8809–8814.
35 Nilsson J, Skog J, Nordstrand A, Baranov V, Mincheva-Nilsson L, Breakefield XO, Widmark A. Prostate cancer-derived urine exosomes: a novel approach to biomarkers for prostate cancer. Br J Cancer. 2009;100:1603–1607

Contact

Monet N. Sayegh, M.D.
Senior Medical/Clinical Consultant
Disease Management Education
Clinical & Scientific Affairs

5210 Pacific Concourse Drive
Los Angeles, CA 90045-6900
USA
Phone: +1 805-584-8750
Fax: +1 805-584-8750
mona.sayegh@siemens-healthineers.com

Experiences with Robot Assisted MR-guided Inbore Prostate Biopsies

Jeroen Reijnen; Jon Bache Marthinsen

Radiology Department, Sørlandet Hospital Kristiansand, Kristiansand, Norway

Background

Clinical management of prostate cancer is strongly challenged by the triangle of very high prevalence [1], heterogeneous and poorly understood tumor biology, and significant side effects of established treatments [2]. In order to contain the harms of therapy, we have to put great effort into the difficult task of identifying, from a huge pool of indolent prostate cancers, the patients that actually benefit from treatment.

In recent years, multiparametric MR imaging of the prostate (mpMRI) has evolved into a useful tool in the pursuit of better prognostic stratification. On the one hand, quality assured mpMRI has great potential for triage of patients for biopsies [3], i.e. omitting unnecessary biopsies [4]. On the other hand, mpMRI targeted biopsies, instead of or in addition to systematic biopsies, escalate the detection rate of cancer that might need treatment [5] and increase the likelihood and confidence of attaining optimally representative biopsies, i.e. sampling tumor tissue that can be expected to drive prognosis.

Diagnostic pathway

In the assessment for possible prostate cancer at our prostate center, mpMRI is the first test for all patients. For interpretation of the mpMRI we apply PI-RADS v2, but in some cases deviate from the scoring guidelines. Based on recent literature [4] and internal results (Table 1), our group refrains from biopsy in most patients with a negative mpMRI (PI-RADS 1–2). Systematic biopsies despite negative mpMRI are performed in selected patients on the basis of certain clinical alarm signals, since it is clear that prostate cancers can have growth patterns that make them more or less MR-invisible. Patients with a positive mpMRI (PI-RADS 3–5) are scheduled for either MR-guided inbore biopsy or TRUS-biopsy, the preferred method depending on the targets defined on the mpMRI, in the following manner: Lesions considered potentially deterministic for prognosis and treatment choice are defined as biopsy targets, with a maximum of three targets for practical reasons. In case of heterogeneous intratumoral signal characteristics on diffusion-weighted images (DWI) or dynamic contrast-enhanced images (DCE), the area that is suspected to correlate to highest tumor aggressiveness is defined as a separate biopsy target. Only in the case of a high probability of hitting all the defined targets is TRUS-biopsies considered the preferred method. At our institute this currently generates approximately 6 MR-guided biopsies weekly.

	PI-RADS 1+2	PI-RADS 3	PI-RADS 4+5
Group size	**43%**	**8%**	**49%**
% cancer	**1%**	**27%**	**91%**
Gleason score 6	1%	20%	33%
Gleason score 7a	0	7%	30%
Gleason score 7b or higher	0	0	28%

Table 1: Performance of diagnostic mpMRI at our institute. Retrospective data collected for quality assurance purposes (189 patients). Numbers represent highest Gleason score found during completed diagnostic workup or in prostatectomy specimens.

System and workflow

For the MR-guided biopsies we use a MAGNETOM Skyra 3T system and Soteria's Remote Controlled Manipulator (RCM)[1], a pneumatically driven robotic device that allows for precise needle guide steering from the operator room (Fig. 1).

Oral antibiotic prophylaxis and an enema are the only preparations for the biopsy procedure. For the procedure the patient is placed in the prone position on the MR table and a needle guide is inserted in the rectum and subsequently connected to the RCM (Fig. 2). Image guidance is done with TrueFISP, alternatively short T2w TSE, sequences and when deemed beneficial, diffusion-weighted imaging (Case 3). Images are send from the MR console to the RCM software, which then allows for quick and easy calibration and thereafter manipulation of the needle guide position (Fig. 3). When the images show satisfactory needle guide positioning, a biopsy needle is inserted into the needle guide at appropriate depth and the biopsy taken.

[1] The information shown herein refers to products of 3rd party manufacturers (Soteria) and thus are in their regulatory responsibility. Please contact Soteria for further information.

Figure 1: The RCM-system. **(1A)** MRI-compatible robotic device that holds and manipulates the position of the needle guide. **(1B)** Cart that is positioned outside of the MRI-room and connected to the robotic device by plastic tubing, containing a steering unit, compressor and vacuum pump. The system includes a portable laptop with the control and targeting software.

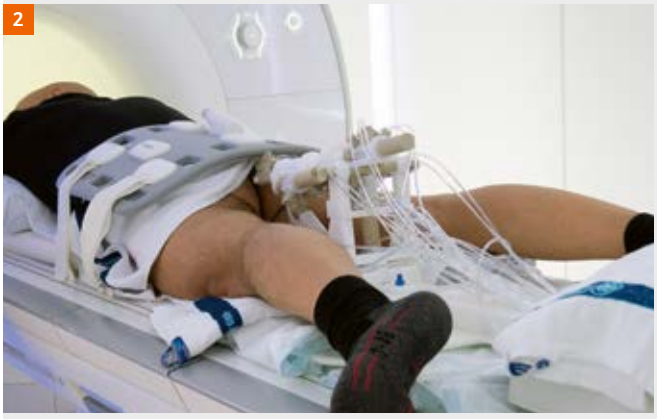

Figure 2: Patient and RCM positioning.

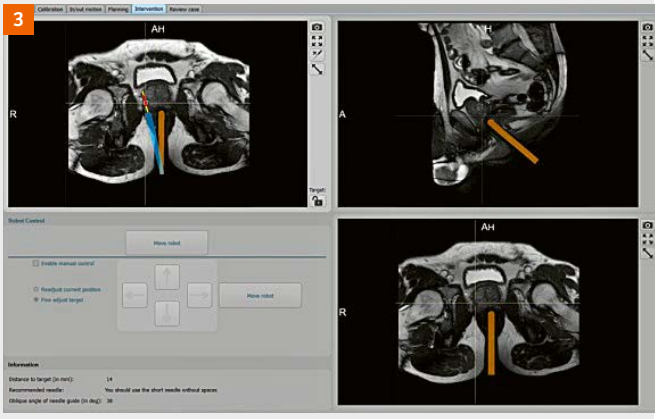

Figure 3: Software interface.

Usage of an MR-compatible biopsy needle permits for image documentation of the needle position. However, in our experience the procedure allows for such accurate needle positioning that this step is superfluous in most cases. By routinely using ordinary biopsy needles we save both time and money.

Procedure time varies with lesion size, location and especially number. In the majority of our cases a door-to-door time of 30 minutes is achieved, but since somewhat longer procedures do occur quite regularly, we currently schedule 40 minutes per patients.

Experiences

Patients generally tolerate the procedure very well. The prone position can become somewhat uncomfortable for the shoulders, but due to predominantly short procedure times this rarely creates significant problems.

Learning to use the RCM system has been quite easy and right from the start we have been able to perform accurate biopsies. Obtaining short procedure times required some experience for both radiologists and technologists, but was achieved rather quickly.

All our targets have been reachable with the system. Biopsy precision is logically dependent on the operator's ability to correctly identify the target and readiness to aim accurately, but the RCM enables the operator to achieve a very high level of precision. In our experience, even the smallest of targets, in all locations in the prostate, are consistently hit (e.g. Case 1).

In approximately 85% of our biopsy cases cancer is found. In the benign cases the mpMRI findings are usually equivocal and the confident needle positioning routinely allows for considering the benign histology to be representative.

In addition to high detection rates, we experience three further important advantages of the high accuracy. First, targeting of more than one lesion and precise targeting of the tumor center or intratumoral areas suspicious of higher-grade cancer regularly generates higher final Gleason scores (Case 2). Second, the technique clarifies mpMRI findings, which increases to total accuracy of the diagnostics. Third, concise learning feedback to the diagnostic imaging is generated, which is highly valuable given the evolving pivotal role of mpMRI in clinical management of probable prostate cancer.

Conclusions

The RCM facilitates targeted MR-guided biopsies of the prostate with very high precision and confidence in a time-efficient manner. Providing high-quality diagnostic mpMRI,

Case 1

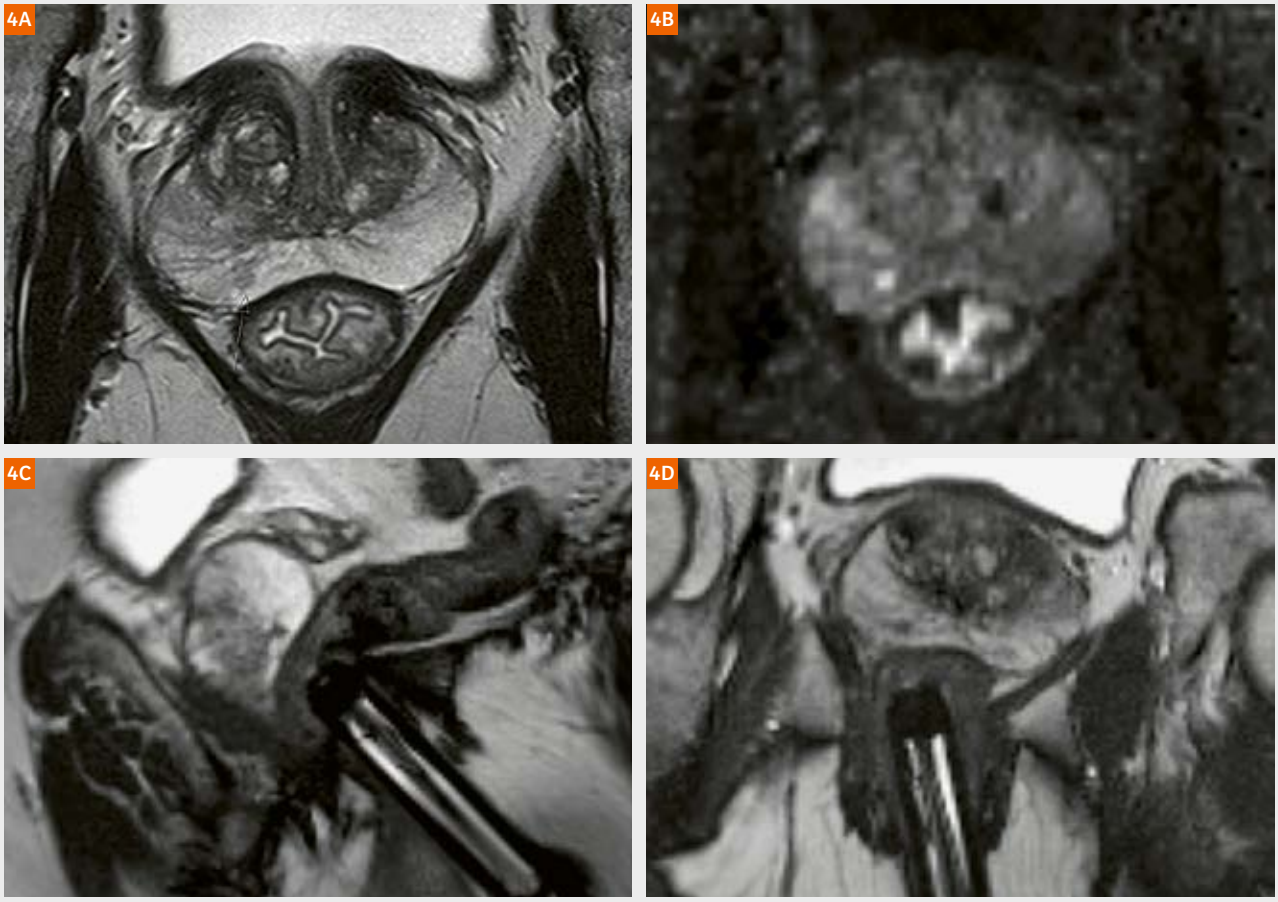

Figure 4: 65-year-old patient with PSA level 4.4.

Diagnostic mpMRI showed a 3 mm highly tumor suspicious lesion in the peripheral zone of the right midgland and additionally typical prostatitis changes anterolaterally mainly on the right side.

MR-guided biopsies revealed prostate cancer Gleason grade 4+3.

4A) Diagnostic mpMRI, transversal TSE T2w.
4B) Diagnostic mpMRI, transversal calculated b1500 images (RESOLVE diffusion).
4C) TrueFISP sagitally along the axis of the biopsy needle guide pointing at the target.
4D) TrueFISP transversally along the axis of the biopsy needle guide pointing at the target.

this allows for routine application of a one-stop, definitive biopsy strategy that aims at accurately mapping prostate cancer. Our center performs RCM-biopsies whenever they are expected to outperform TRUS-biopsies in the challenging task of detecting and delineating the clinical significance of prostate cancer, i.e. in the majority of our patients. With this, the system has revolutionized our practice and empowered us to improve and further develop stratification of our patients. A hope for the future is that improvements in histological grading and molecular testing of tumor tissue [6, 7], combined with optimized biopsies, will lead to further improvements in prognostication.

References

1 Bell, Katy J. L., Del Mar, Chris, Wright, Gordon, Dickinson, James & Glasziou, Paul. 2015. Prevalence of incidental prostate cancer: A systematic review of autopsy studies. International Journal of Cancer. Journal International du Cancer 137: 1749-1757.
2 Resnick, Matthew J., Koyama, Tatsuki, Fan, Kang-Hsien, Albertsen, Peter C., Goodman, Michael, Hamilton, Ann S., Hoffman, Richard M.,

Case 2

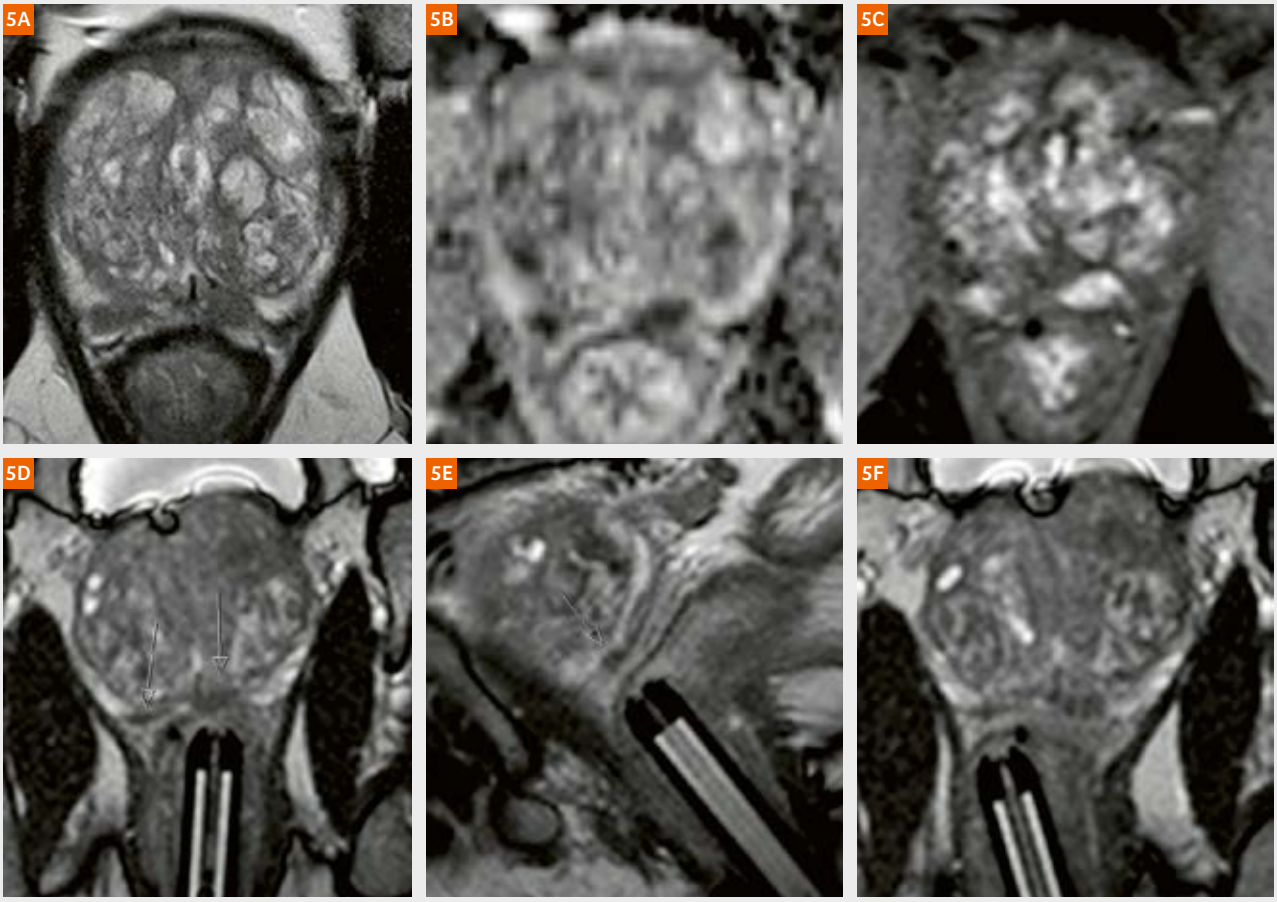

Figure 5: 63-year-old patient with PSA level 6.0, referred to our center for MR-guided biopsies after negative MR-US Fusion-guided biopsies at an external institute.

Diagnostic mpMRI showed a large prostate (estimated volume 128 ml) and apically bilateral relatively small, but highly tumor suspicious lesions.

Both lesions were targeted with MR-guided biopsies. Histology revealed prostate cancer Gleason grade 4+3 on the left side and Gleason grade 4+5 on the right side.

5A) Diagnostic mpMRI, transversal TSE T2w.
5B) Diagnostic mpMRI, transversal ADC map (RESOLVE diffusion).
5C) Diagnostic mpMRI, initial contrast uptake phase of transversal DCE (Twist VIBE).
5D) TrueFISP transversally along the axis of biopsy needle guide pointing at the target on the left side.
5E) TrueFISP sagittaly along the axis of the biopsy needle guide pointing at the target on the right side.
5F) TrueFISP transversally along the axis of the biopsy needle guide pointing at the target on the right side.

Potosky, Arnold L., Stanford, Janet L., Stroup, Antoinette M., Van Horn, R. Lawrence & Penson, David F.. 2013. Long-Term Functional Outcomes after Treatment for Localized Prostate Cancer. The New England journal of medicine 368: 436-445.

3 de Rooij, M., Hamoen, E. H., Futterer, J. J., Barentsz, J. O. & Rovers, M. M.. 2014. Accuracy of multiparametric MRI for prostate cancer detection: a meta-analysis. AJR Am J Roentgenol 202: 343-51.

4 Ahmed HU. The PROMIS study: a paired-cohort, blinded confirmatory study evaluating the accuracy of multi-parametric MRI and TRUS biopsy in men with an elevated PSA. J Clin Oncol 2016; 34: (suppl; abstr 5000).

5 Pokorny, M. R., de Rooij, M., Duncan, E., Schroder, F. H., Parkinson, R., Barentsz, J. O. & Thompson, L. C.. 2014. Prospective study of diagnostic accuracy comparing prostate cancer detection by transrectal ultrasound-guided biopsy versus magnetic resonance (MR) imaging with subsequent MR-guided biopsy in men without previous prostate biopsies. Eur Urol 66: 22-29.

6 McKenney, Jesse K., Wei, Wei, Hawley, Sarah, Auman, Heidi, Newcomb, Lisa F., Boyer, Hilary D., Fazli, Ladan, Simko, Jeff MD, Hurtado-Coll, Antonio, Troyer, Dean A., Tretiakova, Maria S., Vakar-Lopez, Funda, Carroll, Peter R., Cooperberg, Matthew R., Gleave, Martin E., Lance, Raymond S., Lin, Dan W., Nelson, Peter S.,

Case 3

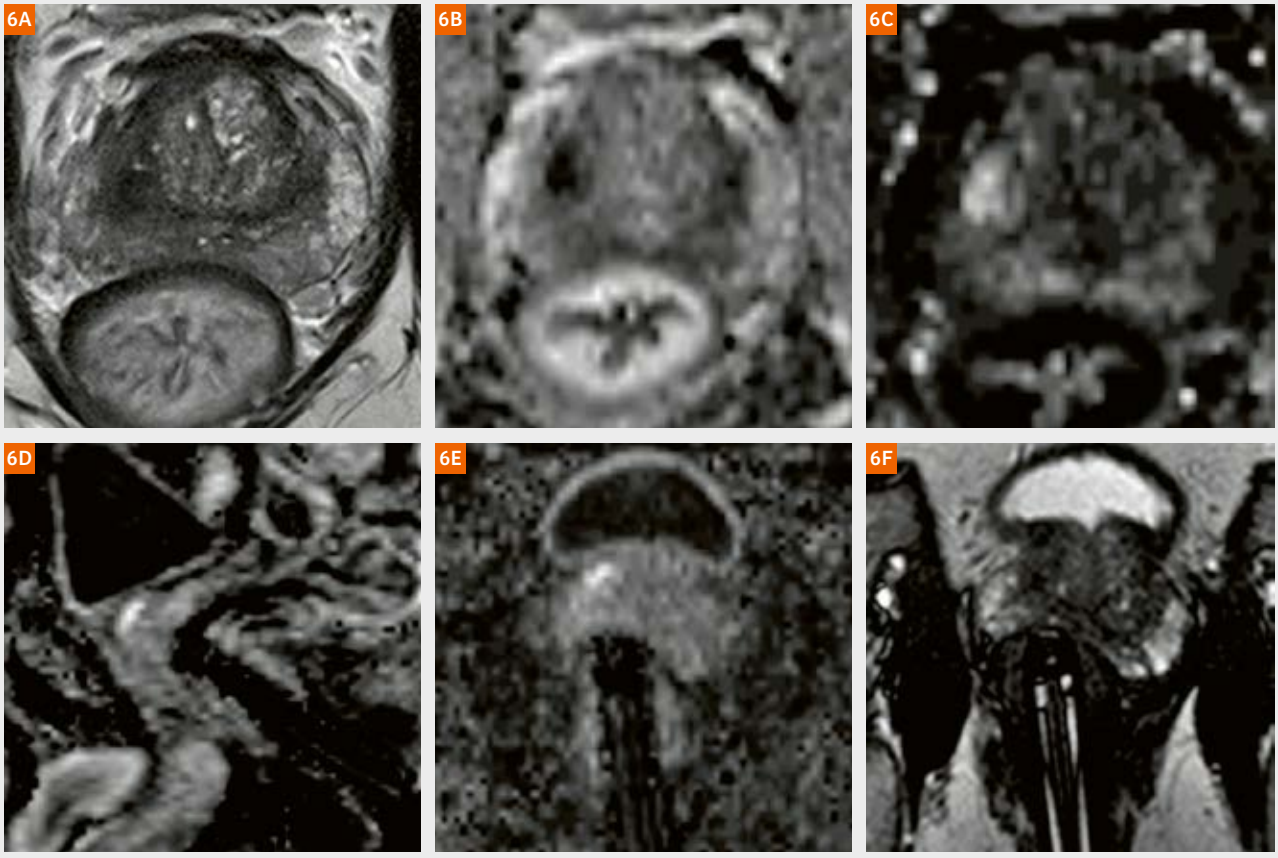

Figure 6: 63-year-old patient with PSA level 5.3.

Diagnostic mpMRI showed an 8 mm tumor suspicious lesion in the transitional zone of the right basal gland.

During the MR-guided biopsy procedure the lesion was hard to localize on TrueFISP and TSE T2 images, but possible to target confidently with the use of diffusion-weighted images.

Histology revealed prostate cancer Gleason grade 3+4.

6A) Diagnostic mpMRI, transversal TSE T2w.
6B) Diagnostic mpMRI, transversal ADC map (RESOLVE diffusion).
6C) Diagnostic mpMRI, transversal calculated b3000 images (RESOLVE diffusion).
6D) Calculated b1500 images (RESOLVE diffusion) sagittaly along the axis of the biopsy needle guide pointing at the target.
6E) Calculated b1500 images (RESOLVE diffusion) transversally along the axis of the biopsy needle guide pointing at the target.
6F) TrueFISP transversally along the axis of the biopsy needle guide pointing at the target.

Thompson, Ian M., True, Lawrence D., Feng, Ziding, Brooks, James D. 2016. Histologic Grading of Prostatic Adenocarcinoma Can Be Further Optimized: Analysis of the Relative Prognostic Strength of Individual Architectural Patterns in 1275 Patients From the Canary Retrospective Cohort. Am J Surg Pathol 2016 Nov;40(11):1439-1456.

7 Hoogland, A. Marije, Kweldam, Charlotte F. and Van Leenders, Geert J. L. H.. Prognostic Histopathological and Molecular Markers on Prostate Cancer Needle-Biopsies: A Review. BioMed Research International, vol. 2014, Article ID 341324.

Contact

Jeroen Reijnen
Radiology Department
Sørlandet Hospital Kristiansand

Egsveien 1000
Postboks 416
4604 Kristiansand
Norway
Phone: +47 97799733
Jeroen.Sebastiaan.Reijnen@sshf.no

Jon Bache Marthinsen, Jeroen Reijnen, Frank Gonzalez

MR-Guided Biopsies of the Prostate in Supine Patient Position

Florian Schneider, M.D.[1]; Martin Requardt, Ph.D.[2]; Gregor Thörmer, Ph.D.[2]; Karl Engelhard, M.D.

[1] Diagnostic Radiology, Martha-Maria Hospital Nürnberg, Germany
[2] Siemens Healthcare, Magnetic Resonance, Erlangen, Germany

Introduction

Prompted by elevated PSA levels, more than a million men in the United States alone have to undergo transrectal ultrasound (TRUS)-guided prostate biopsy to clarify suspicion for prostate cancer per year [1]. Unlike pathways for other malignancies, biopsy of the prostate is performed by standardized, systematic but essentially random sampling [2]. The major limitation of this approach is that clinically insignificant cancers are often identified by chance while, even more important, clinically significant cancers may remain undetected [3, 4]. As a result of this uncertainty, more than one-third of men whose first biopsy was negative are rebiopsied within 5 years [1]. Over recent years, multiparametric magnetic resonance imaging (mpMRI), combining the morphological assessment of T2-weighted (T2w) imaging with different functional imaging techniques such as diffusion-weighted imaging (DWI) and dynamic contrast enhanced imaging (DCE) has become a mature tool for localizing and visualizing suspicious foci in the prostate.

Consequently, advances are being made in the way that biopsies are performed, with the aim to integrate the additional information into the biopsy workflow: Cognitive registration, in-bore MR guided biopsy and MR/US fusion biopsies are the most commonly used techniques to improve prostate cancer detection with targeted biopsy. While both cognitive integration and MR/US fusion biopsies have been shown to improve the cancer detection rate [5], prostate biopsies performed under direct MR guidance are indicated in patients where MR imaging identified lesions that are either very small or located in areas difficult to reach with standard TRUS-guided biopsy. Another indication might be in patients showing a clear discrepancy between the histopathological findings of TRUS-biopsy and imaging results.

In the following, we report on our clinical experience with a customized approach and a simplified biopsy workflow for MR-guided prostate biopsies where the patient lies in supine position.

Case 1

Due to a contraindication for digital rectal examination and transrectal ultrasound because of rectal stenosis, a 72-year-old, biopsy-naive patient with continuously rising PSA levels (last: 12 ng/ml) was referred to our institution for diagnostic prostate MRI. Scans were performed with high-channel surface coils only using a MAGNETOM Skyra 3T system.

The protocol consisted of axial, coronal and sagittal T2-weighed TSE scans (TR 8300 ms, TE 107 ms, slice thickness 3.0 mm, FOV 160 mm, matrix 320, TA 3:11 min); axial diffusion-weighted imaging with RESOLVE (TR 4190 ms, TE 69 ms, slice thickness 3.0 mm, FOV 160 mm, matrix 114, TA 4:42 min) and axial DCE scans (TR 5.08 ms, TE 1.77 ms, slice thickness 3.5 mm, FOV 260 mm, matrix 192, TA 8:1 s, 35 repetitions).

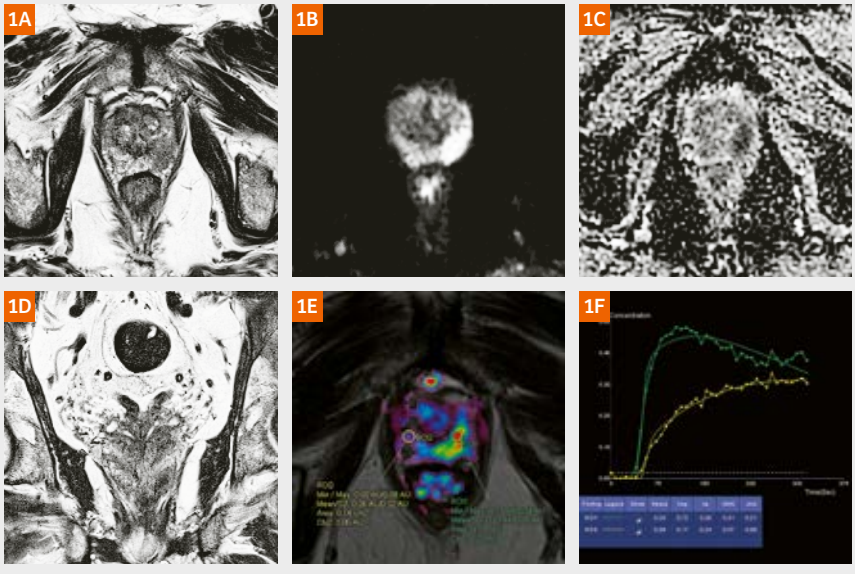

Figure 1: Transversal T2w TSE images **(1A)** demonstrating a suspicious lesion within the left peripheral zone with correspondingly increased signal in the b = 800 s/mm² image **(1B)**, diffusion restriction in the ADC map **(1C)**. The lesion can be confirmed in the coronal T2w images **(1D)**. The parametric map **(1E, K^{trans})** shows a clear focal lesion with a highly suspicious curve **(1F)**.

Dynamic contrast-enhanced images were post-processed using *syngo*.via Tissue 4D.

As illustrated in Figure 1, a lesion in the apical third of the prostate was visible in T2-weighted images as a hypointense, lenticular shaped structure extending more than 1.5 cm with corresponding diffusion-restriction and suspect, focal contrast uptake as well as wash-out in the DCE series. Consequently, the patient was referred to MRI-guided prostate biopsy of the highly suspicious areal in the gland.

Biopsy was performed in a wide-bore MAGNETOM Aera 1.5T system with the patient in supine lithotomy position using a tailored positioning device (Fig. 2, Invivo Germany, Schwerin, Germany). Intra-procedural imaging was undertaken using a combination of a flexible 4-channel coil underneath the patients back and a standard 18-channel body coil positioned on the pelvis of the patient. First, a small, contrast-filled tube was inserted to the patient's rectum and fixated with a highly flexible MR-compatible arm. To define the target for biopsy, fast T2-weighted scans (TR 5000 ms, TE 100 ms, slice thickness 3.5 mm, FOV 200 mm, matrix 256, TA 1:45 min) were performed, while the position and orientation of the contrast-filled needle guide was imaged using a 3D fat suppressed TrueFISP sequence and visualized with a 3D maximum intensity projection (MIP) technique. By simply positioning the center mark of a slice block (Fig. 3, yellow circle) in the center of the lesion, the orientation of the needle guide with respect to the target was checked and the trajectory of the needle guide was iteratively corrected to point to the target. In the given case, only one iteration (repositioning of the needle guide, control scan) was necessary. After contentedly positioning the needle guide, the actual fully-automated biopsy device was inserted and two samples from slightly different positions were taken (Fig. 4). Histopathology revealed a 3 + 3 = 6 acinar adenocarcinoma.

Figure 2: Setup with the customized biopsy device. Patient will be positioned in supine position. A flexible arm (arrow) holds the contrast filled needle guide which is used to define the trajectory to the target and to insert the actual biopsy needle.

Figure 3: Control images to confirm the correct positioning of the needle guide. The center mark (yellow circle, right image) was positioned on the lesion to be biopsied. The left and middle images confirm that the contrast filled needle guide (visible as two bright lines) directly points to the target (yellow circle, arrow).

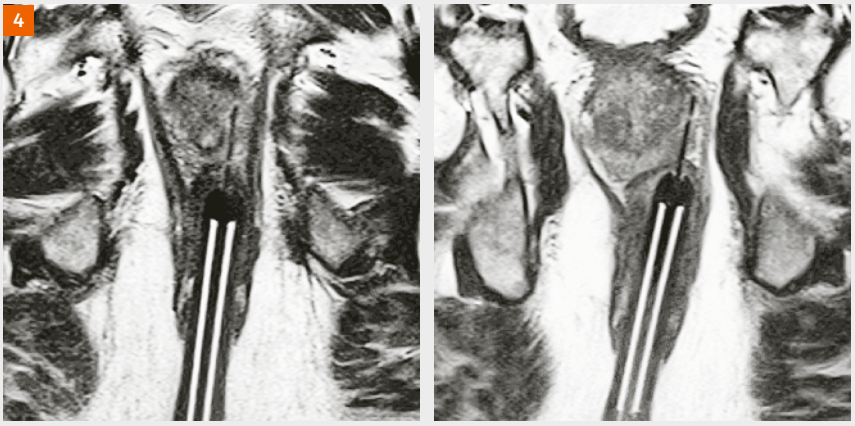

Figure 4: Fast, double-oblique T2w TSE control images confirming the right position of the needle in the lesion before tissue sampling.

Case 2

Patient presented at our department with constantly high PSA values (03/2015: 10.8 ng/ml; 04/2015: 13.0 ng/ml) with a referral for prostate MRI. Diagnostic multiparametric prostate MRI was performed on our 1.5T MAGNETOM Aera and revealed two relatively small lesions in the right and left peripheral zone (Fig. 5). The lesion in the right peripheral zone was selected for MR target biopsy due to better accessibility. During the MR-guided biopsy session, two samples were taken from different positions (Fig. 6). The one taken from the periphery revealed an acinar adenocarcinoma with a Gleason Score of 6 (3 + 3) while the other sample even showed a more aggressive pattern (Gleason Score 3 + 4 = 7).

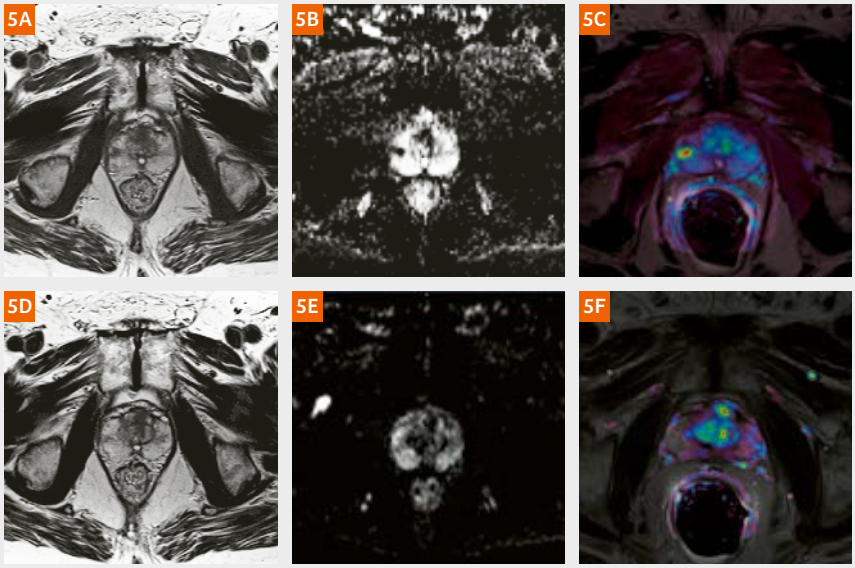

Figure 5: Axial T2w TSE **(5A, D)**, ADC map **(5B, E)**, and K^{trans} maps **(5C, F)**.

Figure 6: After planning the biopsy trajectory **(6A)** the needle was inserted and an oblique control scan was performed. The control scan **(6B)** clearly shows that only the periphery of the lesion is targeted. After minimal repositioning of the needle guide **(6C)** the needle was reinserted and control scan shows optimal positioning of the needle in the lesion.

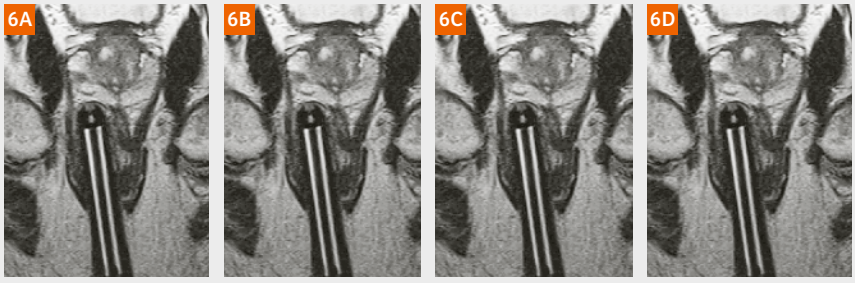

Summary

Targeted biopsies of the prostate under direct MRI-guidance are a reasonable complement to ultrasound biopsy techniques. As shown in the second case presented here, exact targeting of the most suspicious portion of a tumor is crucial for correct classification and consequently best therapy decisions. Especially in case of relatively small lesions, direct MR-guidance has clear advantages over fusion techniques which are always susceptible to intrinsic sources of registration errors.

The targeting procedure presented here, does not require any additional software equipment or extra planning PCs, since it is solely based on standard sequences and planning tools provided with the scanner. Biopsies in a supine position, as performed in Nuremberg, may further improve the acceptance and applicability of MR guided biopsies of the prostate especially in obese, dyspnoeic or elderly individuals.

References

1 Welch HG, Fisher ES, Gottlieb DJ, Barry MJ. Detection of prostate cancer via biopsy in the Medicare-SEER population during the PSA era. J Natl Cancer Inst 2007;99:1395–1400.

2 Churukanti G1, Siddiqui MM1. Prostate cancer: MRI-TRUS fusion biopsy versus 12-core systematic biopsy. Nat Rev Urol. 2015;12:369-71.

3 Sinnott M, Falzarano SM, Hernandez AV et al. Discrepancy in prostate cancer localization between biopsy and prostatectomy specimens in patients with unilateral positive biopsy: implications for focal therapy. Prostate 2012; 72: 1179–86.

4 Epstein JI, Feng Z, Trock BJ, Pierorazio PM. Upgrading and downgrading of prostate cancer from biopsy to radical prostatectomy: incidence and predictive factors using the modified Gleason grading system and factoring in tertiary grades. Eur Urol 2012; 61: 1019–24.

5 Sonn GA, et al. Targeted biopsy in the detection of prostate cancer using an office based magnetic resonance ultrasound fusion device. J Urol. 2013;189: 86-91.

Contact

Florian Schneider, M.D.
Martha-Maria Hospital
Radiology Department

Stadenstr. 58
90491 Nürnberg
Germany
Phone: +49 (0) 911 959-1151
Florian.M.Schneider@web.de

Transurethral MR-Thermometry Guided Ultrasound Ablation of the Prostate – The Heidelberg Experience During Phase I of the TULSA-PRO Device Trial

Maya Mueller-Wolf[1]; Matthias Röthke[1]; Boris Hadaschik[2]; Sascha Pahernik[2]; Joseph Chin[4]; James Relle[5]; Mathieu Burtnyk[6]; Simon Dubler[3]; Johann Motsch[3]; Markus Hohenfellner[2]; Hein-Peter Schlemmer[1]; David Bonekamp[1]

[1] Department of Radiology, German Cancer Research Center (DKFZ), Heidelberg, Germany
[2] Department of Urology, University Hospital Heidelberg, Heidelberg, Germany
[3] Department of Anesthesiology, University Hospital Heidelberg, Heidelberg, Germany
[4] Department of Urology, Western University, London Victoria Hospital, London Health Sciences Center, London, ON, Canada
[5] Department of Urology, Beaumont Health System, Royal Oak, MI, USA
[6] Department of Clinical Affairs, Profound Medical Inc., Toronto, ON, Canada

Background

Prostate cancer (PCa) is the malignancy most commonly diagnosed in men in the western hemisphere. Despite the substantial increase of predominantly low-grade and early stage PCa diagnosed since the appearance of prostate-specific antigen (PSA) screening, PCa remains the second most common cause of cancer-related death in men in the developed world [1], highlighting its aggressive potential and the need for screening and therapy.

The use of prostate-specific antigen (PSA) screening has decreased the average age at diagnosis and increased the proportion of men diagnosed with low-grade, small-volume, localized prostate cancer [2, 3]. Average age at diagnosis is 66 years. While PSA screening is sensitive for prostate cancer, its specificity is low. False positive PSA elevation may be related to benign changes such as prostate hyperplasia (BPH) or prostatitis. Also, PSA and gland size-adjusted parameters such as PSA-density (PSAD) have limited ability to differentiate between BPH and cancer, or between the aggressive life-threatening and low-grade slow-growing forms of the disease [4].

After detection of significant PCa by biopsy, conventional prostate cancer therapy typically consists of either surgical radical prostatectomy or radiation therapy. Due to persistent limitations to predict the aggressiveness of PCa, many patients still receive overtreatment of their disease and are exposed to the associated morbidity with potential long-term erectile dysfunction, urinary incontinence, and bowel complications that may significantly compromise quality of life [5]. It is well-known that low-risk PCa may carry only an insignificant mortality risk compared to men without PCa [6]. Accordingly, the concept of active surveillance (AS) was developed which consists of following patients with low-grade PCa by PSA testing and possibly magnetic resonance imaging (MRI) until significant PCa is detected. Recently, MRI has shown promise to increase detection of PCa compared to standard transrectal ultrasound-guided systematic (TRUS) biopsies [7], with preferential detection of intermediate and higher grade PCa. Negative MRI does currently not exclude significant PCa, although the risk of significant PCa was reported to be lower in patients with negative MRI [8]. The continued improvement of MRI detection, localization and grading of PCa and

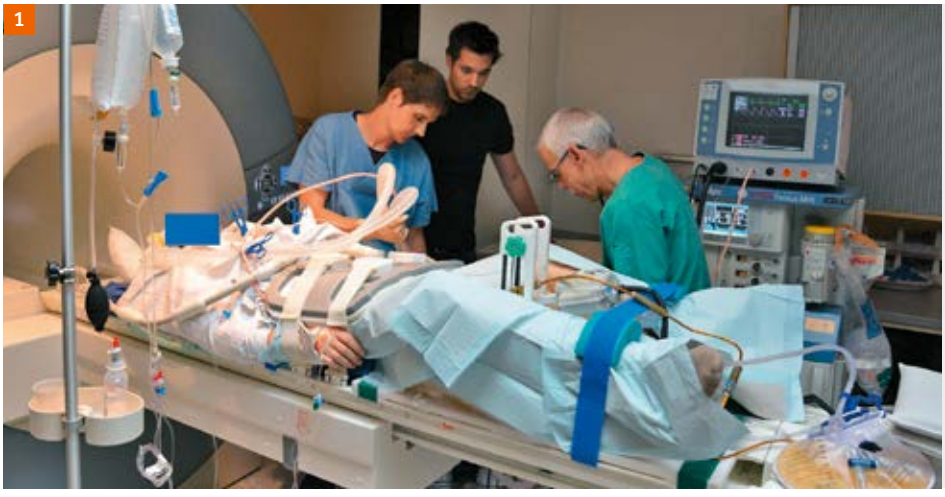

Figure 1: Patient setup in the MRI suite with MR technologist, physicist and anesthesiologist featuring MR-compatible anesthesia machine and monitoring devices needed for general anesthesia on location at the DKFZ Heidelberg, Germany.

growing data on sensitivity and specificity of MR for PCa detection increase the foundation for evidence-based development of alternative, less invasive treatments of PCa by local therapy. This addresses an important need as intermediate therapeutic approaches between AS and radical therapy which provide good control of local disease are highly sought-after. With such therapies it would be possible, both, to tailor therapy to the intermediate-risk group and reduce permanent adverse side effects while also addressing the needs of the growing number of young men diagnosed with small low- to intermediate grade PCa and those of older patients who are not suitable candidates for surgery.

Minimally invasive ablative therapies have the potential to achieve good oncologic outcomes and low morbidity. Adding MR guidance to ablative therapies offers the advantage of direct monitoring of therapy without the need for intermodality co-registration. Furthermore, MR allows temperature monitoring in the form of MR thermometry which can be used to drive a feedback loop for optimal delivery of thermal energy to the target tissue. At the same time, MR-guidance is based on the principal and currently most promising imaging modality for the visualization of PCa. By combining these properties, an MR thermometry-guided ultrasound thermal ablation technique appears very promising to achieve precise lesion targeting and local tumor control. This report is based on our institutional experience during the recent prospective, multi-center, Phase I clinical trial of the TULSA-PRO (described below) device. Within this phase I trial, the TULSA-PRO device was used to heat and ablate prostate tissue in 30 men with localized prostate cancer. Of the 30 men included in the trial, 14 were treated at our site in Heidelberg. All procedures were performed within a 3T Siemens MAGNETOM Tim Trio MR system. Twelve-month follow-up results of the phase I trial have been analyzed and published [9]. The objective of the phase I trial was to determine the clinical safety and feasibility of the TULSA-PRO device for whole-gland prostate ablation in the primary treatment setting of patients with localized prostate cancer. As the precision of targeting was being evaluated during the trial, all treatments included a 3-mm safety margin to the prostate capsule with an expected 10% residual viable prostate tissue expected around the ablation margin.

TULSA overview

MRI Guided **T**ransurethral **UL**trasound **A**blation (TULSA) is a novel, minimally invasive technology that ablates the entire prostate gland, via the urethra. It combines quantitative image-based planning, monitoring, and treatment control with transurethral delivery of therapeutic ultrasound to ablate prostate tissue (both benign and malignant) through thermal coagulation [9, 10].

The procedure is conducted within an MRI scanner (Fig. 1), which provides high-resolution planning images that are registered to real-time quantitative thermometry images acquired during treatment. A closed-loop temperature feedback control algorithm modulates the intensity, frequency, and rotation rate of the ultrasound, shaping the ablation volume with high accuracy to individual prostate anatomy and reducing the risk of possible damage to peri-prostatic structures (rectum, urinary sphincter and neurovascular bundles) [11].

The MRI scanner provides real-time thermal dosimetric monitoring for feedback-controlled ultrasound ablation.

TULSA-PRO™ technical principle

During the phase I clinical trial, we used the TULSA-PRO device developed by Profound Medical Inc. (Toronto, Canada).

The TULSA-PRO System components are depicted in Figure 2. A rigid Ultrasound Applicator (UA) is inserted into

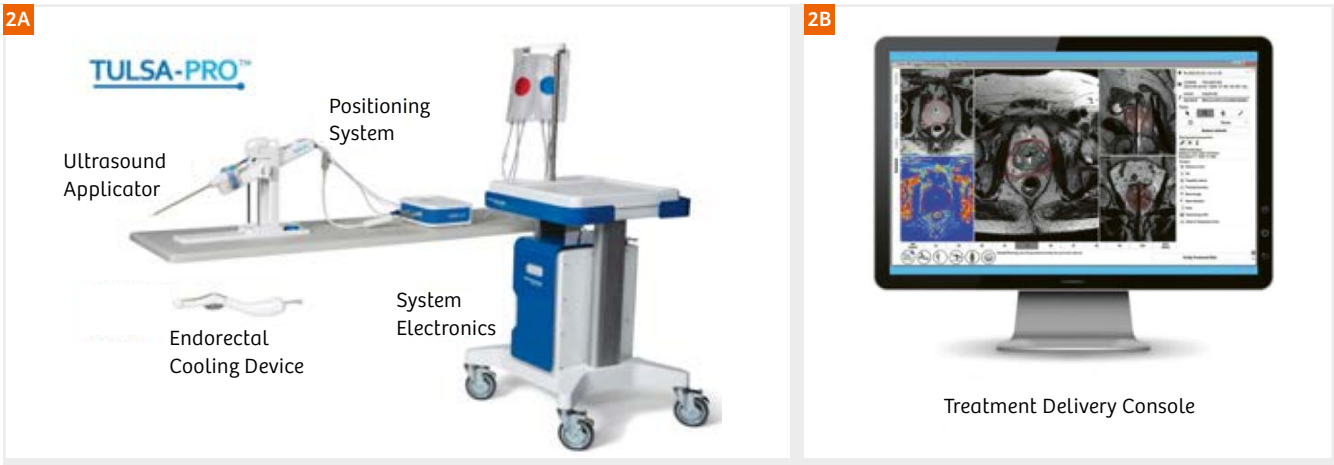

Figure 2: TULSA-PRO System Components. The Ultrasound Applicator, Endorectal Cooling Device and Positioning System are inside the Scanning room on the MRI bed. The Treatment Delivery Console and System Electronics remain outside the Scanning room, in the Console and Equipment room, respectively. *Figure courtesy of Profound Medical Inc.*

the urethra, making contact with and delivering ultrasound energy directly into the prostate gland. A linear array of 10 independent ultrasound transducer elements emits directional (but unfocused) high-intensity ultrasound energy directly into the adjacent prostate, quickly raising tissue temperatures to thermal coagulation. The configuration of the ultrasound beams enables treatment of a large volume of prostate tissue, resulting in shorter treatment times of typically less than 40 minutes. Fluid is circulated through the UA, providing 1–2 mm of urethral tissue preservation. A separate circuit flows water through the Endorectal Cooling Device (ECD) to provide thermal protection of rectal tissue during ultrasound ablation delivery. Figure 3 shows a conceptual illustration and a sagittal MR image of the UA and ECD in a patient.

The UA is held in situ with a Positioning System (PS) that provides remote robotic linear and rotational motion of

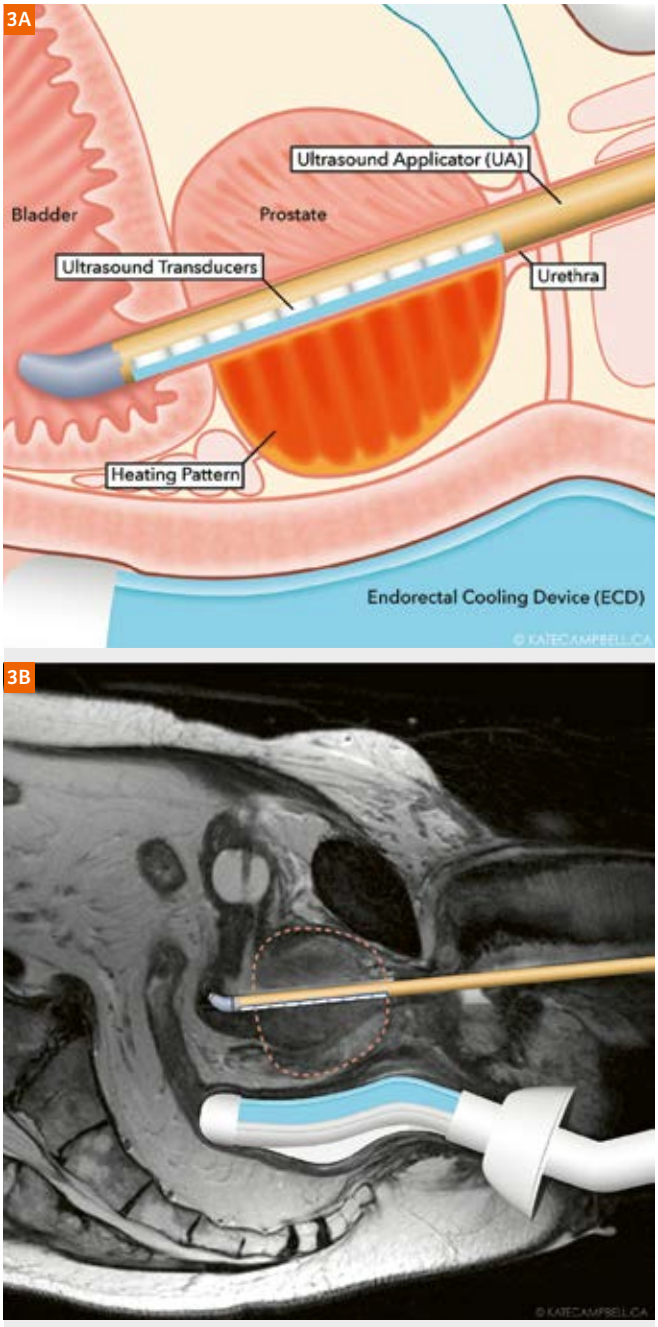

Figure 3: Conceptual illustration **(3A)** and sagittal MR image **(3B)** of the UA and ECD in a patient.
Figure courtesy of Profound Medical Inc.

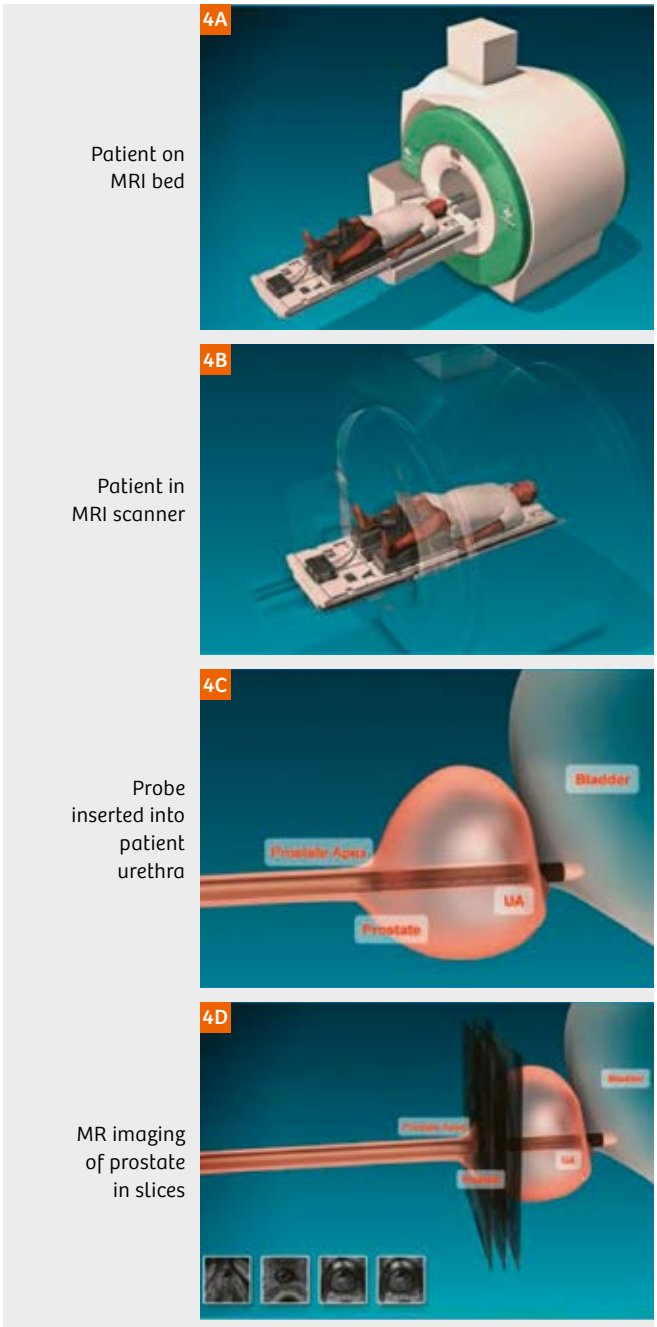

Figure 4: Conceptual illustration **(3A)** and sagittal MR image **(3B)** of the UA and ECD in a patient.
Figure courtesy of Profound Medical Inc.

the device within the prostate. During treatment, the UA is rotated continuously by the PS, ensuring a continuous pattern of thermal damage and preventing cold spots between ultrasound sonications. The System Cart (SC) positioned in the MRI equipment room, houses the fluid circuits and the System Electronics (SE), which power the UA transducer elements and PS motors.

The treatment is conducted completely within an MRI, providing real-time temperature images of the heated region to be acquired as the ultrasound treatment is delivered. A custom software interface (Treatment Delivery Console, TDC) communicates with the MR scanner to display high-resolution images for device positioning and treatment planning, and temperature images for treatment monitoring and control. Using MRI thermometry during treatment, dynamic temperature feedback control over the intensity of the ultrasound beams and rotation of the UA can shape the pattern of thermal coagulation accurately and precisely in the prostate gland, thereby reducing the risk of possible damage to important surrounding anatomy, such as, the rectum, urinary sphincters and neurovascular bundles [11].

During the procedure, the software automatically adjusts ultrasound parameters (power, frequency, and device rotation rate) to achieve at least the target temperature (≥ 55°C) within the target boundary. Prostate tissue temperature feedback is provided from the MR scanner in real-time during the procedure and is displayed in the form of a temperature map (see Fig. 5).

The procedure

Patients undergo general anesthesia prior to insertion of suprapubic catheter and a transurethral guidewire. The patient is then moved onto the MR bed and the UA is inserted manually over the guidewire, followed by the ECD (Fig. 4A).

Under MR guidance and remote operation of the robotic PS, the UA is positioned precisely within the prostatic urethra (Figs. 4B and 4C). High-resolution prostate MR images are acquired for treatment planning (T2-weighted turbo spin echo, echo/repetition time 52/3000 ms, 26-cm field of view, 1 x 1 x 2.5 mm^3 voxels). Using the TDC, the physician traces the outer prostate boundary on oblique-axial images acquired transverse to the UA and aligned with each transducer element (Fig. 4D).

The target prostate volume is defined from the outer prostate boundary drawn by the physicians, and heated to ≥55°C, the temperature critical to achieve acute thermal coagulation (Fig. 5). Treatment begins with high-intensity ultrasound energy delivered to the prostate in one complete rotation of the UA under active MRI thermometry feedback control (proton resonance frequency shift method, echo planar imaging, oblique-axial aligned with planning images, echo/repetition time 8/350 ms, 26-cm field of view, 2 x 2 x 4 mm^3 voxels, 0.8°C average precision *in vivo* human prostate). Real-time MRI thermometry images are acquired every 5.9 s, providing continuous assessment of a three-dimensional temperature volume during treatment. After treatment, contrast-enhanced (CE) MRI may be acquired to confirm non-perfused tissue volume.

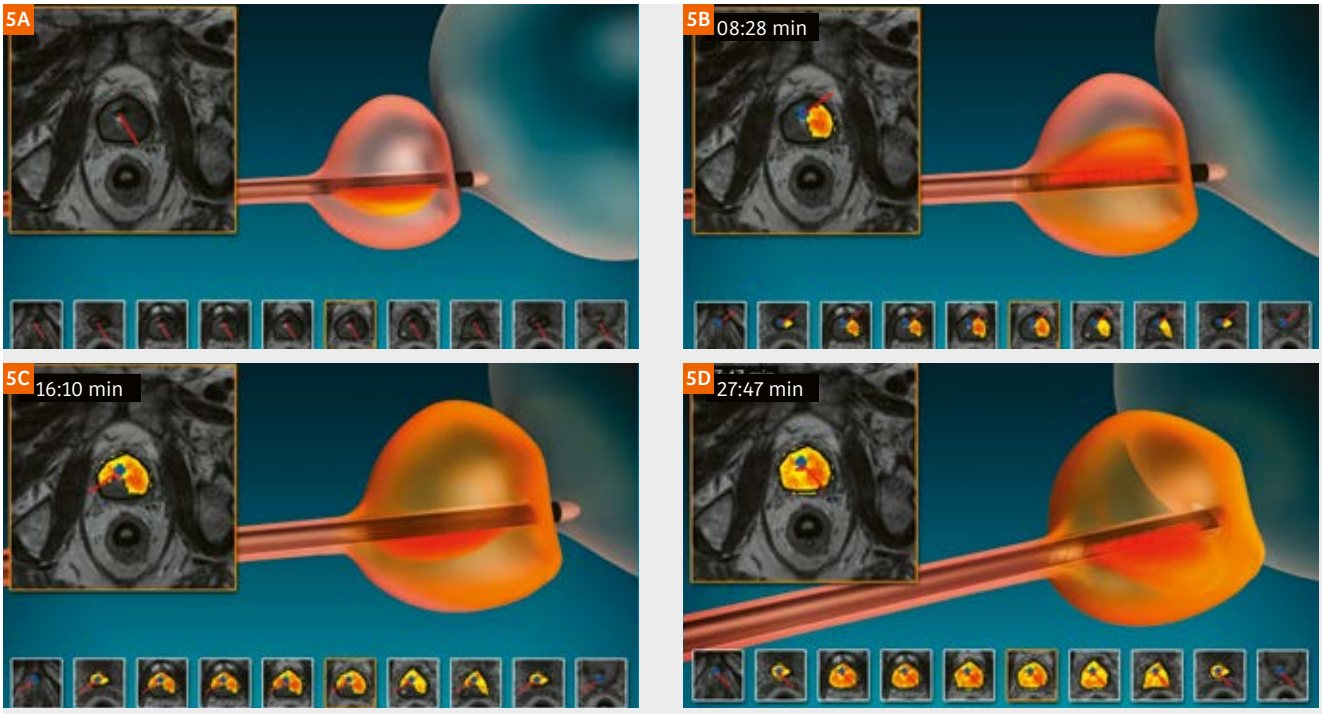

Figure 5: Temporal evolution of a MRI-guided TULSA treatment, completed in one full rotation of the UA.
Figure courtesy of Profound Medical Inc.

Case 1

A 70-year-old patient in good health, initially managed on active surveillance, was enrolled in the Phase I study and treated with the TULSA-PRO. In 2012, the patient presented with a PSA of 6.3 ng/ml, clinical stage T1c and initial biopsy showing 1/12 positive cores with Gleason Score 3+3. In 2013, the patient's PSA increased to 7.5 ng/ml and he subsequently underwent a second biopsy, this time with 6/26 positive cores with Gleason Score 3+3. The patient then enrolled in the TULSA-PRO study and was treated in October 2013.

The prostate volume was 33 cc, and the duration of the ultrasound treatment was 25 min. Figure 6A shows an example mid-gland MR thermometry image demonstrating the millimeter accuracy and precision of prostate ablation. Thermometry findings are confirmed on post-treatment CE-MRI with the hypointense region of non-perfused tissue concordant with the region of cytoablative thermal treatment (Fig. 6B). Figures 6C and D illustrate the prostate anatomical changes at 12 months, demonstrating an 85% decrease in gland volume.

Figure 7 illustrates the changes in PSA and patient quality of life following treatment with the TULSA-PRO. PSA reached a nadir of <0.10 ng/ml at 1 month and remained stable to 0.25 ng/ml at 24 months. The International Prostate Symptom Score (IPSS, range from 0 "no symptoms" to 35 "severe symptoms") initially increased at 1 month and returned to baseline at 3 months after treatment with the TULSA-PRO, further decreasing at 24 months. Internal Index of Erectile Function (IIEF) Item 2 (erection firmness sufficient for penetration, range from 0 "never or almost never" to 5 "always or almost always") remained unchanged after treatment with the TULSA-PRO through 24 months of follow-up. This patient presented with a total of one adverse event attributable to treatment with the TULSA-PRO, which was an asymp-tomatic urinary tract infection that was resolved with oral antibiotics. At 12 months, the patient's 12-core transrectal follow-up biopsy was negative for adenocarcinoma.

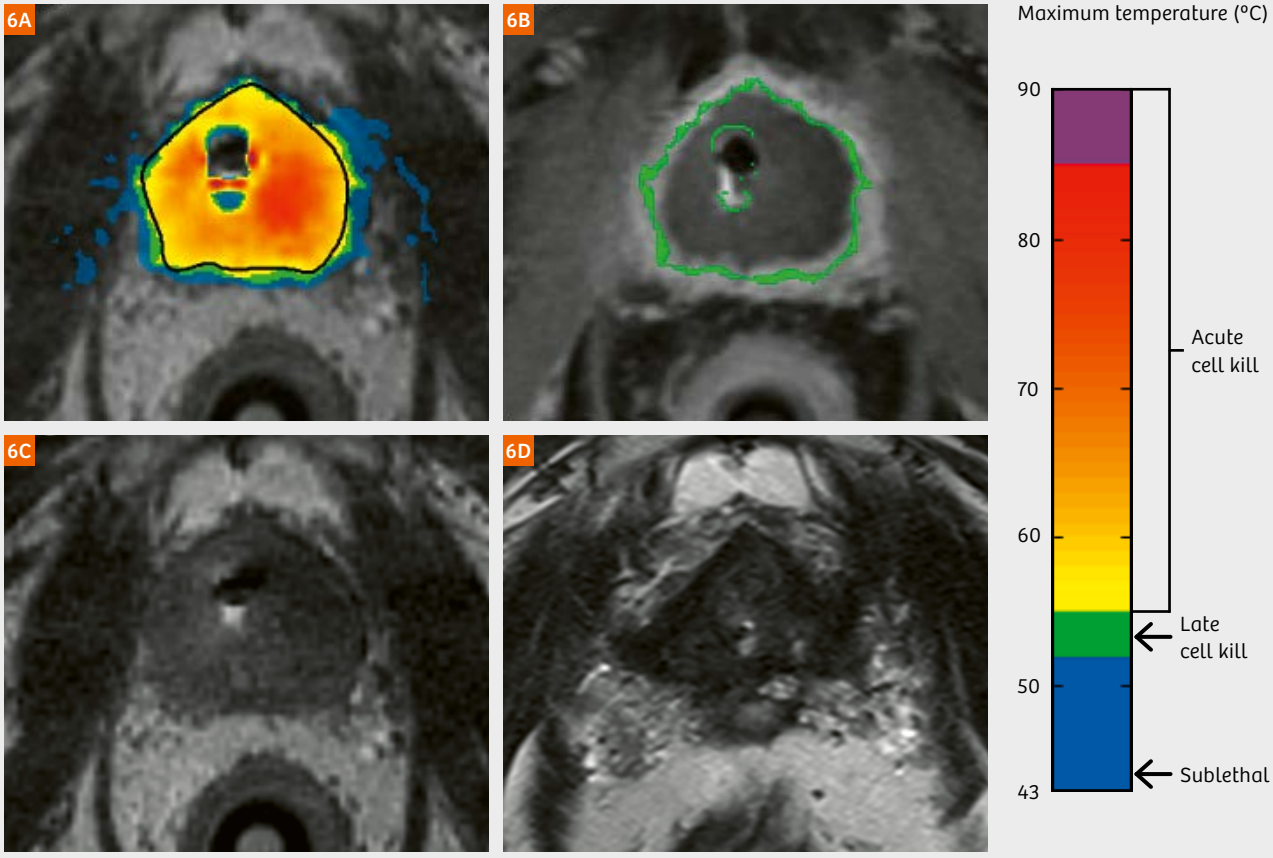

Figure 6: MRI findings of case study patient, with example images through the mid-gland. **6A** shows the maximum temperature reached in the prostate measured using real-time MR thermometry; the acute cell kill target temperature ≥ 55°C was shaped accurately and precisely to the treatment plan (black contour). **6B** shows the CE-MRI acquired immediately after treatment, demonstrating the hypointense region of non-perfused prostate tissue concordant with the ablative temperatures on MR thermometry. **6C** shows the corresponding treatment planning image (Day 0), which is compared to **6D** showing the same location at 12-month follow-up.

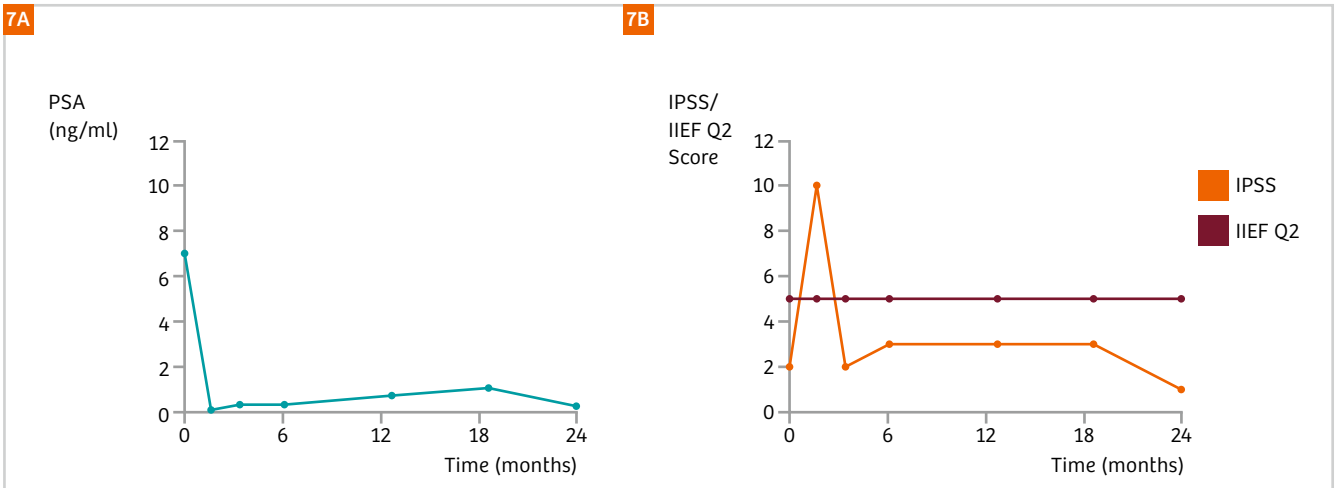

Figure 7: PSA and Quality of Life outcomes for case study patient (TULSA-PRO treatment at time 0). **7A** shows the PSA decreasing to <0.10 ng/ml at 1 month after treatment with the TULSA-PRO, and stable to 0.25 ng/ml at 24 months. **7B** shows the IPSS score [range 0 (no symptoms) to 35 (severe symptoms)] increase at 1 month and return to baseline at 3 months after treatment with the TULSA-PRO, further decreasing at 24 months. IIEF Q2 score (erection firmness sufficient for penetration) [range 0 (never or almost never) to 5 (always or almost always)] remains unchanged after treatment with the TULSA-PRO through 24 months of follow-up.

Case 2

A 68-year-old patient with an initial PSA of 9.1 ng/ml and a Gleason Score of 3+3 was treated with TULSA-PRO in March 2014. Prostate volume was 58 cc requiring a longer than average ultrasound treatment time of 58 min. Prior to treatment, the patient had IPSS of 20 (severe symptoms), which decreased to 11 and 9 (both moderately symptomatic) at 3 and 24 months, respectively. Baseline IIEF item 2 score was 2, and remained stable to 2 and 3, at 3 and 24 months, respectively. Side effects associated with the procedure were urinary tract infection, resolved with oral antibiotics, and obstructive micturition, requiring prolonged post-treatment catheterization from 2 weeks (per-protocol) to 5 weeks.

Following treatment the PSA value decreased to 1.0 ng/ml at 1 month, 0.9 ng/ml at 3 months, 0.7 ng/ml at 6 months, and remaining stable at 0.55 ng/ml at 24 months. Biopsy at 12 months was negative. Figure 8 shows this patient's treatment day and 12 months' mid-gland MR images.

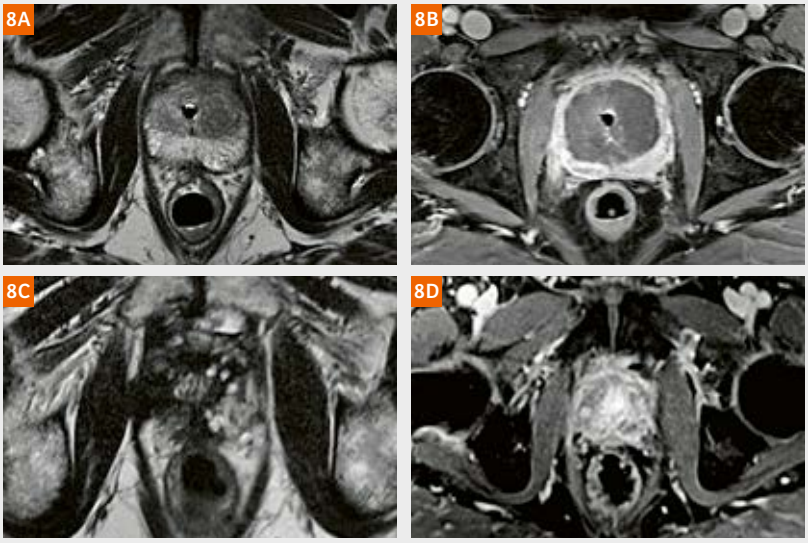

Figure 8: MRI findings of case study II patient. Example images through the mid-gland on treatment day **(8A, B)** and at 12 months **(8C, D)**. **8A** shows the axial T2-weighted treatment planning image, used to define the target boundaries for the real-time MR thermometry algorithm. **8B** shows the T1-weighted fatsat contrast-enhanced image acquired immediately following treatment. It demonstrates accurate ablation with the hypointense region of non-perfused prostate tissue and demonstrates the peripheral security margin of 3 mm used in the phase I trial, which will be reduced in the up-coming Pivotal trial. **8C** shows the axial T2-weighted image of the prostate gland at 12 months. Prostate volume is significantly reduced and T2 hypointense scarring is seen. **8D** demonstrates the low post-treatment prostate volume at the 12 month follow-up on a T1-weighted fatsat contrast-enhanced image with enhancement corresponding to a mixture of fibrotic tissue and remaining peripheral prostate tissue.

Parameter (n=30)		Average	Std Deviation	Median	IQR
Patient Age (years)		69.0	3.7	69	67–71
Prostate Volume (cc)		47.6	17.2	44	38–48
Ultrasound Treatment Time (min)		35.8	10.4	36	26–44
Thermal Ablation Accuracy (mm)		0.1	0.4	0.1	−0.3–0.4
Thermal Ablation Precision (mm)		1.3	0.4	1.3	1.0–1.5
Median Value (IQR)	**Baseline**	**1 month**	**3 months**	**6 months**	**12 months**
IPSS	8 (5–13)	14 (11–19)	6 (4–10)	5 (3–8)	5 (4–7)
IIEF item 2	13 (6–28)	7 (2–12)	11 (4–18)	11 (4–19)	13 (5–25)
Bowel Habits	100 (90–100)	100 (80–100)	100 (89–100)	100 (89–100)	100 (100–100)
PSA (ng/ml)	5.8 (3.8–8.0)	0.8 (0.5–1.1)	0.9 (0.4–1.7)	0.8 (0.4–1.1)	0.8 (0.6–1.1)

Table 1: Results summary of the prospective 12-month Phase I follow-up data.

Results summary of the TULSA-PRO prospective phase I study

An analysis of the prospective 12-month Phase I follow-up data showed that the TULSA-PRO is spatially accurate and precise to ablate prostate tissue, both malignant and benign, to millimeter accuracy, while providing a favourable safely profile and a low rate of erectile dysfunction [9].

Of the 30 study subjects, median (IQR) age was 69 (67–71) years, with 24 (80%) low-risk and 6 (20%) intermediate-risk cancers (D'Amico criteria). As summarized in Table 1, ultrasound treatment time was 36 (26–44) min and prostate volume 44 (38–48) cc. Spatial control of ablation was 0.1 ± 1.3 mm (spatial accuracy of 0.1 mm, precision of ± 1.3 mm). Adverse events (CTCAE v4) included haematuria Grade 1 (asymptomatic) in 13 patients (43%), and Grade 2 (symptomatic) in 2 patients (6.7%); urinary tract infections Grade 2 in 10 patients (33%); acute urinary retention Grade 1 (blocked suprapubic catheter) in 3 patients (10%), and Grade 2 (prolonged catheterization) in 5 patients (17%); and epididymitis Grade 3 (resolved with IV antibiotics) in 1 patient (3.3%). There were no rectal injuries or intraoperative complications.

Baseline IPSS of 8 (5–13) recovered to 6 (4–10) at 3 months, stable to 5 (4–7) at 12 months (n=29). The proportion of patients with erections sufficient for penetration (IIEF item 2 ≥ 2) remained unchanged from 21/30 (70%) at baseline to 20/29 (69%) at 12 months. Median PSA decreased 87% at 1 month, stable to 0.8 (0.6–1.1) ng/ml at 12 months (n=30). Positive biopsies at 12 months show 61% reduction in total cancer length, clinically significant disease in 9/29 patients (31%), and any disease in 16/29 patients (55%).

Conclusions

Here we report our initial experience with the TULSA-PRO device during a recently completed comprehensive prospective Phase I study, with Heidelberg being the center that has enrolled most of the patients into the trial. The TULSA-PRO device offers a novel, MRI-guided, minimally-invasive method to safely ablate target benign and malignant prostate tissue with millimeter accuracy and precision. Real-time MR thermometry performed during transurethral ultrasound delivery enables active feedback control of the thermal volume, with high success in the ablation of the target tissue. Furthermore, MRI-guidance allows acquisition of high-resolution images of the prostate for accurate treatment planning without the need for fusion algorithms. The TULSA-PRO device demonstrated conformal thermal ablation of target prostate volumes with a favorable side-effect profile and minor or no impact on urinary, erectile and bowel function, while maintaining a security margin of 3 mm to the prostate capsule during the phase I trial. In the upcoming Pivotal trial, and after assessment of millimeter accuracy during phase I, the security margin will be reduced further to allow treatment of the most peripheral portions of prostatic tissue.

TULSA-PRO has the potential to be an effective therapy option for clinicians and their patients diagnosed with localized prostate disease. The effectiveness of the device continues to be evaluated through the upcoming prospective pivotal study, with a 110-patient trial being established in over 10 institutions across Europe (Germany, The Netherlands, Spain), Canada and the United States.

References

1 Carlsson S and Vickers A, "Spotlight on prostate cancer: the latest evidence and current controversies," BMC Medicine 13:60 (2015).
2 Cooperberg M, Broering J, Kantoff P and Carroll P, "Contemporary trends in low risk prostate cancer: risk assessment and treatment," The Journal of Urology 178(3 Pt 2): S14-9 (2007).
3 Neutel C, Gao R, Blood P and Gaudette L, "The changing age distribution of prostate cancer in Canada," Canadian Journal of Public Health 98(1): 60-4 (2007).
4 Hammerer P, Kattan M, Mottet N and Prayer-Galetti T, "Using prostate-specific antigen screening and nomograms to assess risk and predict outcomes in the management of prostate cancer," BJU International 98(1): 11-9 (2002).
5 Thompson I, Thrasher JB, Aus G, Burnett AL, Canby-Hagino ED, Cookson MS, D'Amico AV, Dmochowski RR, Eton DT, Forman JD, Goldenberg SL, Hernandez J, Higano CS, Kraus SR, Moul JW, Tangen CM; AUA Prostate Cancer Clinical Guideline Update Panel, "Guideline for the management of clinically localized prostate cancer: 2007 update," The Journal of Urology 177(6): 2106-31 (2007).
6 Rider JR, Sandin F, Andrén O, Wiklund P, Hugosson J, Stattin P. Long-term outcomes among noncuratively treated men according to prostate cancer risk category in a nationwide, population-based study. Eur Urol. 2013 Jan;63(1):88-96. doi: 10.1016/j.eururo.2012.08.001. Epub 2012 Aug 10. PMID: 22902040
7 Siddiqui MM, Rais-Bahrami S, Truong H, Stamatakis L, Vourganti S, Nix J, Hoang AN, Walton-Diaz A, Shuch B, Weintraub M, Kruecker J, Amalou H, Turkbey B, Merino MJ, Choyke PL, Wood BJ, Pinto PA. Magnetic resonance imaging/ultrasound-fusion biopsy significantly upgrades prostate cancer versus systematic 12-core transrectal ultrasound biopsy. Eur Urol. 2013 Nov;64(5):713-9. doi: 10.1016/j.eururo.2013.05.059. Epub 2013 Jun 12.
8 Dianat SS, Carter HB, Pienta KJ, Schaeffer EM, Landis PK, Epstein JI, Trock BJ, Macura KJ. Magnetic resonance-invisible versus magnetic resonance-visible prostate cancer in active surveillance: a preliminary report on disease outcomes. Urology. 2015 Jan;85(1):147-53. doi: 10.1016/j.urology.2014.06.085. Epub 2014 Oct 16.
9 Chin JL1, Billia M2, Relle J3, Roethke MC4, Popeneciu IV5, Kuru TH5, Hatiboglu G5, Mueller-Wolf MB4, Motsch J5, Romagnoli C2, Kassam Z2, Harle CC2, Hafron J3, Nandalur KR3, Chronik BA2, Burtnyk M6, Schlemmer HP4, Pahernik S5. Magnetic Resonance Imaging-Guided Transurethral Ultrasound Ablation of Prostate Tissue in Patients with Localized Prostate Cancer: A Prospective Phase 1 Clinical Trial. Eur Urol. 2016 Jan 6. pii: S0302-2838(15)01238-5. doi: 10.1016/j.eururo.2015.12.029. [Epub ahead of print]
10 Chopra R, Colquhoun A, Burtnyk M, N'djin WA, Kobelevskiy I, Boyes A, Siddiqui K, Foster H, Sugar L, Haider MA, Bronskill M and Klotz L, "MR imaging-controlled transurethral ultrasound therapy for conformal treatment of prostate tissue: initial feasibility in humans," Radiology 265(1): 303-13 (2012).
11 Burtnyk M, Chopra R and Bronskill M, "Simulation study on the heating of the surrounding anatomy during transurethral ultrasound prostate therapy: A 3D theoretical analysis of patient safety," Medical Physics 37(6): 2862-75 (2010).
12 Fütterer JJ, Briganti A, De Visschere P, Emberton M, Giannarini G, Kirkham A, Taneja SS, Thoeny H, Villeirs G and Villers A, "Can clinically significant prostate cancer be detected with multiparametric magnetic resonance imaging? A systematic review of the literature," European Urology 68(6): 1045-53 (2015).
13 American Cancer Society, http://www.cancer.org/cancer/prostatecancer

Contact

David Bonekamp, M.D.
Department of Radiology – E010
German Cancer Research Center (DKFZ)

Im Neuenheimer Feld 280
69120 Heidelberg
Germany
d.bonekamp@dkfz-heidelberg.de

Hybrid PET/MR Imaging with PSMA-Ligands: the Future Standard in the Diagnosis of Prostate Cancer?

Ali Afshar-Oromieh, M.D.[1,2]; Martin T. Freitag, M.D.[3]; Matthias C. Röthke, M.D.[3]; Jan P. Radtke, M.D.[3,4]; Heinz Peter Schlemmer, M.D.[3]

[1] Department of Nuclear Medicine, Heidelberg University Hospital, Heidelberg, Germany
[2] Clinical Cooperation Unit Nuclear Medicine, German Cancer Research Center (DKFZ), Heidelberg, Germany
[3] Department of Radiology (E010), German Cancer Research Center (DKFZ), Heidelberg, Germany
[4] Department of Urology, University Hospital Heidelberg, Germany

Prostate cancer (PCa) is the most frequent malignant tumor in men worldwide [1, 2]. Following initial therapy, mostly by surgery or radiation, biochemical relapse is rather common [3–6]. The search for tumor lesions at this constellation is challenging, since imaging modalities such as Computed Tomography (CT) and Magnetic Resonance Imaging (MRI) often revealed unsatisfying sensitivity and specificity [7].

Research has therefore sought to find more sensitive and specific ways of diagnostic measures. The fact that prostate-specific membrane antigen (PSMA) is known to be overexpressed in most PCa offers the chance to develop ligands for this target. This has led to the introduction of the low-molecular-weight PSMA-ligand Glu-NH-CO-NH-Lys-(Ahx)-[^{68}Ga(HBED-CC)] (= ^{68}Ga-PSMA-11) in 2011 as a novel PET-tracer for diagnosing PCa. This compound was developed at the German Cancer Research Center Heidelberg, Germany [8, 9]. The first clinical application of ^{68}Ga-PSMA-11-PET/CT was conducted in May 2011 in the department of nuclear medicine at the Heidelberg University Hospital. This led to the rapid international spread of this novel imaging method. The growth can be explained by the hitherto existing results of PET/CT-imaging with ^{68}Ga-PSMA-11, which clearly demonstrate a significant increase in the diagnostic capabilities for the detection of PCa-related tissue [10–13]. A recently published study with a large patient cohort (n = 319) affirmed that ^{68}Ga-PSMA-11-PET/CT provides excellent sensitivity and specificity to detect PCa lesions [12]. Other groups have confirmed these findings [14].

When compared to CT, MRI provides a better method of soft tissue imaging due to its higher contrast-resolution and different functional sequences, both helping to clarify uncertain findings. Multiparametric MRI of the prostate has been proven as a powerful imaging tool for prostate cancer assessment [15]. It provides essential information for accurate prostate biopsy using TRUS/MR image-fusion guided biopsy systems, and is an integral part of follow-up during active surveillance and individualized therapy planning [16]. However, there are significant limitations in the early detection of cancer spreading into lymph nodes and bones, or of recurrent disease after curative intended treatment. These limitations can be overcome by adding the information from PSMA-PET, which yields complementary information compared to multiparametric MR. Consequently, the next step should therefore be a combination of PSMA-PET with MRI, thus creating the best possible tool to detect, diagnose, stage and follow-up patients with suspected prostate cancer comprehensively and most accurately within 'one-stop-shopping'.

[1] The full prescribing information can be found at page 59.

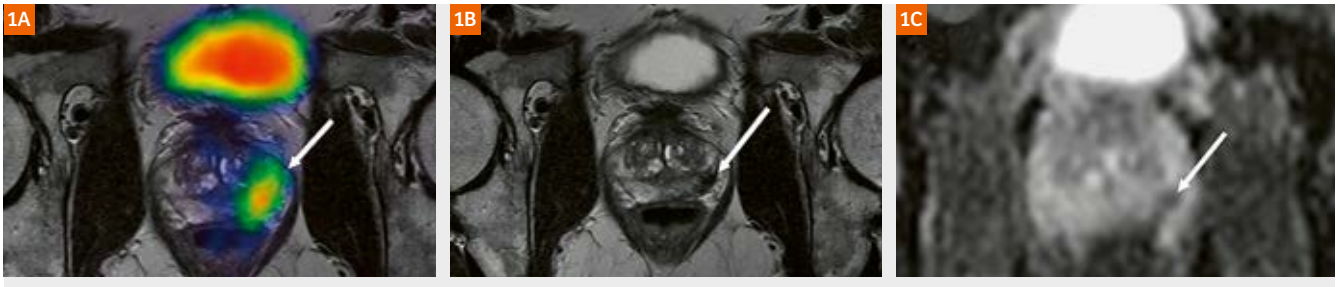

Figure 1: Patient with prostate cancer (Gleason 9, cT3, PSA 26 ng/ml) presenting with focal T2w hypointensity, pathologic uptake in PSMA-PET and focal ADC decrease in the peripheral zone (white arrows). The PSMA-ligand is excreted via the urinary tract (in the upper part of 1A radioactive urine is visible within the bladder). **(1A)** PSMA-PET/MRI fusion with T2w high-resolution. **(1B)** T2w high-resolution TSE sequence. **(1C)** ADC map.

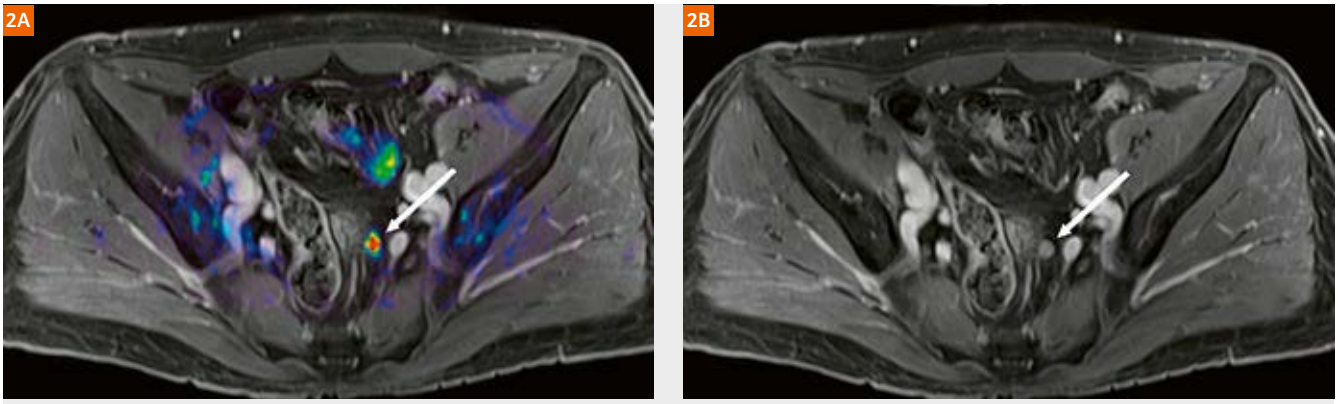

Figure 2: Patient with biochemical relapse after radical prostatectomy (Gleason 9, T2a, PSA at scan 3.6 ng/ml). PSMA-PET/MRI identifies a typical lymph node metastasis next to the left internal iliacal artery (white arrows). **(2A)** PSMA-PET/MRI fusion with **(2B)** T1w-CE-fatsat.

Siemens is the first company to have successfully developed a hybrid whole-body PET/MRI scanner allowing for simultaneous PET and MRI assessment. The objective of such hybrid scanners is a faster investigation and more accurate image fusion compared to separately conducted PET and MRI images.

As dedicated software to fuse separately acquired PET and MRI images already exists, some experts may argue that the development of hybrid PET/MRI scanners was a bit futile. Bearing in mind that very similar arguments were raised at the time of hybrid PET/CT scanner devel-opment, the ensuing years have clearly showed multiple advantages of those scanners: the image fusion was found to be more accurate when compared to the images that were reconstructed based on retroactive fusion of separately obtained PET and CT/MRI images. Human errors in the context of image fusion could also be avoided as no manipulation by humans is required. All this has resulted in saved time and resources. Furthermore, with regard to external radiation therapy, the development of hybrid PET/CT has enabled more accurate therapy approaches. In addition, PET/MRI allows parallel acquisition of PET and MRI, whereas for PET/CT the scans have to be conducted sequentially. At last, patients who undergo a PET/MRI scan are also exposed to less radiation compared to PET/CT.

After the development of hybrid whole-body PET/MRI scanners, multiple studies have been published which demonstrate the feasibility and the advantages of a PET/MRI hybrid system when using ^{18}F-FDG or ^{18}F-Choline. In 2013, our group began conducting PET/MRI with ^{68}Ga-PSMA-11 and the results were highly promising [9–12]. In fact, a subjectively easier evaluation of the images compared to PET/CT could be shown; an effect enabled by different diagnostic sequences and the higher resolution of MRI. The combination of the ^{68}Ga-PSMA-11-PET with multiparametric MRI provided images of a high diagnostic value not witnessed before (Figs. 1, 2). MRI has also helped to clarify unclear findings in PET/CT regarding PCa metastases (Fig. 3). The appearance of a reduced PET-signal around the urinary bladder in some patients was the only noticeable limitation compared to PET/CT [12]. However, there are strategies for reducing or even omitting the described effect, i.e. a sufficient hydration of the patients, voiding the bladder prior to acquisition and starting the examination with the pelvis when the bladder is less full. Further, a newly developed software offering two different types of scatter correction (relative and absolute scatter correction) can help to significantly reduce the described effect.

In summary, the authors strongly believe that hybrid ^{68}Ga-PSMA-PET/MRI has significant advantages over PET/CT and will create new options for the diagnosis and selective treatment of primary and recurrent PCa in the future.

Acknowledgements

We express our gratitude to our staff, in particular to Regula Gnirs, René Hertel and Dr. Henrik Hetzheim.

References

1 Jemal A, Bray F, Center MM, Ferlay J, Ward E, Forman D. Global cancer statistics. CA. Cancer J. Clin. 2011;61:69–90.
2 Siegel R, DeSantis C, Jemal A. Colorectal cancer statistics, 2014: Colorectal Cancer Statistics, 2014. CA. Cancer J. Clin. 2014; 64:104–17.
3 Simmons MN, Stephenson AJ, Klein EA. Natural History of Biochemical Recurrence after Radical Prostatectomy: Risk Assessment for Secondary Therapy. Eur. Urol. 2007;51:1175–84.
4 Suardi N, Porter CR, Reuther AM, Walz J, Kodama K, Gibbons RP, et al. A nomogram predicting long-term biochemical recurrence after radical prostatectomy. Cancer. 2008;112:1254–63.
5 Boorjian SA, Thompson RH, Tollefson MK, Rangel LJ, Bergstralh EJ, Blute ML, et al. Long-Term Risk of Clinical Progression After Biochemical Recurrence Following Radical Prostatectomy: The Impact of Time from Surgery to Recurrence. Eur. Urol. 2011;59:893–9.

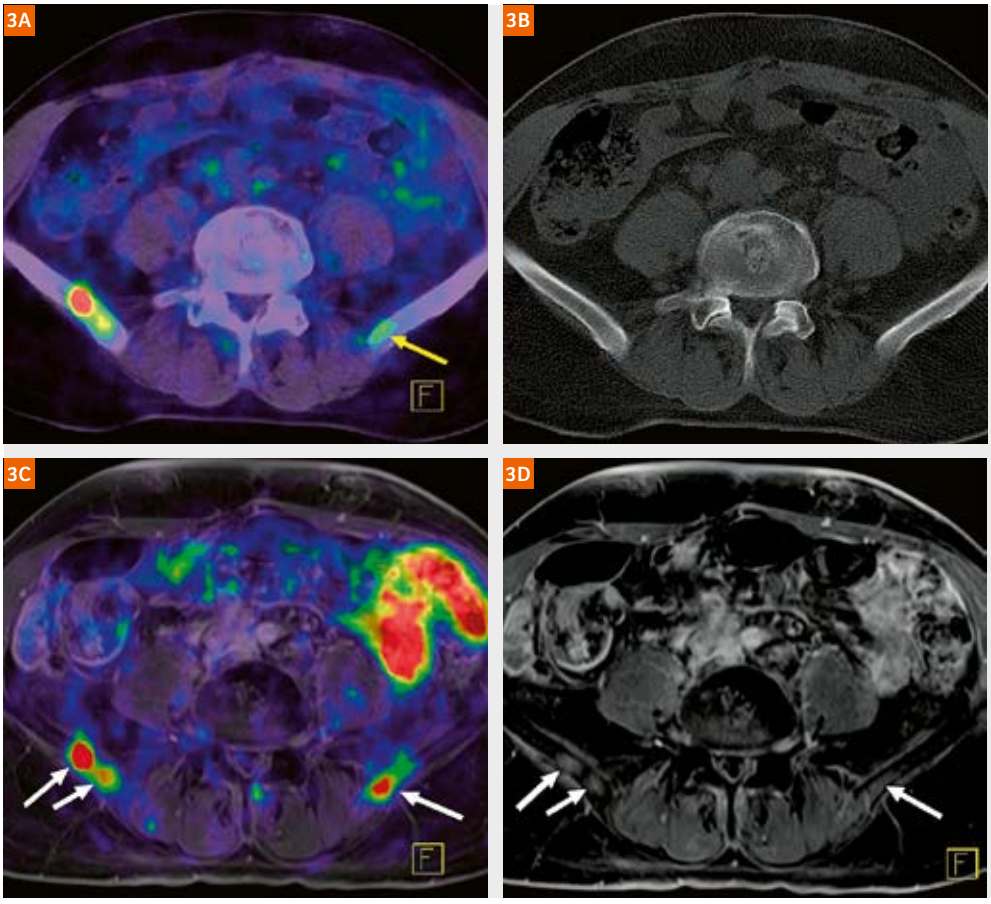

Figure 3: ^{68}Ga-PSMA-11-PET/CT **(3A, B)** and PET/MRI **(3C, D)** of a patient with rising PSA levels. This is an example of the potential of MRI to clarify even moderate PSMA-tracer accumulations as visible in the PET/CT (yellow arrow in 3A): while there is no correlation in CT, white arrows in 3D point to pathological MR-signals indicating bone metastases. **(3A)** PET/CT fusion, **(3B)** CT without contrast medium, **(3C)** PET/MRI fusion, **(3D)** MRI (contrast-enhanced T1w and fat saturation). *With kind permission of the European Journal of Nuclear Medicine and Molecular Imaging.*

6 Han M, Partin AW, Pound CR, Epstein JI, Walsh PC. Long-term biochemical disease-free and cancer-specific survival following anatomic radical retropubic prostatectomy. The 15-year Johns Hopkins experience. Urol. Clin. North Am. 2001;28:555–65.

7 Sandler HM, Eisenberger MA. Assessing and Treating Patients With Increasing Prostate Specific Antigen Following Radical Prostatectomy. J. Urol. 2007;178:S20–4.

8 Eder M, Schäfer M, Bauder-Wüst U, Hull W-E, Wängler C, Mier W, et al. 68Ga-Complex Lipophilicity and the Targeting Property of a Urea-Based PSMA Inhibitor for PET Imaging. Bioconjug. Chem. 2012;23:688–97.

9 Schäfer M, Bauder-Wüst U, Leotta K, Zoller F, Mier W, Haberkorn U, et al. A dimerized urea-based inhibitor of the prostate-specific membrane antigen for 68Ga-PET imaging of prostate cancer. EJNMMI Res. 2012;2:23.

10 Afshar-Oromieh A, Haberkorn U, Schlemmer HP, Fenchel M, Eder M, Eisenhut M, et al. Comparison of PET/CT and PET/MRI hybrid systems using a 68Ga-labelled PSMA ligand for the diagnosis of recurrent prostate cancer: initial experience. Eur. J. Nucl. Med. Mol. Imaging. 2014;41:887–97.

11 Afshar-Oromieh A, Malcher A, Eder M, Eisenhut M, Linhart HG, Hadaschik BA, et al. PET imaging with a [68Ga]gallium-labelled PSMA ligand for the diagnosis of prostate cancer: biodistribution in humans and first evaluation of tumor lesions. Eur. J. Nucl. Med. Mol. Imaging. 2013;40:486–95.

12 Afshar-Oromieh A, Avtzi E, Giesel FL, Holland-Letz T, Linhart HG, Eder M, et al. The diagnostic value of PET/CT imaging with the 68Ga-labelled PSMA ligand HBED-CC in the diagnosis of recurrent prostate cancer. Eur. J. Nucl. Med. Mol. Imaging. 2014;1–13.

13 Afshar-Oromieh A, Zechmann CM, Malcher A, Eder M, Eisenhut M, Linhart HG, et al. Comparison of PET imaging with a 68Ga-labelled PSMA ligand and 18F-choline-based PET/CT for the diagnosis of recurrent prostate cancer. Eur. J. Nucl. Med. Mol. Imaging. 2014;41:11–20.

14 Eiber M, Maurer T, Souvatzoglou M, Beer AJ, Ruffani A, Haller B, et al. Evaluation of hybrid 68Ga-PSMA-ligand PET/CT in 248 patients with biochemical recurrence after radical prostatectomy. J. Nucl. Med. 2015;jnumed.115.154153.

15 Baco E, Ukimura O, Rud E, Vlatkovic L, Svindland A, Aron M, et al. Magnetic Resonance Imaging–Transectal Ultrasound Image-fusion Biopsies Accurately Characterize the Index Tumor: Correlation with Step-sectioned Radical Prostatectomy Specimens in 135 Patients. Eur. Urol. 2015;67:787–94.

16 Siddiqui M, Rais-Bahrami S, Turkbey B, et al. COmparison of mr/ultrasound fusion–guided biopsy with ultrasound-guided biopsy for the diagnosis of prostate cancer. JAMA. 2015;313:390–7.

Contact

Ali Afshar-Oromieh, M.D.
Heidelberg University Hospital
Department of Nuclear Medicine

INF 400
69120 Heidelberg
Germany
Phone: +49-6221-56-7732
Fax: +49-6221-42-2462
ali.afshar@med.uni-heidelberg.de

HIGHLIGHTS OF PRESCRIBING INFORMATION

These highlights do not include all the information needed to use Fludeoxyglucose F 18 Injection safely and effec-tively. See full prescribing information for Fludeoxyglucose F 18 Injection. Fludeoxyglucose F 18 Injection, USP For intravenous use Initial U.S. Approval: 2005

RECENT MAJOR CHANGES

Warnings and Precautions (5.1, 5.2)	7/2010
Adverse Reactions (6)	7/2010

INDICATIONS AND USAGE

Fludeoxyglucose F18 Injection is indicated for positron emission tomography (PET) imaging in the following settings:

- Oncology: For assessment of abnormal glucose metabolism to assist in the evaluation of malignancy in patients with known or suspected abnormalities found by other testing modalities, or in patients with an existing diagnosis of cancer.
- Cardiology: For the identification of left ventricular myocardium with residual glucose metabolism and reversible loss of systolic function in patients with coronary artery disease and left ventricular dysfunction, when used together with myocardial perfusion imaging.
- Neurology: For the identification of regions of abnormal glucose metabolism associated with foci of epileptic seizures (1).

DOSAGE AND ADMINISTRATION

Fludeoxyglucose F 18 Injection emits radiation. Use procedures to minimize radiation exposure. Screen for blood glucose abnormalities.

- In the oncology and neurology settings, instruct patients to fast for 4 to 6 hours prior to the drug's injection. Consider medical therapy and laboratory testing to assure at least two days of normoglycemia prior to the drug's administration (5.2).
- In the cardiology setting, administration of glucose-containing food or liquids (e.g., 50 to 75 grams) prior to the drug's injection facilitates localization of cardiac ischemia (2.3).

Aseptically withdraw Fludeoxyglucose F 18 Injection from its container and administer by intravenous injection (2).

The recommended dose:

- for adults is 5 to 10 mCi (185 to 370 MBq), in all indicated clinical settings (2.1).
- for pediatric patients is 2.6 mCi in the neurology setting (2.2).

Initiate imaging within 40 minutes following drug injection; acquire static emission images 30 to 100 minutes from time of injection (2).

DOSAGE FORMS AND STRENGTHS

Multi-dose 30mL and 50mL glass vial containing 0.74 to 7.40 GBq/mL (20 to 200 mCi/mL) Fludeoxyglucose F 18 Injection and 4.5mg of sodium chloride with 0.1 to 0.5% w/w ethanol as a stabilizer (approximately 15 to 50 mL volume) for intravenous administration (3).

CONTRAINDICATIONS

None

WARNINGS AND PRECAUTIONS

- Radiation risks: use smallest dose necessary for imaging (5.1).
- Blood glucose adnormalities: may cause suboptimal imaging (5.2).

ADVERSE REACTIONS

Hypersensitivity reactions have occurred; have emergency resuscitation equipment and personnel immediately available (6). **To report SUSPECTED ADVERSE REACTIONS, contact PETNET Solutions, Inc. at 877-473-8638 or FDA at 1-800-FDA-1088 or www.fda.gov/medwatch.**

USE IN SPECIFIC POPULATIONS

Pregnancy Category C: No human or animal data. Consider alternative diagnostics; use only if clearly needed (8.1).

- Nursing mothers: Use alternatives to breast feeding (e.g., stored breast milk or infant formula) for at least 10 half-lives of radioactive decay, if Fludeoxyglucose F 18 Injection is administered to a woman who is breast-feeding (8.3).
- Pediatric Use: Safety and effectiveness in pediatric patients have not been established in the oncology and cardiology settings (8.4).

See 17 for PATIENT COUNSELING INFORMATION

Revised: 1/2011

FULL PRESCRIBING INFORMATION: CONTENTS*

*Sections or subsections omitted from the full prescribing information are not listed

FULL PRESCRIBING INFORMATION

1 INDICATIONS AND USAGE

Fludeoxyglucose F 18 Injection is indicated for positron emission tomography (PET) imaging in the following settings:

1.1 Oncology

For assessment of abnormal glucose metabolism to assist in the evaluation of malignancy in patients with known or suspected abnormalities found by other testing modalities, or in patients with an existing diagnosis of cancer.

1.2 Cardiology

For the identification of left ventricular myocardium with residual glucose metabolism and reversible loss of systolic function in patients with coronary artery disease and left ventricular dysfunction, when used together with myocardial perfusion imaging.

1.3 Neurology

For the identification of regions of abnormal glucose metabolism associated with foci of epileptic seizures.

2 DOSAGE AND ADMINISTRATION

Fludeoxyglucose F 18 Injection emits radiation. Use procedures to minimize radiation exposure. Calculate the final dose from the end of synthesis (EOS) time using proper radioactive decay factors. Assay the final dose in a properly calibrated dose calibrator before administration to the patient [see Description (11.2)].

2.1 Recommended Dose for Adults

Within the oncology, cardiology and neurology settings, the recommended dose for adults is 5 to 10 mCi (185 to 370 MBq) as an intravenous injection.

2.2 Recommended Dose for Pediatric Patients

Within the neurology setting, the recommended dose for pediatric patients is 2.6 mCi, as an intravenous injection. The optimal dose adjustment on the basis of body size or weight has not been determined [see Use in Special Populations (8.4)].

2.3 Patient Preparation

- To minimize the radiation absorbed dose to the bladder, encourage adequate hydration. Encourage the patient to drink water or other fluids (as tolerated) in the 4 hours before their PET study.
- Encourage the patient to void as soon as the imaging study is completed and as often as possible thereafter for at least one hour.
- Screen patients for clinically significant blood glucose abnormalities by obtaining a history and/or laboratory tests [see Warnings and Precautions (5.2)]. Prior to Fludeoxyglucose F 18 PET imaging in the oncology and neurology settings, instruct patient to fast for 4 to 6 hours prior to the drug's injection.
- In the cardiology setting, administration of glucose-containing food or liquids (e.g., 50 to 75 grams) prior to Fludeoxyglucose F18 Injection facilitates localization of cardiac ischemia

2.4 Radiation Dosimetry

The estimated human absorbed radiation doses (rem/mCi) to a newborn (3.4 kg), 1-year old (9.8 kg), 5-year old (19 kg), 10-year old (32 kg), 15-year old (57 kg), and adult (70 kg) from intravenous administration of Fludeoxyglucose F 18 Injection are shown in Table 1. These estimates were calculated based on human[2] data and using the data published by the International Commission on Radiological Protection[4] for Fludeoxyglucose ^{18}F. The dosimetry data show that there are slight variations in absorbed radiation dose for various organs in each of the age groups. These dissimilarities in absorbed radiation dose are due to developmental age variations (e.g., organ size, location, and overall metabolic rate for each age group). The identified critical organs (in descending order) across all age groups evaluated are the urinary bladder, heart, pancreas, spleen, and lungs.

Table 1. Estimated Absorbed Radiation Doses (rem/mCi) After Intravenous Administration of Fludeoxyglucose F-18 Injection[a]

Organ	Newborn	1-year old	5-year old	10-year old	15-year old	Adult
	(3.4 kg)	(9.8 kg)	(19 kg)	(32 kg)	(57 kg)	(70 kg)
Bladder wall[b]	4.3	1.7	0.93	0.60	0.40	0.32
Heart wall	2.4	1.2	0.70	0.44	0.29	0.22
Pancreas	2.2	0.68	0.33	0.25	0.13	0.096
Spleen	2.2	0.84	0.46	0.29	0.19	0.14
Lungs	0.96	0.38	0.20	0.13	0.092	0.064
Kidneys	0.81	0.34	0.19	0.13	0.089	0.074
Ovaries	0.80	0.8	0.19	0.11	0.058	0.053
Uterus	0.79	0.35	0.19	0.12	0.076	0.062
LLI wall *	0.69	0.28	0.15	0.097	0.060	0.051
Liver	0.69	0.31	0.17	0.11	0.076	0.058
Gallbladder wall	0.69	0.26	0.14	0.093	0.059	0.049
Small intestine	0.68	0.29	0.15	0.096	0.060	0.047
ULI wall **	0.67	0.27	0.15	0.090	0.057	0.046
Stomach wall	0.65	0.27	0.14	0.089	0.057	0.047
Adrenals	0.65	0.28	0.15	0.095	0.061	0.048
Testes	0.64	0.27	0.14	0.085	0.052	0.041
Red marrow	0.62	0.26	0.14	0.089	0.057	0.047
Thymus	0.61	0.26	0.14	0.086	0.056	0.044
Thyroid	0.61	0.26	0.13	0.080	0.049	0.039
Muscle	0.58	0.25	0.13	0.078	0.049	0.039
Bone surface	0.57	0.24	0.12	0.079	0.052	0.041
Breast	0.54	0.22	0.11	0.068	0.043	0.034
Skin	0.49	0.20	0.10	0.060	0.037	0.030
Brain	0.29	0.13	0.09	0.078	0.072	0.070
Other tissues	0.59	0.25	0.13	0.083	0.052	0.042

[a] MIRDOSE 2 software was used to calculate the radiation absorbed dose. Assumptions on the biodistribution based on data from Gallagher et al.1 and Jones et al.2

[b] The dynamic bladder model with a uniform voiding frequency of 1.5 hours was used. *LLI = lower large intestine; **ULI = upper large intestine

2.5 Radiation Safety – Drug Handling

- Use waterproof gloves, effective radiation shielding, and appropriate safety measures when handling Fludeoxyglucose F 18 Injection to avoid unnecessary radiation exposure to the patient, occupational workers, clinical personnel and other persons.
- Radiopharmaceuticals should be used by or under the control of physicians who are qualified by specific training and experience in the safe use and handling of radionuclides, and whose experience and training have been approved by the appropriate governmental agency authorized to license the use of radionuclides.
- Calculate the final dose from the end of synthesis (EOS) time using proper radioactive decay factors. Assay the final dose in a properly calibrated dose calibrator before administration to the patient [see Description (11.2)].
- The dose of Fludeoxyglucose F 18 used in a given patient should be minimized consistent with the objectives of the procedure, and the nature of the radiation detection devices employed.

2.6 Drug Preparation and Administration

- Calculate the necessary volume to administer based on calibration time and dose.
- Aseptically withdraw Fludeoxyglucose F 18 Injection from its container.
- Inspect Fludeoxyglucose F 18 Injection visually for particulate matter and discoloration before administration, whenever solution and container permit.
- Do not administer the drug if it contains particulate matter or discoloration; dispose of these unacceptable or unused preparations in a safe manner, in compliance with applicable regulations.
- Use Fludeoxyglucose F 18 Injection within 12 hours from the EOS.

2.7 Imaging Guidelines

- Initiate imaging within 40 minutes following Fludeoxyglucose F 18 Injection administration.
- Acquire static emission images 30 to 100 minutes from the time of injection.

3 DOSAGE FORMS AND STRENGTHS

Multiple-dose 30 mL and 50 mL glass vial containing 0.74 to 7.40 GBq/mL (20 to 200 mCi/mL) of Fludeoxyglucose F 18 Injection and 4.5 mg of sodium chloride with 0.1 to 0.5% w/w ethanol as a stabilizer (approximately 15 to 50 mL volume) for intravenous administration.

4 CONTRAINDICATIONS

None

5 WARNINGS AND PRECAUTIONS

5.1 Radiation Risks

Radiation-emitting products, including Fludeoxyglucose F 18 Injection, may increase the risk for cancer, especially in pediatric patients. Use the smallest dose necessary for imaging and ensure safe handling to protect the patient and health care worker [see Dosage and Administration (2.5)].

5.2 Blood Glucose Abnormalities

In the oncology and neurology setting, suboptimal imaging may occur in patients with inadequately regulated blood glucose levels. In these patients, consider medical therapy and laboratory testing to assure at least two days of normoglycemia prior to Fludeoxyglucose F 18 Injection administration.

6 ADVERSE REACTIONS

Hypersensitivity reactions with pruritus, edema and rash have been reported in the post-marketing setting. Have emergency resuscitation equipment and personnel immediately available.

7 DRUG INTERACTIONS

The possibility of interactions of Fludeoxyglucose F 18 Injection with other drugs taken by patients undergoing PET imaging has not been studied.

8 USE IN SPECIFIC POPULATIONS

8.1 Pregnancy

Pregnancy Category C Animal reproduction studies have not been conducted with Fludeoxyglucose F 18 Injection. It is also not known whether Fludeoxyglucose F 18 Injection can cause fetal harm when administered to a pregnant woman or can affect reproduction capacity. Consider alternative diagnostic tests in a pregnant woman; administer Fludeoxyglucose F 18 Injection only if clearly needed.

8.3 Nursing Mothers

It is not known whether Fludeoxyglucose F 18 Injection is excreted in human milk. Consider alternative diagnostic tests in women who are breast-feeding. Use alternatives to breast feeding (e.g., stored breast milk or infant formula) for at least 10 half-lives of radioactive decay, if Fludeoxyglucose F 18 Injection is administered to a woman who is breast-feeding.

8.4 Pediatric Use

The safety and effectiveness of Fludeoxyglucose F 18 Injection in pediatric patients with epilepsy is established on the basis of studies in adult and pediatric patients. In pediatric patients with epilepsy, the recommended dose is 2.6 mCi. The optimal dose adjustment on the basis of body size or weight has not been determined. In the oncology or cardiology settings, the safety and effectiveness of Fludeoxyglucose F 18 Injection have not been established in pediatric patients.

11 DESCRIPTION

11.1 Chemical Characteristics

Fludeoxyglucose F 18 Injection is a positron emitting radiopharmaceutical that is used for diagnostic purposes in conjunction with positron emission tomography (PET) imaging. The active ingredient 2-deoxy-2-[^{18}F]fluoro-D-glucose has the molecular formula of $C_6H_{11}{}^{18}FO_5$ with a molecular weight of 181.26, and has the following chemical structure:

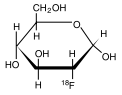

Fludeoxyglucose F 18 Injection is provided as a ready to use sterile, pyrogen free, clear, colorless solution. Each mL contains between 0.740 to 7.40GBq (20.0 to 200 mCi) of 2-deoxy-2-[^{18}F]fluoro-D-glucose at the EOS, 4.5 mg of sodium chloride and 0.1 to 0.5% w/w ethanol as a stabilizer. The pH of the solution is between 4.5 and 7.5. The solution is packaged in a multiple-dose glass vial and does not contain any preservative.

11.2 Physical Characteristics

Fluorine F 18 decays by emitting positron to Oxygen O 16 (stable) and has a physical half-life of 109.7 minutes. The principal photons useful for imaging are the dual 511 keV gamma photons, that are produced and emitted simultaneously in opposite direction when the positron interacts with an electron (Table 2).

Table 2. Pricipal Radiation Emission Data for Fluorine F18

Radiation/Emission	% Per Disintegration	Mean Energy
Positron (b+)	96.73	249.8 keV
Gamma (±)*	193.46	511.0 keV

*Produced by positron annihilation

From: Kocher, D.C. Radioactive Decay Tables DOE/TIC-I 1026, 89 (1981)
The specific gamma ray constant (point source air kerma coefficient) for fluorine F 18 is 5.7 R/hr/mCi (1.35 x 10-6 Gy/hr/kBq) at 1 cm. The half-value layer (HVL) for the 511 keV photons is 4 mm lead (Pb). The range of attenuation coefficients for this radionuclide as a function of lead shield thickness is shown in Table 3. For example, the interposition of an 8 mm thickness of Pb, with a coefficient of attenuation of 0.25, will decrease the external radiation by 75%.

Table 3. Radiation Attenuation of 511 keV Photons by lead (Pb) shielding	
Shield thickness (Pb) mm	Coefficient of attenuation
0	0.00
4	0.50
8	0.25
13	0.10
26	0.01
39	0.001
52	0.0001

For use in correcting for physical decay of this radionuclide, the fractions remaining at selected intervals after calibration are shown in Table 4.

Table 4. Physical Decay Chart for Fluorine F18	
Minutes	Fraction Remaining
0*	1.000
15	0.909
30	0.826
60	0.683
110	0.500
220	0.250

*calibration time

12 CLINICAL PHARMACOLOGY

12.1Mechanism of Action

Fludeoxyglucose F 18 is a glucose analog that concentrates in cells that rely upon glucose as an energy source, or in cells whose dependence on glucose increases under pathophysiological conditions. Fludeoxyglucose F 18 is transported through the cell membrane by facilitative glucose transporter proteins and is phosphorylated within the cell to [18F] FDG-6-phosphate by the enzyme hexokinase. Once phosphorylated it cannot exit until it is dephosphorylated by glucose-6-phosphatase. Therefore, within a given tissue or pathophysiological process, the retention and clearance of Fludeoxyglucose F 18 reflect a balance involving glucose transporter, hexokinase and glucose-6-phosphatase activities. When allowance is made for the kinetic differences between glucose and Fludeoxyglucose F 18 transport and phosphorylation (expressed as the ,'lumped constant" ratio), Fludeoxyglucose F 18 is used to assess glucose metabolism. In comparison to background activity of the specific organ or tissue type, regions of decreased or absent uptake of Fludeoxyglucose F 18 reflect the decrease or absence of glucose metabolism. Regions of increased uptake of Fludeoxyglucose F 18 reflect greater than normal rates of glucose metabolism.

12.2Pharmacodynamics

Fludeoxyglucose F 18 Injection is rapidly distributed to all organs of the body after intravenous administration. After background clearance of Fludeoxyglucose F 18 Injection, optimal PET imaging is generally achieved between 30 to 40 minutes after administration.

In cancer, the cells are generally characterized by enhanced glucose metabolism partially due to (1) an increase in activity of glucose transporters, (2) an increased rate of phosphorylation activity, (3) a reduction of phosphatase activity or, (4) a dynamic alteration in the balance among all these processes. However, glucose metabolism of cancer as reflected by Fludeoxyglucose F 18 accumulation shows considerable variability. Depending on tumor type, stage, and location, Fludeoxyglucose F 18 accumulation may be increased, normal, or decreased. Also, inflammatory cells can have the same variability of uptake of Fludeoxyglucose F 18.

In the heart, under normal aerobic conditions, the myocardium meets the bulk of its energy requirements by oxidizing free fatty acids. Most of the exogenous glucose taken up by the myocyte is converted into glycogen. However, under ischemic conditions, the oxidation of free fatty acids decreases, exogenous glucose becomes the preferred myocardial sub strate, glycolysis is stimulated, and glucose taken up by the myocyte is metabolized immediately instead of being converted into glycogen. Under these conditions, phosphorylated Fludeoxyglucose F 18 accumulates in the myocyte and can be detected with PET imaging.

In the brain, cells normally rely on aerobic metabolism. In epilepsy, the glucose metabolism varies. Generally, during a seizure, glucose metabolism increases. Interictally, the seizure focus tends to be hypometabolic.

12.3 Pharmacokinetics

Distribution: In four healthy male volunteers, receiving an intravenous administration of 30 seconds in duration, the arterial blood level profile for Fludeoxyglucose F 18 decayed triexponentially. The effective half-life ranges of the three phases were 0.2 to 0.3 minutes, 10 to 13 minutes with a mean and standard deviation (STD) of 11.6 (±) 1.1 min, and 80 to 95 minutes with a mean and STD of 88 (±) 4 min. Plasma protein binding of Fludeoxyglucose F 18 has not been studied.

Metabolism: Fludeoxyglucose F 18 is transported into cells and phosphorylated to [^{18}F]-FDG-6- phosphate at a rate proportional to the rate of glucose utilization within that tissue. [F18]-FDG-6-phosphate presumably is metabolized to 2-deoxy-2-[F18]fluoro-6-phospho-D-mannose([F 18]FDM-6-phosphate). Fludeoxyglucose F 18 Injection may contain several impurities (e.g., 2-deoxy-2-chloro-D-glucose (ClDG)). Biodistribution and metabolism of ClDG are presumed to be similar to Fludeoxyglucose F 18 and would be expected to result in intracellular formation of 2-deoxy-2-chloro-6-phospho-D-glucose (ClDG-6-phosphate) and 2-deoxy-2-chloro-6-phospho-D-mannose (ClDM-6-phosphate). The phosphorylated deoxyglucose compounds are dephosphorylated and the resulting compounds (FDG, FDM, ClDG, and ClDM) presumably leave cells by passive diffusion. Fludeoxyglucose F 18 and related compounds are cleared from non-cardiac tissues within 3 to 24 hours after administration. Clearance from the cardiac tissue may require more than 96 hours. Fludeoxyglucose F 18 that is not involved in glucose metabolism in any tissue is then excreted in the urine.

Elimination: Fludeoxyglucose F 18 is cleared from most tissues within 24 hours and can be eliminated from the body unchanged in the urine. Three elimination phases have been identified in the reviewed literature. Within 33 minutes, a mean of 3.9% of the administrated radioactive dose was measured in the urine. The amount of radiation exposure of the urinary bladder at two hours post-administration suggests that 20.6% (mean) of the radioactive dose was present in the bladder.

Special Populations:

The pharmacokinetics of Fludeoxyglucose F 18 Injection have not been studied in renally-impaired, hepatically impaired or pediatric patients. Fludeoxyglucose F 18 is eliminated through the renal system. Avoid excessive radiation exposure to this organ system and adjacent tissues.

The effects of fasting, varying blood sugar levels, conditions of glucose intolerance, and diabetes mellitus on Fludeoxyglucose F 18 distribution in humans have not been ascertained [see Warnings and Precautions (5.2)].

13 NONCLINICAL TOXICOLOGY

13.1Carcinogenesis, Mutagenesis, Impairment of Fertility

Animal studies have not been performed to evaluate the Fludeoxyglucose F 18 Injection carcinogenic potential, mutagenic potential or effects on fertility.

14 CLINICAL STUDIES

14.1Oncology

The efficacy of Fludeoxyglucose F 18 Injection in positron emission tomography cancer imaging was demonstrated in 16 independent studies. These studies prospectively evaluated the use of Fludeoxyglucose F 18 in patients with suspected or known malignancies, including non-small cell lung cancer, colo-rectal, pancreatic, breast, thyroid, melanoma, Hodgkin's and non-Hodgkin's lymphoma, and various types of metastatic cancers to lung, liver, bone, and axillary nodes. All these studies had at least 50 patients and used pathology as a standard of truth. The Fludeoxyglucose F 18 Injection doses in the studies ranged from 200 MBq to 740 MBq with a median and mean dose of 370 MBq.

In the studies, the diagnostic performance of Fludeoxyglucose F 18 Injection varied with the type of cancer, size of cancer, and other clinical conditions. False negative and false positive scans were observed. Negative Fludeoxyglucose F 18 Injection PET scans do not exclude the diagnosis of cancer. Positive Fludeoxyglucose F 18 Injection PET scans can not replace pathology to establish a diagnosis of cancer. Non-malignant conditions such as fungal infections, inflammatory processes and benign tumors have patterns of increased glucose metabolism that may give rise to false-positive scans. The efficacy of Fludeoxyglucose F 18 Injection PET imaging in cancer screening was not studied.

14.2Cardiology

The efficacy of Fludeoxyglucose F 18 Injection for cardiac use was demonstrated in ten independent, prospective studies of patients with coronary artery disease and chronic left ventricular systolic dysfunction who were scheduled to undergo coronary revascularization. Before revascularization, patients underwent PET imaging with Fludeoxyglucose F 18 Injection (74 to 370 MBq, 2 to 10 mCi) and perfusion imaging with other diagnostic radiopharmaceuticals. Doses of Fludeoxyglucose F 18 Injection ranged from 74 to 370 MBq (2 to 10 mCi). Segmental, left ventricular, wall-motion assessments of asynergic areas made before revascularization were compared in a blinded manner to assessments

made after successful revascularization to identify myocardial segments with functional recovery.

Left ventricular myocardial segments were predicted to have reversible loss of systolic function if they showed Fludeoxyglucose F 18 accumulation and reduced perfusion (i.e., flow-metabolism mismatch). Conversely, myocardial segments were predicted to have irreversible loss of systolic function if they showed reductions in both Fludeoxyglucose

F 18 accumulation and perfusion (i.e., matched defects).

Findings of flow-metabolism mismatch in a myocardial segment may suggest that successful revascularization will restore myocardial function in that segment. However, false-positive tests occur regularly, and the decision to have a patient undergo revascularization should not be based on PET findings alone. Similarly, findings of a matched defect in a myocardial segment may suggest that myocardial function will not recover in that segment, even if it is successfully revascularized. However, false-negative tests occur regularly, and the decision to recommend against coronary revascularization, or to recommend a cardiac transplant, should not be based on PET findings alone. The reversibility of segmental dysfunction as predicted with Fludeoxyglucose F 18 PET imaging depends on successful coronary revascularization. Therefore, in patients with a low likelihood of successful revascularization, the diagnostic usefulness of PET imaging with Fludeoxyglucose F 18 Injection is more limited.

14.3Neurology

In a prospective, open label trial, Fludeoxyglucose F 18 Injection was evaluated in 86 patients with epilepsy. Each patient received a dose of Fludeoxyglucose F 18 Injection in the range of 185 to 370 MBq (5 to 10 mCi). The mean age was 16.4 years (range: 4 months to 58 years; of these, 42 patients were less than 12 years and 16 patients were less than 2 years old). Patients had a known diagnosis of complex partial epilepsy and were under evaluation for surgical treatment of their seizure disorder. Seizure foci had been previously identified on ictal EEGs and sphenoidal EEGs. Fludeoxyglucose F 18 Injection PET imaging confirmed previous diagnostic findings in 16% (14/87) of the patients; in 34% (30/87) of the patients, Fludeoxyglucose F 18 Injection PET images provided new findings. In 32% (27/87), imaging with Fludeoxyglucose F 18 Injection was inconclusive. The impact of these imaging findings on clinical outcomes is not known.

Several other studies comparing imaging with Fludeoxyglucose F 18 Injection results to subsphenoidal EEG, MRI and/or surgical findings supported the concept that the degree of hypometabolism corresponds to areas of confirmed epileptogenic foci. The safety and effectiveness of Fludeoxyglucose F 18 Injection to distinguish idiopathic epileptogenic foci from tumors or other brain lesions that may cause seizures have not been established.

15 REFERENCES

1. Gallagher B.M., Ansari A., Atkins H., Casella V., Christman D.R., Fowler J.S., Ido T., MacGregor R.R., Som P., Wan C.N., Wolf A.P., Kuhl D.E., and Reivich M. "Radiopharmaceuticals XXVII. 18F-labeled 2-deoxy-2-fluoro-d-glucose as a radiopharmaceutical for measuring regional myocardial glucose metabolism in vivo: tissue distribution and imaging studies in animals," J Nucl Med, 1977; 18, 990-6.
2. Jones S.C., Alavi, A., Christman D., Montanez, I., Wolf, A.P., and Reivich M. "The radiation dosimetry of 2 [F-18] fluoro-2-deoxy-D-glucose in man," J Nucl Med, 1982; 23, 613-617.
3. Kocher, D.C. "Radioactive Decay Tables: A handbook of decay data for application to radiation dosimetry and radiological assessments," 1981, DOE/TIC-I 1026, 89.
4. ICRP Publication 53, Volume 18, No. l-4,1987, pages 75-76.

16 HOW SUPPLIED/STORAGE AND DRUG HANDLING

Fludeoxyglucose F 18 Injection is supplied in a multi-dose, capped 30 mL and 50 mL glass vial containing between 0.740 to 7.40 GBq/mL (20 to 200 mCi/mL), of no carrier added 2-deoxy-2-[F 18] fluoro-D-glucose, at end of synthesis, in approximately 15 to 50 mL. The contents of each vial are sterile, pyrogen-free and preservative-free. NDC 40028-511-30; 40028-511-50

Receipt, transfer, handling, possession, or use of this product is subject to the radioactive material regulations and licensing requirements of the U.S. Nuclear Regulatory Commission, Agreement States or Licensing States as appropriate.

Store the Fludeoxyglucose F 18 Injection vial upright in a lead shielded container at 25°C (77°F); excursions permitted to 15-30°C (59-86°F).

Store and dispose of Fludeoxyglucose F 18 Injection in accordance with the regulations and a general license, or its equivalent, of an Agreement State or a Licensing State. The expiration date and time are provided on the container label. Use Fludeoxyglucose F 18 Injection within 12 hours from the EOS time.

17 PATIENT COUNSELING INFORMATION

Instruct patients in procedures that increase renal clearance of radioactivity. Encourage patients to:

- drink water or other fluids (as tolerated) in the 4 hours before their PET study.
- void as soon as the imaging study is completed and as often as possible thereafter for at least one hour.

Manufactured by: PETNET Solutions Inc.
810 Innovation Drive
Knoxville, TN 37932

Distributed by: PETNET Solutions Inc.
810 Innovation Drive
Knoxville, TN 37932

PETNET Solutions

PN0002262 Rev. A

March 1, 2011

Indications

Fludeoxyglucose F^{18} Injection is indicated for positron emission tomography (PET) imaging in the following settings:

- **Oncology:** For assessment of abnormal glucose metabolism to assist in the evaluation of malignancy in patients with known or suspected abnormalities found by other testing modalities, or in patients with an existing diagnosis of cancer.
- **Cardiology:** For the identification of left ventricular myocardium with residual glucose metabolism and reversible loss of systolic function in patients with coronary artery disease and left ventricular dysfunction, when used together with myocardial perfusion imaging.
- **Neurology:** For the identification of regions of abnormal glucose metabolism associated with foci of epileptic seizures.

Important Safety Information

- **Radiation Risks:** Radiationemitting products, including Fludeoxyglucose F^{18} Injection, may increase the risk for cancer, especially in pediatric patients. Use the smallest dose necessary for imaging and ensure safe handling to protect the patient and healthcare worker.
- **Blood Glucose Abnormalities:** In the oncology and neurology setting, suboptimal imaging may occur in patients with inadequately regulated blood glucose levels. In these patients, consider medical therapy and laboratory testing to assure at least two days of normoglycemia prior to Fludeoxyglucose F^{18} Injection administration.
- **Adverse Reactions:** Hypersensitivity reactions with pruritus, edema and rash have been reported; have emergency resuscitation equipment and personnel immediately available.

Metastatic Prostate Cancer in Practice – the MET-RADS-P Imaging Response System Using Whole-body MRI

Anwar R. Padhani[1]; Nina Tunariu[2]

[1] Paul Strickland Scanner Centre, Mount Vernon Hospital, Northwood, Middlesex, UK
[2] Royal Marsden NHS Foundation Trust & Institute of Cancer Research and Cancer Research UK Cancer Imaging Centre, Sutton, Surrey, UK

Introduction

Whole-body MRI (WB-MRI) is an increasingly used, radiation-free imaging method for assessing bone and soft tissue pathology, and for evaluating response to therapy [1]. WB-MRI has been developed to overcome the limitations of Bone Scintigraphy (BS) and Computed Tomography (CT) for detection and therapeutic response assessments in bone metastases [2]. Although increasingly used and recommended by international guidelines for multiple myeloma [3], WB-MRI usage has been confined mainly to expert centers, causing some concerns about its broader applicability. While WB-MRI can be performed on almost all modern MRI scanners, inconsistencies in WB-MRI acquisition protocols and reporting standards have prevented its widespread testing and implementation, beyond the indication for multiple myeloma.

Recently, a group of oncologic imaging specialists teamed with a leading urologist and oncologist, to develop recommendations on the minimum requirements for WB-MRI acquisition protocol as well as standardized reporting guidelines. They recognized that for this promising method to become mainstream it is vital to enforce some uniformity in acquisition, interpretation, and reporting. The authors have named their formulation for metastatic disease response and diagnostic system for prostate cancer as MET-RADS-P (METastasis Reporting And Data System for Prostate cancer) [4].

Why MET-RADS is needed

BS/CT scans are widely used and endorsed by international guidelines as the standard imaging investigations in the staging and follow-up of metastatic prostate cancer, thereby affecting patient management [5, 6]. However, it is increasing clear that currently used imaging methods are limited in their effectiveness in directing therapy and may no longer be relevant in the era of high-precision medicine, where an increasing number of cytostatic and novel therapies are becoming available [2]. For example, the accepted minimum lymph node diameter (10 mm – short axis) on CT scan as measure of involvement is only modestly correlated with the presence of malignant disease, and CT cannot accurately evaluate the presence or the therapeutic response in bone metastases, the commonest metastatic site in prostate cancer. Conversely, increased BS uptake in number and extent of lesions can equally occur with the osteoblastic healing (FLARE reaction) associated with tumor response and with the osteoblastic progression associated with tumor burden increase, thus creating confusion between response and progression, when response to therapy is being assessed. Next generation whole-body imaging tools such as PET with targeted tracers and WB-MRI with diffusion-weighted sequences are emerging as powerful alternatives; however, the challenge remains in validating these newer imaging approaches, so that their use can be justified in the clinical routine.

An important step in this process is to ensure uniformity in the acquisition, interpretation, and reporting of next generation whole-body imaging methods, so that multicenter trials leading to validation of these methods can be more easily performed and evaluated. An important step for WB-MRI is the new MET-RADS-P standard for use in patients with advanced prostate cancer [4]. The standard establishes minimum acceptable technical parameters for imaging acquisitions built with sequences already available on most modern scanners. Of the sequences recommended, it is acknowledged that whole-body diffusion-weighted sequences are the most challenging to implement across imaging platforms. These sequences have been grouped to enable fast, high-quality examinations for tumor detection and response assessments (core and comprehensive protocols respectively). Image quality control and quality assurance procedures are also detailed by the standard. The MET-RADS-P standard is designed to offer day-to-day reporting guidance, paired with a detailed reporting tool that describes the disease phenotype based on anatomic patterns of metastatic spread thus, enabling systematic collection of analyzable data for research purposes.

Comprehensive response criteria for bone and soft tissue metastases and local disease have been proposed, with the ability to summarize the likelihood of a response to treatment, using a Likert-like 1–5 scale. It is important to note that the summarized likelihood of response in bone, uses newly developed MET-RADS criteria, but the response in soft-tissues continues to be based on long established

Figure 1: Updated MET-RADS-P template form and response criteria for bone and soft tissue disease.

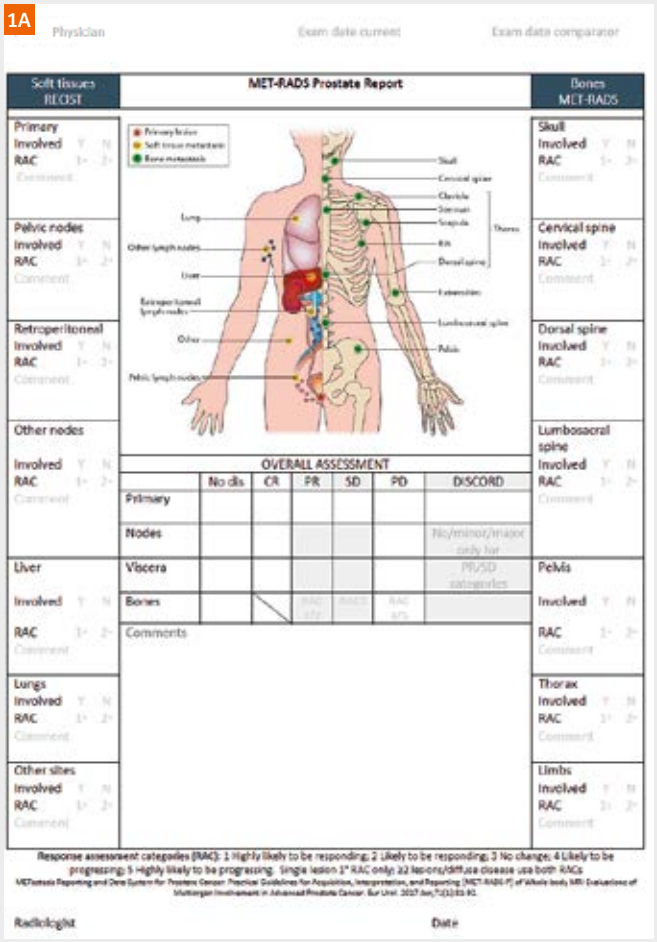

Figure 1A: Updated MET-RADS-P template form allocates the presence of unequivocal identified disease to 14 predefined regions of the body (primary disease, seven skeletal and three nodal regions, lung, liver and other soft tissue sites) at baseline and on follow-up assessments. At each anatomical location, the presence of disease is indicated (yes/no) together with the response assessment categories (primary/secondary). The overall response of the primary tumor, nodal and visceral disease are categorical (no disease (ND), complete response (CR), partial response (PR), stable disease (SD) and progressive disease (PD)). However, the overall response of bone disease is on a scale of 1–5 indicating the likely overall response category: (1) highly likely to be responding, (2) likely to be responding, (3) stable, (4) likely to be progressing and (5) highly likely to be progressing.

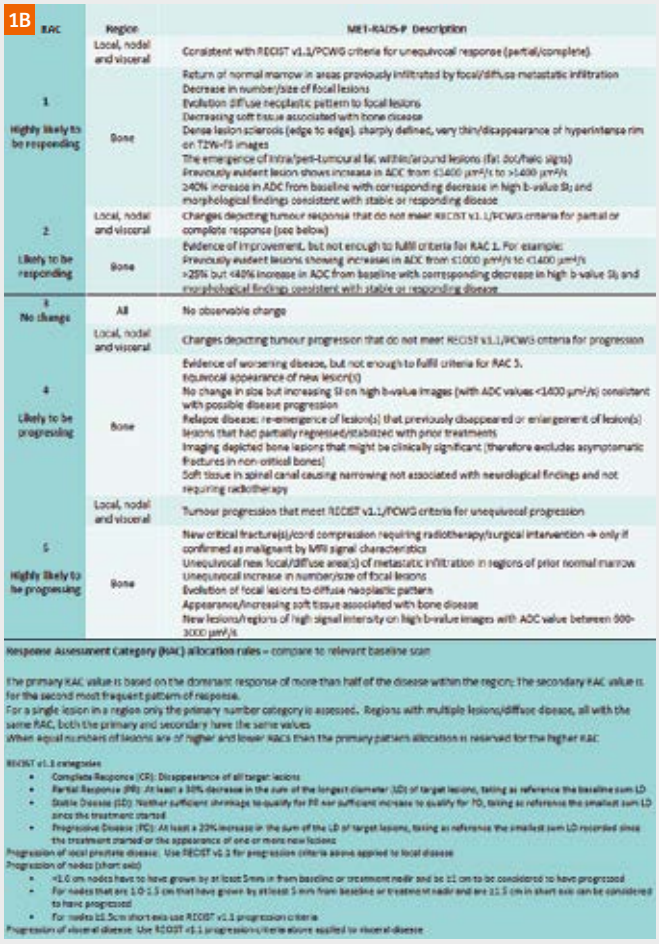

Figure 1B: Criteria for regional response assessment categories (RACs) that summarize likelihood of response in bone disease employ the newly developed MET-RADS criteria, but RACs for response in soft-tissues uses established standards already prescribed by RECIST v1.1 and PCWG guidance [7, 8]. Response assessment is indicated on a 1–5 scale indicating the likely RAC for each location, comparing to the baseline study (RAC-1, indicates highly likely to be responding, up to RAC-5, indicating highly likely to be progressing).

Figure 2: Primary resistance to hormonal therapy
67-year-old male with metastatic castrate resistant prostate cancer (mCRPC).
WB-MRI examinations before and on androgen deprivation therapy (Abiraterone and Goserelin).

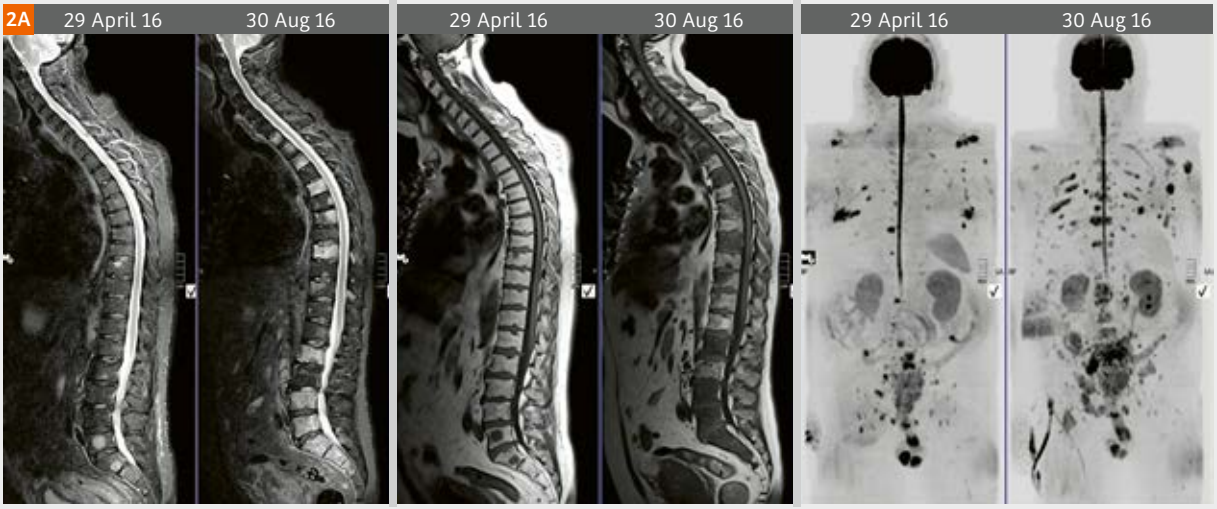

Figure 2A: Marked disease progression can be seen on morphology T1-weighted and STIR sequences and on WB b900 MIP images and confirmed by ADC measurements (see Fig. 2D also). Disease progression is seen in the prostate gland with extensive bladder invasion together with rectal invasion. There is disease progression in pelvic and retroperitoneal lymph nodes with nodal enlargement in the left axilla also. There is bone disease progression throughout the spine with extra-osseous soft tissue disease with new and enlarging deposits. No liver or lung disease is seen. The spinal stenosis at L3/l4 is degenerative in nature.

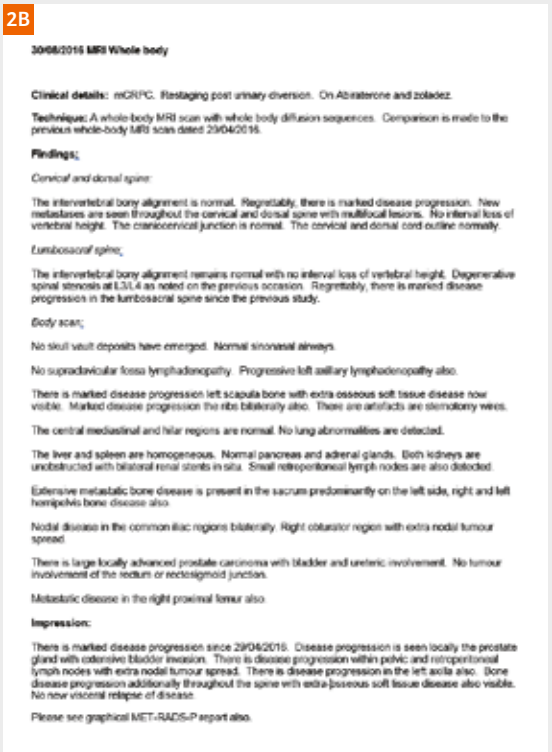
2B

30/08/2016 MRI Whole body

Clinical details: mCRPC. Restaging post urinary diversion. On Abiraterone and zoladez.

Technique: A whole-body MRI scan with whole body diffusion sequences. Comparison is made to the previous whole-body MRI scan dated 29/04/2016.

Findings:

Cervical and dorsal spine:

The intervertebral bony alignment is normal. Regrettably, there is marked disease progression. New metastases are seen throughout the cervical and dorsal spine with multifocal lesions. No interval loss of vertebral height. The craniocervical junction is normal. The cervical and dorsal cord outline normally.

Lumbosacral spine:

The intervertebral bony alignment remains normal with no interval loss of vertebral height. Degenerative spinal stenosis at L3/L4 as noted on the previous occasion. Regrettably, there is marked disease progression in the lumbosacral spine since the previous study.

Body scan:

No skull vault deposits have emerged. Normal sinonasal airways.

No supraclavicular fossa lymphadenopathy. Progressive left axillary lymphadenopathy also.

There is marked disease progression left scapula bone with extra osseous soft tissue disease now visible. Marked disease progression the ribs bilaterally also. There are artefacts are sternotomy wires.

The central mediastinal and hilar regions are normal. No lung abnormalities are detected.

The liver and spleen are homogeneous. Normal pancreas and adrenal glands. Both kidneys are unobstructed with bilateral renal stents in situ. Small retroperitoneal lymph nodes are also detected.

Extensive metastatic bone disease is present in the sacrum predominantly on the left side, right and left hemipelvis bone disease also.

Nodal disease in the common iliac regions bilaterally. Right obturator region with extra nodal tumour spread.

There is large locally advanced prostate carcinoma with bladder and ureteric involvement. No tumour involvement of the rectum or rectosigmoid junction.

Metastatic disease in the right proximal femur also.

Impression:

There is marked disease progression since 29/04/2016. Disease progression is seen locally the prostate gland with extensive bladder invasion. There is disease progression within pelvic and retroperitoneal lymph nodes with extra nodal tumour spread. There is disease progression in the left axilla also. Bone disease progression additionally throughout the spine with extra-osseous soft tissue disease also visible. No new visceral relapse of disease.

Please see graphical MET-RADS-P report also.

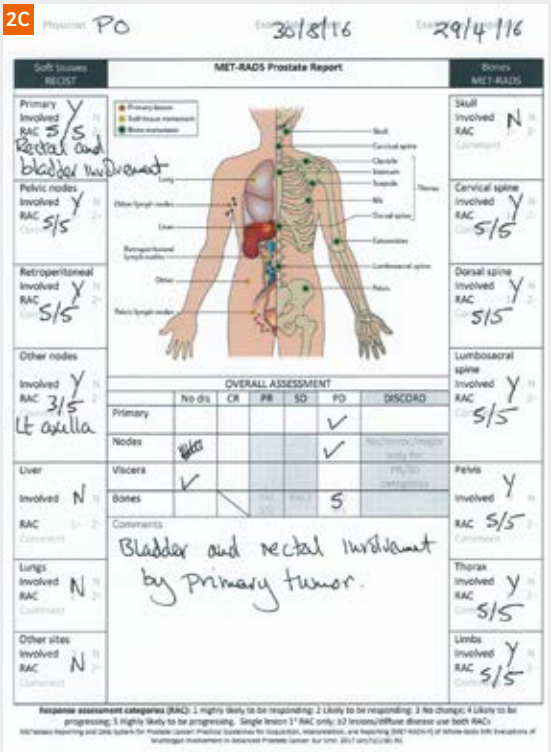

Figure 2B: Original text report for the follow-up examination that accompanies the MET-RADS-P template report.

Figure 2C: Completed MET-RADS-P template report indicating sites of disease and RACs at each anatomical location compared to the baseline study. The presence of unequivocal identified disease is indicated together with primary and secondary RACs at each site using the criteria set out in Figure 1B. Short relevant comments are included for clarification purposes where needed.

Figure 2D: WB-tumor load segmentation undertaken on *syngo*.via Frontier MR Total Tumor Load software (Siemens Healthcare; released research prototype – not part of the MET-RADS-P standard) for illustrative purposes only.

The whole-body b900 images are segmented using computed high b-value images of 1200 s/mm² and signal intensity threshold of approximately 100 AU. Extraneous signals (such as the brain, kidneys, bowel, gonads) are removed to leave only recognizable disease sites. The color the b900 MIP images are overlaid with ADC value classes using the thresholds indicated. The green voxels are values ≥1500 µm²/s (representing voxels that are 'highly likely' to be responding). The yellow voxels are set to lie between the 95th centile ADC value of the pre-treatment histogram (1295 µm²/s) and 1500 µm²/s thus representing voxels 'likely' to be responding. Red-voxels represent mostly untreated disease.

43 mL of tumor are segmented before therapy and 472 mL on therapy. Note that there is no significant global increase in ADC values (859 µm²/s and 885 µm²/s) on the corresponding absolute frequency histograms. There is also no increase in the standard deviation of the histogram (247 and 249 µm²/s). Note increased extent and volume of red-voxels consistent with disease progression (95% before therapy and 94% after therapy).

standards, prescribed by RECIST v1.1 and PCWG, the Prostate Cancer Working Group [7, 8) for clinical research. Discordant responses in which progressing and responding lesions are seen at same time point, are increasing seen with the use of targeted therapies and are a recognized manifestation of tumor heterogeneity. MET-RADS-P proposes methods to record the presence, location and extent of discordant responses between and within body parts. The use of MET-RADS-P enables for the first time to categorize bone disease response into 3 categories (progressive disease, stable disease and response), rather than the clinically recommended categories (progression/no progression) when using BS/CT scans [8], thus mirroring response assessments in soft tissues disease.

The benefits of using a standardized approach include enhanced data collection for outcomes monitoring in clinical trials and from patient registries, enhancing the education of radiologists to reduce variability in imaging interpretations, and for improving communication with referring clinicians. The MET-RADS-P authors state that the new way of response categorization from 2 categories used currently, to 3 categories when assessing bone disease response, could lead to a paradigm shift from the current concept of treating patients to documentable progression (when tumor volume could be substantially greater than baseline), to being guided by the presence or absence of benefit to therapy thus introducing more nuanced delivery of patient care.

MET-RADS-P template form

Response assessment categories (RACs)
An updated MET-RADS-P template form can be found in Figure 1 and is available as a pdf document at: www.siemens.com/magnetom-world.

The use of MET-RADS-P system starts by allocating the presence of unequivocal identified disease based on morphology and signal characteristics on all acquired images to 14 predefined regions of the body (primary disease, seven skeletal and three nodal regions, lung, liver and other soft tissue sites) at baseline and on follow-up assessments (see page 1 of the MET-RADS-P template form Figure 1A).

For follow-up studies, a response assessment on a scale of 1–5 indicating the likely response assessment category (RAC) for each location is recorded, comparing to the baseline study (RAC-1, indicating highly likely to be responding, up to RAC-5, indicating highly likely to be progressing).

The reporting guideline provides detailed explanations of the imaging criteria to be used to classify the likelihood of response in bones. Thus, RACs that summarize likelihood

of response in bone disease employ the newly developed MET-RADS criteria (Fig. 1B), but RACs for response in soft-tissues continues to use established standards already prescribed by RECIST v1.1 and PCWG guidance [7, 8].

For each region, only 2 RACs are needed to account for heterogeneity of responses that may occur in different anatomic areas. The primary RAC value (1–5) is based on dominant pattern of response within the region (that is, the response shown by more than half of the lesions within the region). A secondary RAC value (1–5) is assigned to the second most frequent pattern of response seen within the region.

A tertiary RAC value (4–5) maybe assigned to the region to illustrate progressing disease (i.e. RAC 4–5), if not already captured by the primary or secondary RAC values but this is not usually necessary in clinical practice.

When assessing a single lesion in a region, only the primary number category is used. Regions with multiple lesions all with the same pattern of response will have the same RAC value assigned as both the primary and secondary RACs. When equal numbers of lesions are category RAC 4/5 (progressing) as RAC 1/2/3 (responding & stable), then the primary pattern allocation is reserved for RAC 4/5 (the higher category). Similarly, when equal numbers of lesions are category RAC 1/2 as RAC 3, then the primary pattern allocation is reserved for RAC 3 (the higher category).

Overall response
The final response assessment consists of separately assessing the status of the primary disease, bones, nodes, and viscera without an overall patient response result. The overall patient assessment should be summarized in the text report which should accompany the MET-RADS-P template report (Figs. 2B, C).

Unlike regional response assessments which allocate RACs, the overall response for the primary tumor, nodal and visceral disease should be categorical, thus following established guidelines [7, 8], to improve communication with clinicians who are already familiar with this format. The following categories should be assigned: no disease (ND), complete response (CR), partial response (PR), stable disease (SD) and progressive disease (PD).

In contradistinction, the overall response of bone disease should be categorized on a scale of 1–5 indicating the likely overall response category: (1) highly likely to be responding, (2) likely to be responding, (3) stable, (4) likely to be progressing and (5) highly likely to be progressing.

Discordance or mixed response indicates the presence of progressing bone/soft tissue disease, not meeting definite progression criteria in the primary category, that is, when the majority of disease is stable or responding.

Discordant response should also be separately reported for primary, nodal, viscera and bone; evaluation of regional responses will enable the specific identification of the anatomic sites of mixed responses.

When discordant response is observed, the degree of discordance should be indicated major or minor to indicate in the evaluators opinion on whether alternative therapy options should be considered.

ADC value measurements should be made using a region-of-interest (ROI) technique on ADC images. Due to the lower spatial resolution of WB-MRI compared to CT scans, a 1.5 cm diameter threshold for bone lesions ROI is recommended for ADC measurements.

ADC measurements in bone disease should only be obtained from lesions that have sufficient signal intensity detected on all b-value images (including b0); otherwise the ADC values will be erroneous, reflecting only the noise in the images. Note that the absence of tissue signal on highest b-value images does not exclude tissues from ADC measurements because signal maybe present at lower b-values (thus, low or intermediate b-value images should be chosen instead for ROI placements).

Research components
Because of the need to unequivocally identify disease and to cope with the lower spatial resolution of WB-MRI compared to CT scans, a 1.5 cm diameter threshold for lesion size assessments is advised. Lesion size should be measured on anatomic T1-weighted images where possible.

Note that progression assignments for soft tissues, if based on measurements should be from baseline or the treatment induced summed measurement nadir, whichever is lower as per the RECIST v1.1 guidelines [7].

The type of progression (new disease versus growth of existing lesions) should be separately recorded; the location of progression can be accessible from the regional response assessments.

RACs at each time point should be compared to the baseline (pre-treatment) study for clinical use, but maybe referenced to the immediate prior study for research purposes if needed.

Whole-body tumor segmentations and histogram analysis are not part of the MET-RADS-P standard but can be used as ancillary tools if available (and are used in this paper for illustrative purposes only).

Worked up examples

An updated MET-RADS-P template form and detailed bone response assessment criteria can be found in Figure 1 and is available as a pdf document at www.siemens.com/magnetom-world.

Figures 2–4 illustrate the use of the MET-RADS-P standard in advanced, metastatic prostate cancer illustrated with examples of disease progression, responding and discordant responses.

The figures also demonstrate the utility of the WB-tumor load segmentation which is undertaken with the MR Total Tumor Load prototype, a released research software tool available on *syngo*.via Frontier (Siemens Healthcare,

Figure 3: Excellent response to chemotherapy
65-year-old male with metastatic castrate naive prostate cancer (mCNPC).
WB-MRI examinations before and after 4 cycles of docetaxel, goserelin and prednisolone therapy.

Figure 3A: There is improvement in the spinal canal narrowing in the mid-dorsal and lumbar spine on the T2W-FS images. The T1-weighted images are essentially unchanged or possibly minimally worse. There is also marked improved appearances of the bone and nodal disease on the paired WB b900 MIP images (inverted scale) and confirmed by significant increase in ADC values (see Figure 3C) of the bone lesions and reduction in size of the nodes.

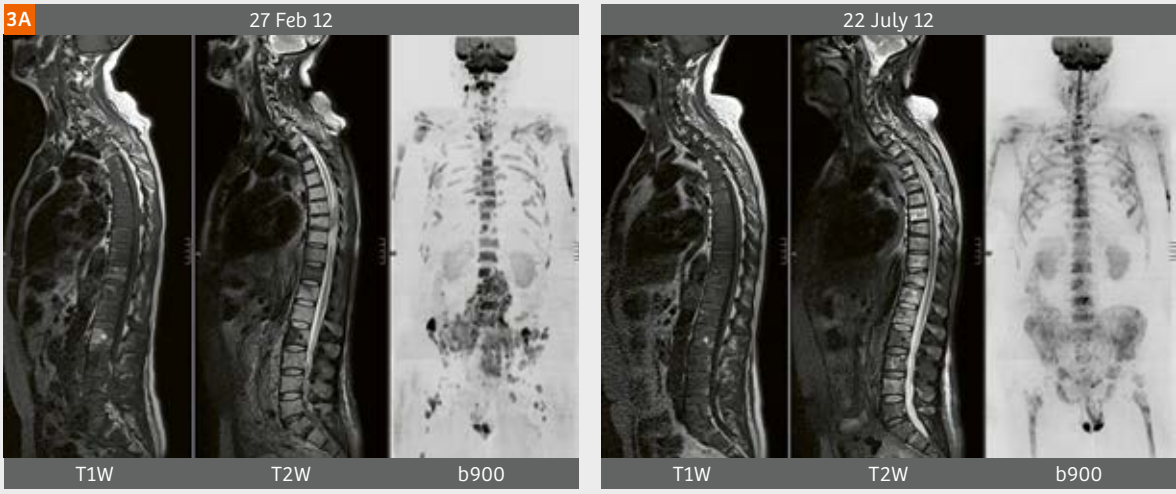

Figure 3B: Completed MET-RADS-P template report indicating sites of disease and RACs at each anatomical location compared to the baseline study. Note how the overall response at the primary tumor is indicated as no disease (previous radiotherapy). The overall pelvic nodal and retroperitoneal disease is excellent indicated as partial response (PR). The bone disease response is indicated by category 1 (highly likely to be responding).

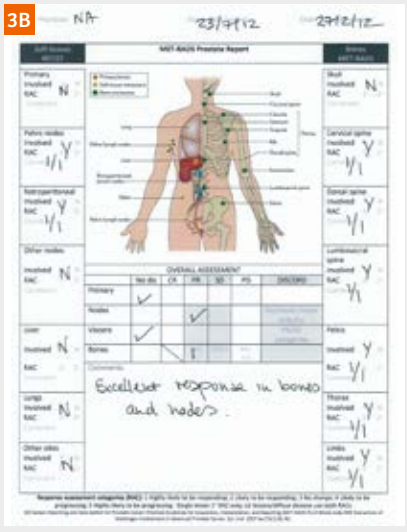

Figure 3C: WB-tumor load segmentation undertaken on *syngo*.via Frontier MR Total Tumor Load software (Siemens Healthcare; released research prototype – not part of the MET-RADS-P standard) for illustrative purposes only.

The whole-body b900 images are segmented using computed high b-value images of 1000 s/mm² and signal intensity threshold of approximately 30 AU. Extraneous signals (such as the brain, kidneys, bowel, gonads) are removed to leave only recognizable disease sites. The thresholded mask is overlaid with ADC value classes using the thresholds indicated and superimposed onto the b900 MIP images. The green voxels are values ≥1500 µm²/s (representing voxels that are 'highly likely' to be responding). The yellow voxels are set to lie between the 95th centile ADC value of the pre-treatment histogram (1067 µm²/s) and 1500 µm²/s thus representing voxels 'likely' to be responding. Red-voxels represent mostly untreated disease.

1281 mL of bone marrow and retroperitoneal nodal disease were segmented before therapy and 430 mL on therapy. Note that there is marked global increase in ADC values (705 µm²/s and 1635 µm²/s) on the corresponding relative frequency histograms. There is a marked decrease in excess kurtosis of the histograms (9.0 and -0.60). Note decreased extent and volume of red-voxels consistent with disease response (95% before therapy and 17% after therapy). The residual red regions on the post therapy scan are presumed to represent residual disease with low ADC values in the lower lumbar spine and in the left proximal femur.

Figure 4: Discordant response to Radium-223 therapy
55-year-old male with metastatic castrate resistant prostate cancer (mCRPC). Previously failed treatments include docetaxel chemotherapy and abiraterone. Previously lumbar spinal radiotherapy. WB-MRI scans were obtained before and after Radium-223 treatment. Symptomatically the patient is worse with increasing bone pain and has become blood transfusion dependent; however PSA values are improved from 792 ng/mL to 167 ng/mL thus creating diagnostic confusion on the effectiveness of Radium-223 therapy.

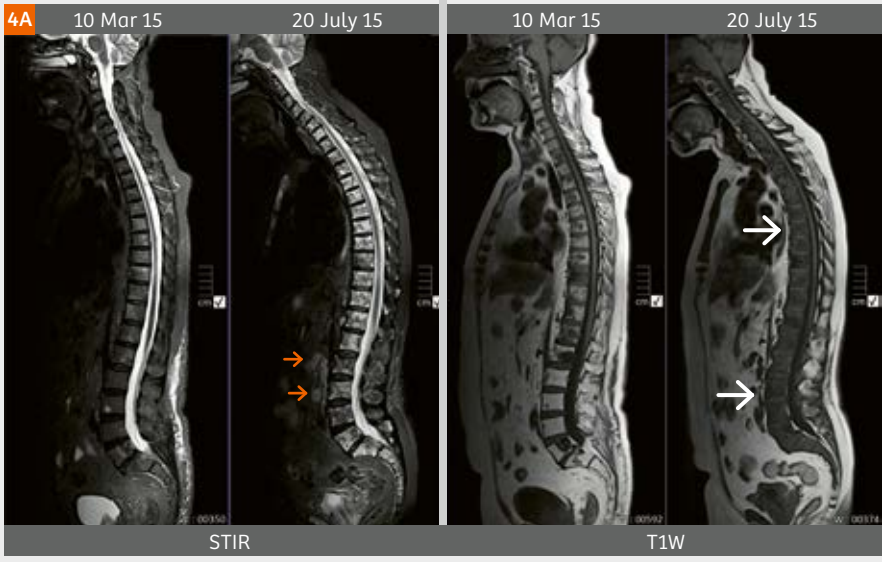

Figure 4A: T1-weighted spine images show increased abnormal signal in the cervical, dorsal and lumbosacral spine suggestive of disease progression using the criteria in Figure 1B. However, the STIR sequence shows higher signal intensities in the cervical and dorsal spine indicating increased tissue water. Note increase in size of retro-peritoneal nodes (orange arrows).

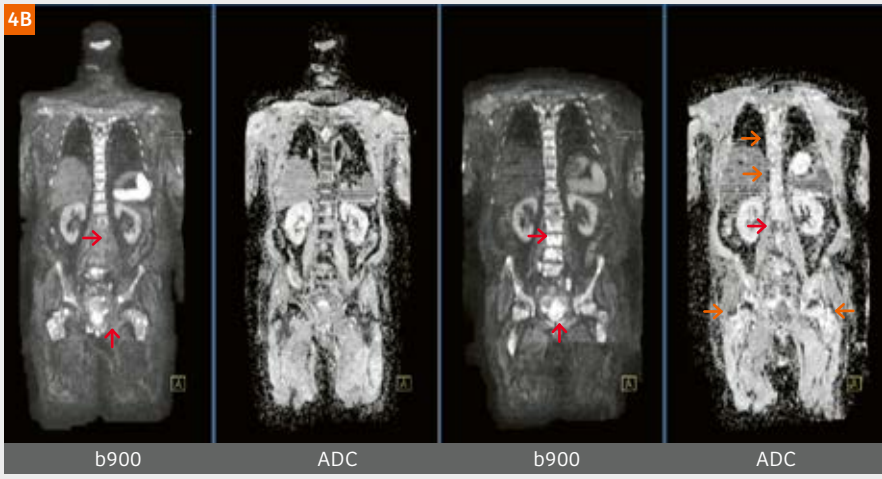

Figure 4B: Responding disease in femora & dorsal spine, new disease in lumbar spine
Coronal b900 and ADC maps show decreased b900 signal intensities and increased ADC values in the dorsal spine and proximal femora (orange arrows) indicating responding disease (T1w-pseudo-progression in the dorsal spine). However, the opposite is seen in the lumbar spine where b900 signal intensity is increased (red arrows) and with low ADC values indicating new disease (true progression). Note some enlargement of the primary prostate tumor also (vertical red arrows).

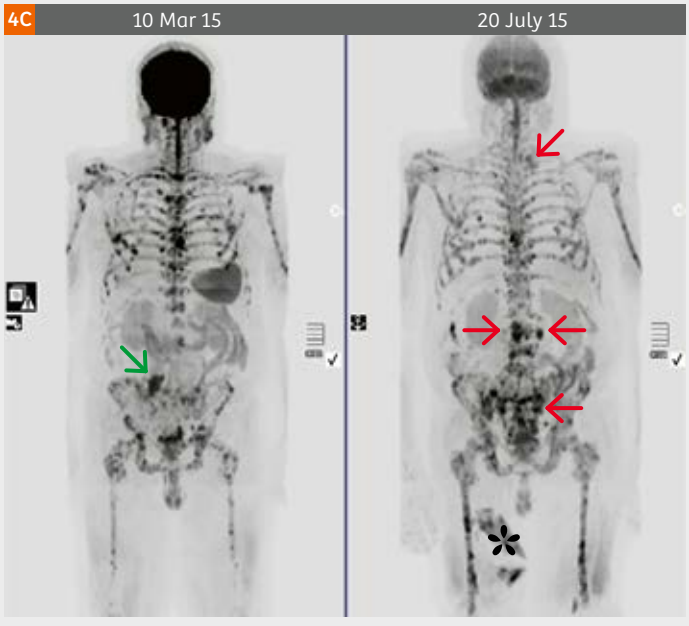

Figure 4C: Paired b900 MIP images (inverted scale) showing new nodal disease in the left hemipelvis, retroperitoneum and in the left supraclavicular fossa (red arrows). On the other hand, the enlarged lymph nodes in the right common iliac region is improved (green arrow). There seems to be an increase in extent of bone marrow signal intensity. The high signal geographic lesion over the right thigh on the follow-up examination is a dipper pad (*). Note lower signal intensity of the brain on follow-up examination due to the absence of the head coil.

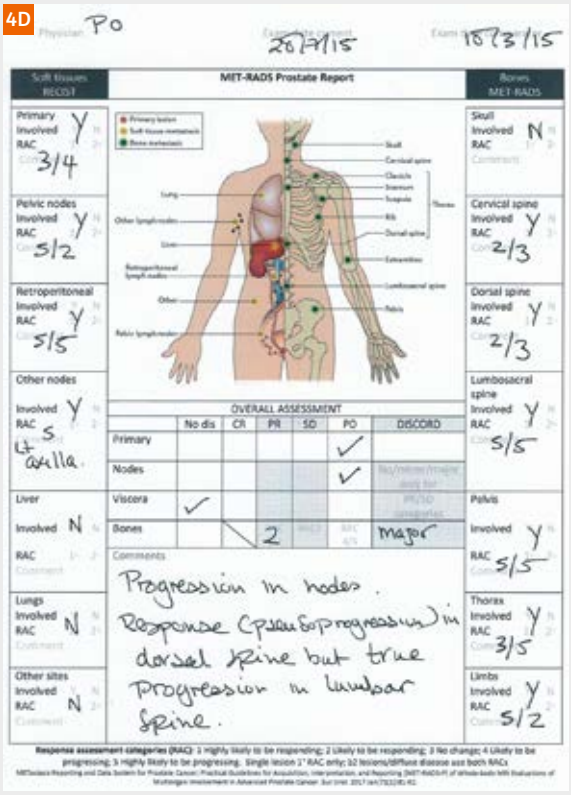

Figure 4D: Completed MET-RADS-P template report indicating sites of disease and RACs at each anatomical location compared to the baseline study. Note how the RAC of response at the primary tumor is mostly stable with some progression (RAC 3/4). The RAC of the pelvic nodes is indicated as 5/2 meaning that there is progression in the majority of the nodes although a single lymph node has responded (see also Figure 4E). Overall the bone disease is scored as 2 (likely to be responding in the majority of regions) with major discordance due to progression in lumbo-sacral spine and pelvis (both with RAC scores of 5/5).

Figure 4E: WB-tumor load segmentation undertaken on *syngo*.via Frontier MR Total Tumor Load software (Siemens Healthineers; released research prototype – not part of the MET-RADS-P standard) for illustrative purposes only.

The whole-body b900 images are segmented using computed high b-value images of 1000 s/mm² and signal intensity threshold of approximately 100 AU. Extra-neous signals (such as the brain, kidneys, bowel, gonads) are removed to leave only recognizable disease sites. The color the b900 MIP images are overlaid with ADC value classes using the thresholds indicated. The green voxels are values ≥1500 µm²/s (representing voxels that are 'highly likely' to be responding). The yellow voxels are set to lie between the 95th centile ADC value of the pre-treatment histogram (1208 µm²/s) and 1500 µm²/s thus representing voxels 'likely' to be responding. Red-voxels represent mostly untreated disease.

570 mL of bone marrow and nodal disease are segmented before therapy and 538 mL on therapy. Note that there is moderate global increase in ADC values (670 µm²/s and 920 µm²/s) on the corresponding relative frequency histograms. There is a decrease in excess kurtosis of the histograms (2.2 and -0.05). Note decrease extent and volume of red-voxels consistent with disease response (95% before therapy and 76% after therapy). Heterogeneity of response in the spine (more red voxels in the lumbar spine and more green voxels in the dorsal spine) and in the pelvis is appreciable on these color projected images. This heterogeneity of response emphasizes the need to evaluate all the relevant WB-MRI images and to apply regional responses using the MET-RADS-P criteria.

Erlangen, Germany; released research prototype). Note that tumor load and ADC histogram analysis is not part of the MET-RADS-P standard, and is included for illustrative and cross-correlations purposes only. Detailed working of the *syngo*.via Frontier MR Total Tumor Load software is described in an accompanying article by Robert Grimm and Anwar R. Padhani in this issue of MAGNETOM Flash.

Conclusions and future developments

The MET-RADS-P system provides the minimum standards for whole-body MR with DWI image acquisition, interpretation, and reporting of both baseline and follow-up monitoring examinations of men with advanced, metastatic prostate cancer. MET-RADS-P is suitable for guiding patient care in practice (using the regional and overall assessment criteria), but can also be incorporated into clinical trials when accurate lesion size and ADC measurements become more important (thus, recording of measurements is not mandated for clinical practice). MET-RADS-P enables the evaluation of the benefits of continuing therapy to be assessed, when there are signs that the disease is progressing (discordant responses).

MET-RAD-P requires validation within clinical trials initially in studies that assess the effects of known efficacious treatments, such as those targeting the androgen axis, cytotoxic chemotherapy, Radium-223 and PARP inhibitors. METRADS-P measures should be correlated to other tumor response biomarkers delineated by PCWG (such as PSA declines), quality of life measures, rates of skeletal events, radiographic progression free survival and overall survival. The latter will be needed for the introduction of WB-MRI into longer term follow-up studies that will allow objective assessments of whether WB-MRI is effective in supporting patient care. Thus, we recommend that MET-RADS-P is now evaluated in clinical care and trials, to assess its impact on the clinical practice of advanced prostate cancer.

References

1 Lecouvet FE. Whole-Body MR Imaging: Musculoskeletal Applications. Radiology. 2016;279:345–365.
2 Padhani AR, Lecouvet FE, Tunariu N, et al. Rationale for Modernising Imaging in Advanced Prostate Cancer. Eur Urol Focus. European Association of Urology; 2016;44:198–205.
3 Dimopoulos M a., Hillengass J, Usmani S, et al. Role of magnetic resonance imaging in the management of patients with multiple myeloma: a consensus statement. J Clin Oncol. 2015;33:657–664.
4 Padhani AR, Lecouvet FE, Tunariu N, et al. METastasis Reporting and Data System for Prostate Cancer : Practical Guidelines for Acquisition , Interpretation , and Reporting of Whole-body Magnetic Resonance Imaging-based Evaluations of Multiorgan Involvement in Advanced Prostate Cancer. Eur Urol. European Association of Urology; 2017;71:81–92.
5 Mottet N, Bellmunt J, Bolla M, et al. EAU-ESTRO-SIOG Guidelines on Prostate Cancer. Part 1: Screening, Diagnosis, and Local Treatment with Curative Intent. Eur Urol. 2016;1–12.
6 Cornford P, Bellmunt J, Bolla M, et al. EAU-ESTRO-SIOG Guidelines on Prostate Cancer. Part II: Treatment of Relapsing, Metastatic, and Castration-Resistant Prostate Cancer. Eur Urol. 2016;1–13.
7 Eisenhauer EA, Therasse P, Bogaerts J, et al. New response evaluation criteria in solid tumours: revised RECIST guideline (version 1.1). Eur J Cancer. 2008/12/23. 2009;45:228–247.
8 Scher HI, Morris MJ, Stadler WM, et al. Trial Design and Objectives for Castration-Resistant Prostate Cancer: Updated Recommendations From the Prostate Cancer Clinical Trials Working Group 3. J Clin Oncol. 2016;34:1402–1418.

Contact

Professor Anwar R. Padhani
MB, BS, FRCP, FRCR
Paul Strickland Scanner Centre
Mount Vernon Hospital

Rickmansworth Road
Northwood, Middlesex HA6 2RN
United Kingdom
anwar.padhani@stricklandscanner.org.uk

Contact

Nina Tunariu
MD MRCP FRCR MDR
Royal Marsden NHS Foundation Trust &
Institute of Cancer Research
Cancer Research UK Cancer Imaging Centre

Downs Road, Sutton, Surrey, SM2 5PT
United Kingdom
Nina.Tunariu@icr.ac.uk

Visit us at
www.siemens.com/magnetom-world
to download the MET-RADS-P template form.

Whole-body Diffusion-weighted MR Image Analysis with *syngo*.via Frontier MR Total Tumor Load

Robert Grimm[1], Anwar R. Padhani[2]

[1] Siemens Healthineers, Erlangen, Germany
[2] Paul Strickland Scanner Centre, Mount Vernon Hospital, Northwood, Middlesex, UK

Whole-body diffusion-weighted MRI has recently gained a lot of attention as a promising technique for the assessment of multifocal bone disease such as multiple myeloma and bone metastases from breast and prostate cancer [1–3]. Compared to other imaging techniques, diffusion-weighted MRI has a high sensitivity and specificity for disease detection, without exposing the patient to ionizing radiation. Uniquely, diffusion imaging also enables therapy response to be evaluated, with particular application for bone disease. However, one challenge is the relatively large effort in response interpretation, due to the number of images that are generated and the lack of tools for efficient evaluation for multifocal disease.

This limitation was addressed by an efficient analysis approach that has been proposed by Blackledge et al. [4], using a threshold-based segmentation on diffusion-weighted images to identify regions of disease. Based on this segmentation, the overall tumor volume as well as histogram metrics of the corresponding apparent diffusion coefficient (ADC) maps are analyzed. Excellent inter- and intra-observer agreement of this computed approach was demonstrated recently in a pilot study [5].

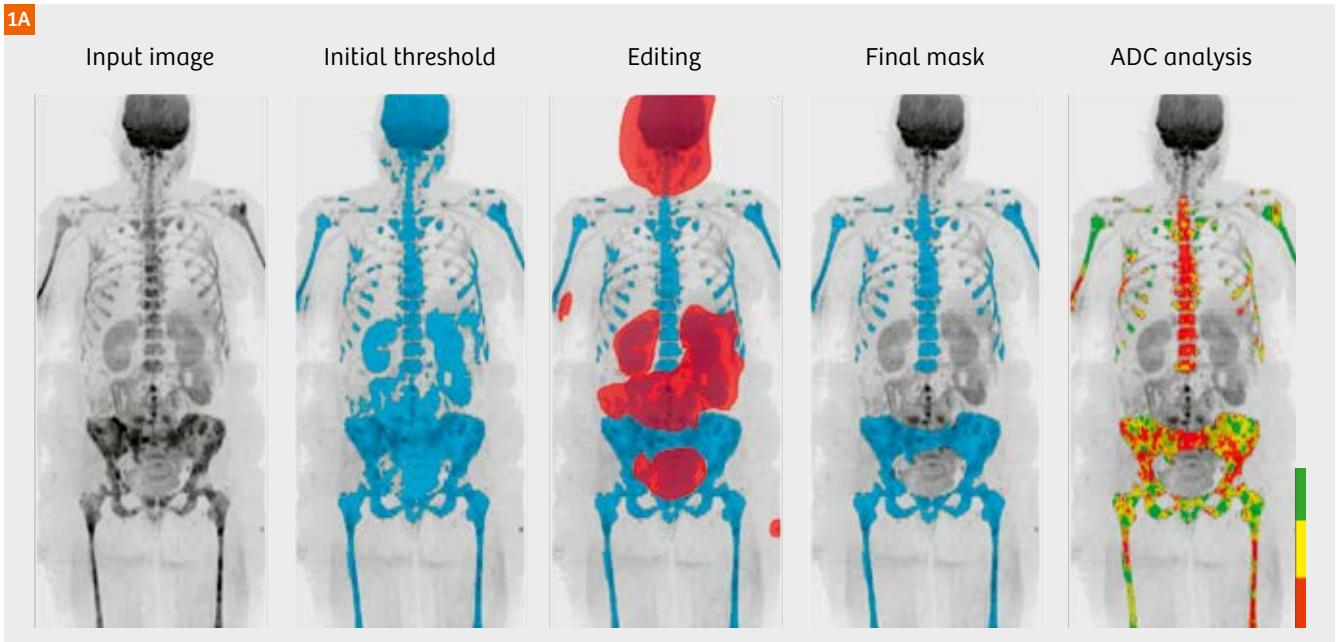

Figure 1: Application workflow. A computed high b-value image (b = 800 s/mm²) serves as input. An initial segmentation of the multiple myeloma lesions is obtained by thresholding and then edited to manually exclude regions from the analysis. In this case the brain, neck nodes, salivary glands, kidneys, spleen, and pelvic bowel were removed. Furthermore, the lower lumbar spine was removed, because of artifacts from a spine stabilization. Finally, back-mapping analysis reveals the ADC associated with each voxel, and provides detailed ADC histogram metrics (see also Figure 2).

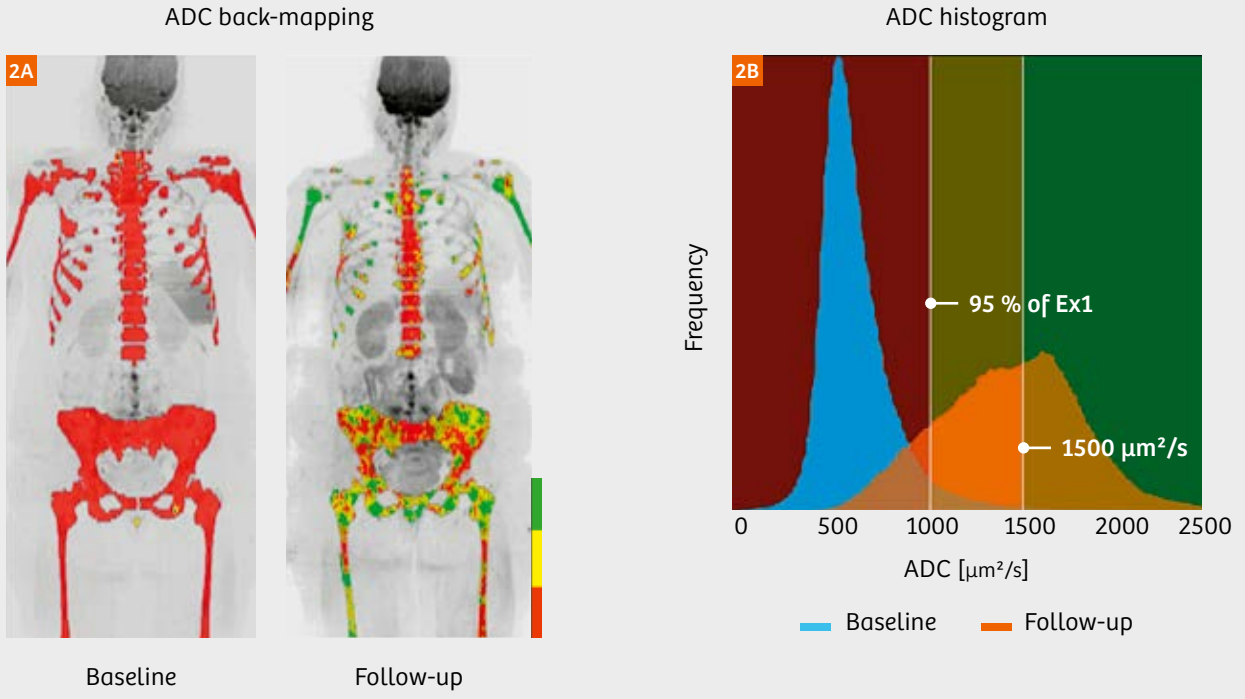

Figure 2: Example result for a multiple myeloma patient before and after one cycle of ESHAP (etoposide, methylprednisolone, cytarabine and cisplatin) therapy. The ADC back-mapping **(2A)** indicates reduced tumor burden and region based responses by yellow and green overlays. The ADC histograms **(2B)** show a significant change due to the treatment. The ADC statistics show reduced active tumor volume, increased mean and median ADC, and decreased ADC skewness and kurtosis. While 94.5% of the segmented volume were in the ADC range associated with active tumor at baseline, only 13.8% of the volume at follow-up were in the same range (ADC < 1000 µm²/s). Conversely, the fraction of the data in the ADC range associated with tumor cell kill (ADC > 1500 µm²/s) has increased from 0.9% at baseline to 44.7% on the follow-up study.

Quantitative whole-body diffusion MRI is implemented in the *syngo*.via Frontier MR Total Tumor Load[1] released research prototype: It uses diffusion-weighted images as input and allows creation of a 3D mask on diffusion images, for the analysis of the corresponding ADC maps. The prototype supports evaluation of up to two time-points, side-by-side and utilizes maximum intensity projections (MIPs) to facilitate efficient visual assessment of the intermediate result at each step. The workflow is structured in three steps, as depicted in Figure 1. The example illustrates the processing steps for a patient with multiple myeloma:

1. **Initial segmentation:** An initial mask is defined interactively by applying a threshold to a computed high b-value image (for example, b = 800 s/mm²). An automatic outlier removal can be performed to reduce false positive voxels due to artifacts or T2 shine-through.
2. **Mask editing:** The initial mask is edited by the user. The user can perform volume punching in order to exclude artifact regions and normal hyperintense organs such as brain, kidneys, spleen, testes, salivary glands etc, or users can choose to retain only a selected volume of interest. Furthermore, a volumetric, semi-automatic segmentation tool is available for manually adding false negative regions to the mask if not already captured.

Metric	Baseline	Follow-up
Volume [cm³]	1298	978
ADC mean [µm²/s]	653	1432
ADC median [µm²/s]	609	1437
ADC skewness	2.11	0.12
ADC e. kurtosis	8.21	0.07
% Low	94.5	13.8
% High	0.9	44.7

Table 1: Segmentation statistics. The tumor volume as well as several histogram metrics have changed significantly during treatment.

[1] *syngo*.via Frontier is for research only, not a medical device.

3. **Analysis:** The ADC histogram and corresponding statistics are computed for the edited masked volume. Histogram metrics include mask volume, mean, median, standard deviation, skewness, excess kurtosis, and customizable percentiles.

   Regions of low, intermediate and high ADC values can be inspected interactively by adjusting slider positions on the histogram. Depending on the ADC chosen, the colored back-mapping ADC overlays allow the visual discrimination of regions with untreated disease (typically associated with lower ADC values) compared to disease regions that have been treated effectively (high ADC values).

In the example shown in Figure 2, the 95th percentile of the baseline examination, approximately 1000 µm²/s, was used as lower ADC threshold and 1500 µm²/s was used as upper threshold. The ADC back-mapping in Figure 2A shows a red overlay for voxels with an ADC below 1000 µm²/s, a yellow overlay for voxels in the intermediate range, and a green overlay for voxels above 1500 µm²/s. The corresponding histograms and limits are shown in Figure 2B. The patient shows changes consistent with a significant response to the therapy, indicated by the emergence of mixed yellow and green regions in the humeri, pelvis, and femur. However, red regions continue to be seen indicating the continued presence of untreated disease.

The histogram statistics, listed in Table 1, show a reduction of the total diffusion volume, from 1298 cm³ at baseline to 978 cm³ at follow-up, and a radical change in the histogram shape. The mean and median values have increased from 653 (609) µm²/s at baseline to 1432 (1437) µm²/s in the follow-up examination. The skewness decreased from 2.11 to 0.12, while the excess kurtosis decreased from 8.21 to 0.07.

Further examples obtained with the *syngo*.via Frontier MR Total Tumor Load[1] released research prototype software can be found in the article *"Metastatic Prostate Cancer in Practice – the MET-RADS-P Imaging Response System Using Whole-body MRI"* on page 64 and in the case study *"Observing Endocrine Therapy Resistance in Metastatic Breast Cancer with Whole-body MRI"* on page 80 of this issue of MAGNETOM Flash.

To summarize, the *syngo*.via Frontier MR Total Tumor Load released research prototype provides an efficient and reproducible workflow with quantitative results for the processing and analysis of whole-body diffusion-weighted images in the response assessment setting. It is a promising tool to support the standardization of whole-body MRI for treatment response monitoring of bone disease in particular. Extensions like a fully automatic bone segmentation (as described in *"Whole-body MRI Reading and Bone Assessment with syngo.via Frontier MR Bone Scan"* on page 76 in this issue), simultaneous consideration of other MR parameters such as the normalized signal intensity, fat fraction, or Gadolinium enhancement fraction [6, 7], and integrated classification techniques to detect and separate regions of discordant response [7], may further add to the potential of the technique to promote high-precision medicine.

References

1 Pawlyn C, Fowkes L, Otero S, et al. Whole-body diffusion-weighted MRI: a new gold standard for assessing disease burden in patients with multiple myeloma? Leukemia. 2016;30(6):1446-1448. doi:10.1038/leu.2015.338.

2 Padhani AR, Lecouvet FE, Tunariu N, Koh DM, De Keyzer F, et al. (2016) Rationale for Modernising Imaging in Advanced Prostate Cancer. European Urology Focus, Available online. doi:10.1016/j.euf.2016.06.018.

3 Padhani AR and Tunariu N, Metastatic response system in using whole body MRI for prostate cancer in practice. See also page 76 in this issue of MAGNETOM Flash.

4 Blackledge MD, Collins DJ, Tunariu N, Orton MR, Padhani AR, et al. (2014) Assessment of Treatment Response by Total Tumor Volume and Global Apparent Diffusion Coefficient Using Diffusion-Weighted MRI in Patients with Metastatic Bone Disease: A Feasibility Study. PLOS ONE 9(4): e91779. doi: 10.1371/journal.pone.0091779.

5 Blackledge MD, Tunariu N, Orton MR, Padhani AR, Collins DJ, et al. (2016) Inter- and Intra-Observer Repeatability of Quantitative Whole-Body, Diffusion-Weighted Imaging (WBDWI) in Metastatic Bone Disease. PLOS ONE 11(4): e0153840. doi: 10.1371/journal.pone.0153840

6 Amlani A, Ghosh-Ray S, van Ree K, Makris A, D'Sa S, Ostler P, Anyamene N, Padhani AR. Relationships Between Diffusion Weighted Signal Intensity, ADC and Water/fat Content of Malignant Bone Marrow. Program Number: 3447. Proceedings of the International Society of Magnetic Resonance in Medicine. 20th Scientific Meeting and Exhibition, Salt Lake City, May 2013.

7 Blackledge MD, Leach M, Rata M, Tunariu N, Koh DM, et al. (2016) Visualizing whole-body treatment response heterogeneity using multi-parametric magnetic resonance imaging. Journal of Algorithms & Computation Technology, in press. doi: 10.1177/1748301816668024.

Contact

Robert Grimm, Ph.D.
Siemens Healthcare GmbH
HC DI MR PI TIO ONCO

Postbox 32 60
91050 Erlangen
Germany
Phone: +49 (0) 9131 84-2717
robertgrimm@siemens.com

First Clinical Experiences with Simultaneous Multi-Slice Accelerated Diffusion-Weighted Imaging Throughout the Body

Valentin Tissot, M.D.[1]; Olivier Legeas, M.D.[1]; Isabelle Kergastel, M.D[1]; Erwan Derrien[2]; Gregor Thörmer, Ph.D.[3]

[1] Morvan Hospital, Centre Hospitalier Regional Universitaire (CHRU), Brest, France
[2] Siemens Healthineers, La Chapelle-sur-Erdre, France
[3] Siemens Healthineers, Erlangen, Germany

Case 1

60-year-old female patient with multiple lesions at the cortico-medullary junction in the brain.

Figure 1A–B: T2 FLAIR and T1w post-contrast image show a lesion in the left temporal lobe with surrounding edema and moderate mass effect. The central cavity of the lesion is hyperintense and surrounded by a thin capsule. In postcontrast images the lesion shows a 'target sign' with rim enhancement and central hyperintensity.

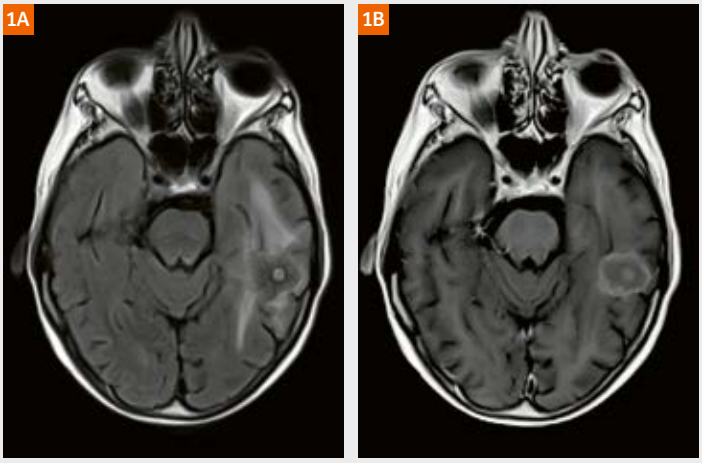

Figure 1C–F: DWI at the same level demonstrates a target lesion, with high signal intensity in b1000 **(1C, E)** and corresponding lowered ADC **(1D, F)**, reflecting very strong diffusion restriction (mean ADC ~ 400 mm^2/s) in the central part of the lesion, consistent with a highly viscous abscess formation. While 1C and D were acquired with standard parameters (see Table 1), images 1E and F were acquired with an SMS factor of 2, which allowed to reduce the TR from 5600 ms to 2700 ms. Accordingly, the overall acquisition time was shortened from 1:54 min to 1:11 min without compromising image quality.

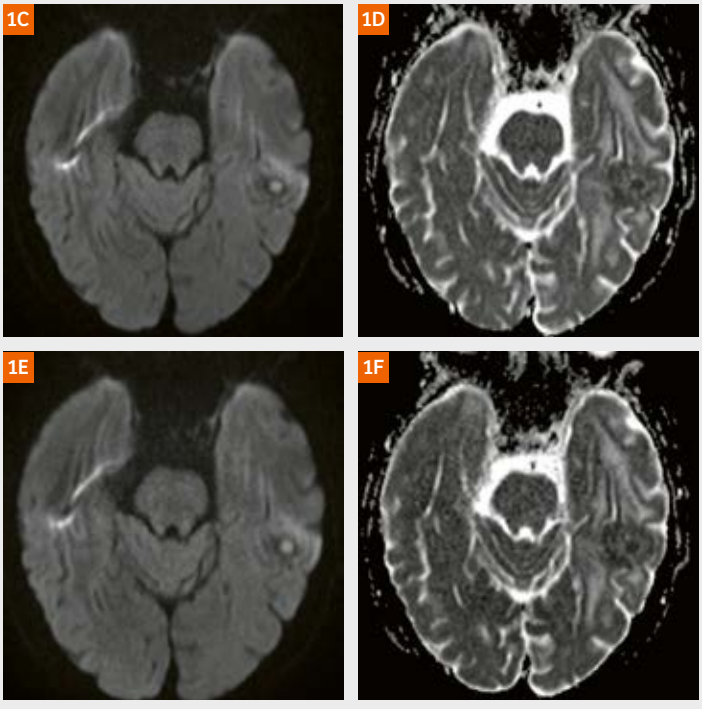

Introduction & Motivation

The service spectrum of our radiology department and medical imaging center at the Hôpital Morvan comprises multidisciplinary diagnostic and interventional activities, with a focus on visceral imaging, neuroradiology, vascular imaging as well as musculoskeletal imaging. To serve both in- and outpatient referrals of different medical disciplines we are, amongst others, equipped with two Magnetic Resonance Imaging (MRI) systems of which one is a MAGNETOM Avanto^{fit}, 1.5T scanner.

Running on *syngo* MR E11C software, this system facilitates a new method for advanced and accelerated diffusion-weighted imaging (DWI), namely Simultaneous Multi-Slice (SMS) imaging, which is of tremendous value for our daily clinical work. DWI has become an integral part not only of neuro imaging studies but also imaging of the head & neck region, breast, liver, prostate, rectum and so forth. Especially in body oncology, DWI can be used as a sensitive tool to identify potential areas of impeded diffusion on high b-value images and to improve lesion characterization in terms of cellular properties with the Apparent Diffusion Coefficient (ADC).

Case 2

72-year-old male patient with mass tumor in the right submandibular space.

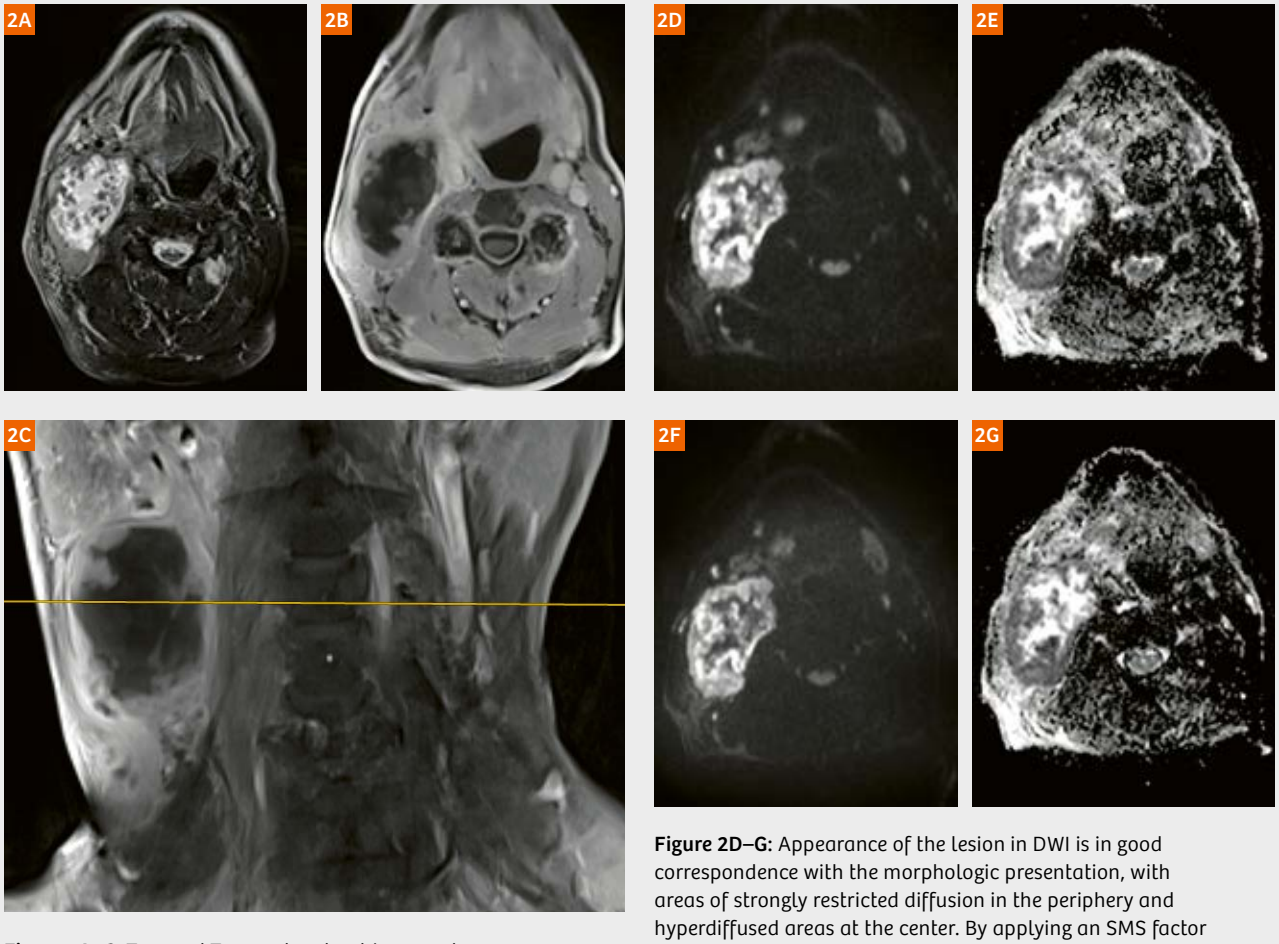

Figure 2A–C: T2w and T1w postcontrast images show an extended, oval-shaped, inhomogeneous imposing mass in the right submandibular space, displacing the trachea and major cervical vessels towards medial. The tumor presents with solid, nodular appearing areas in the parietal part and shows T2w hyperintensity in the more centrally located aspects, consistent with fluid accumulation due to necrosis. T1w postcontrast images show rim like enhancement of the tumor and advanced infiltration of the musculus sternocleidomastoideus, lingual area, platysma and tongue are present.

Figure 2D–G: Appearance of the lesion in DWI is in good correspondence with the morphologic presentation, with areas of strongly restricted diffusion in the periphery and hyperdiffused areas at the center. By applying an SMS factor of 2, it was possible to reduce the TR from 4300 to 2200 ms and the overall acquisition time from 4:18 min to 2:12 min (further parameters in Table 1).

Case 3

33-year-old woman with invasive breast cancer of the left breast.

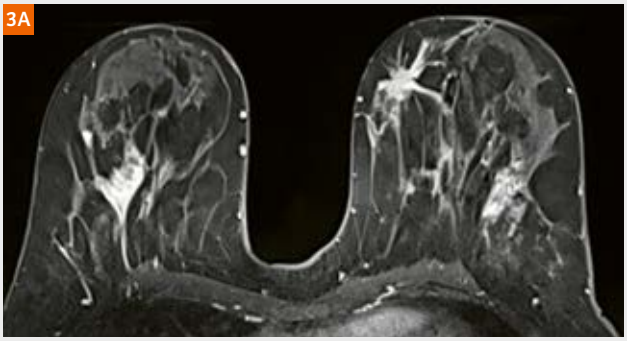

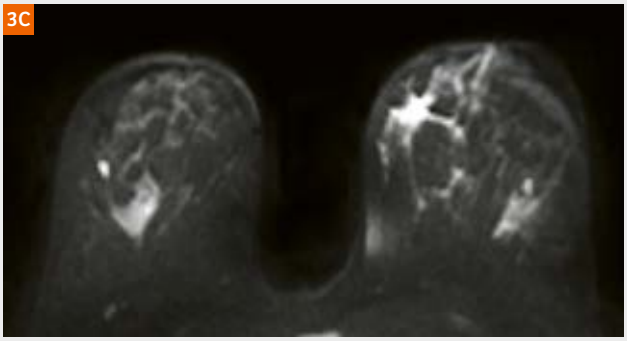

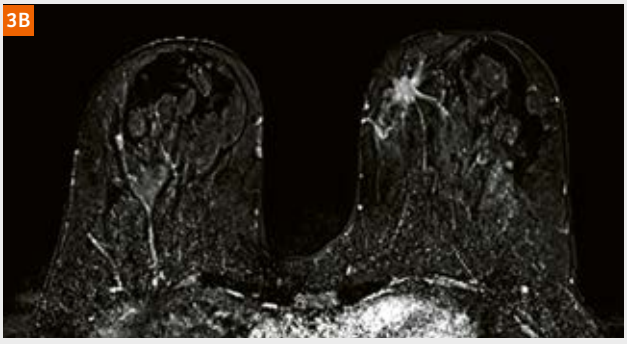

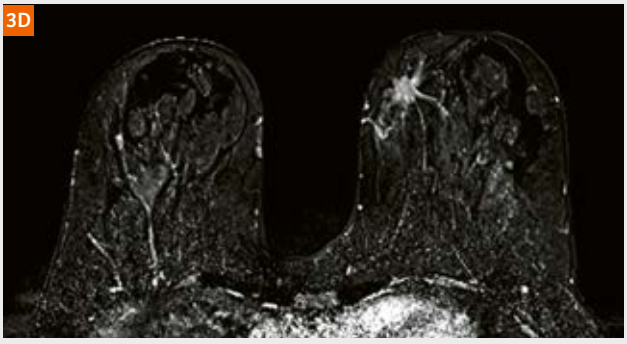

Figure 3A–B: First postcontrast T1w image of the dynamic contrast-enhanced series and respective subtraction view clearly show a lesion in the left breast, demonstrating fast enhancement and subsequent washout. The mass is irregular shaped, spiculated and homogenously enhancing. In the right breast, wedge-shaped, moderate enhancement of the glandular tissue and a small lenticular lesion can be found.

Figure 3C–D: SMS accelerated DWI at the same level shows a hyperintense area in the left breast in b1000 with corresponding ADC restriction and a mean ADC value of 865 x10^{-3} mm^2. The small, round, well circumscribed lesion in the right breast manifests as a T2 shine-through effect in the high b-value image with corresponding high ADC value, most likely corresponding to a fibroadenoma. Acquisition parameters can be found in Table 1.

Region		Field-of-View [mm]	Matrix	Slice thickness [mm]	#slices	TR /TE [ms]	*b-values* [s/mm²]	PAT factor	SMS factor	Acquisiton time [min]
Brain	Conv	230x230	384x384i	4	26	5600 / 84	0, 1000	2	0	1:54
	SMS					2700 / 84		2	2	1:11
Head & Neck	Conv	230x230	384x384	4	24	4300 / 106	50, 800	2	0	4:18
	SMS					2200 / 106		2	2	2:12
Breast	SMS	203x339	108x180	4	26	2600 / 84	50, 800	2	2	3:08
Prostate	Conv	200x200	128x128	3.5	18	3400 / 72	50, 800	2	0	4:58
	SMS					2000 / 72		2	2	2:55
Rectum	SMS (axial)	200x200	128x128	4	24	2400 / 72	50, 400, 800	2	2	2:24
	SMS (sag)	200x200	128x128	4	20	2100 / 79	50, 800, 1600	2	2	3:30

Table 1: Acquisition parameters

Case 4

68-year-old man with prostate cancer.

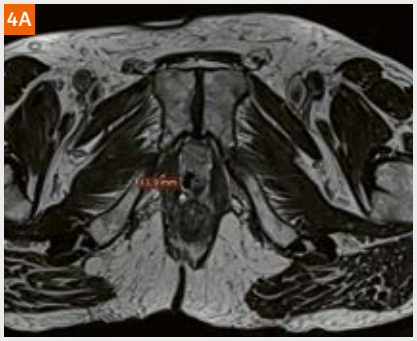

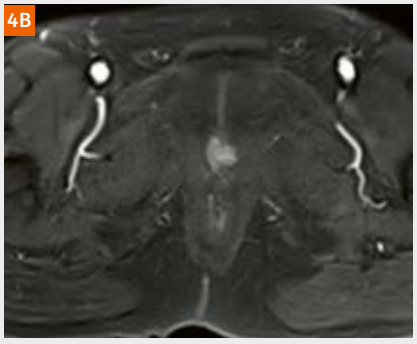

Figure 4A–B: T2w images show a benign hyperplasia of the transition zone of the prostate in accordance with the patient's age. In the apex of the gland, however, a lenticular shaped, T2 hypointense lesion with irregular margins and a maximum diameter of ~13 mm is visible. Early phase T1w images after contrast application show a distinct, well circumscribed enhancement of contrast medium in the respective area.

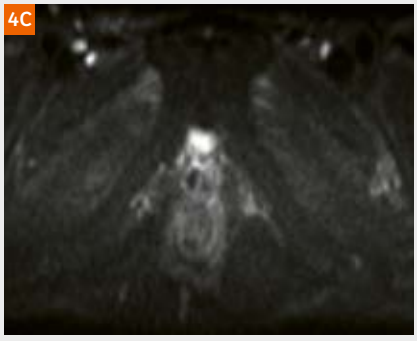

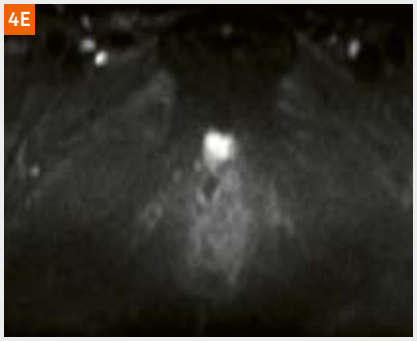

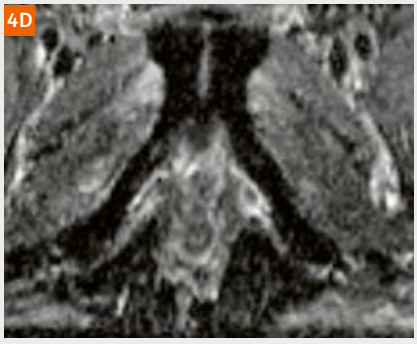

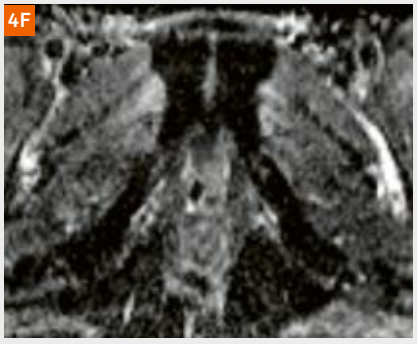

Figure 4C–F: Conventional **(4C, D)** and SMS accelerated **(4E, F)** high b-value image and ADC map show an apical lesion with strongly restricted diffusion. Measured ADC values show a high inter-method reproducibility with values of 758 and 744 x 10^{-3} mm^2/s, respectively. With Simultaneous Multi-Slice acceleration, acquisition time could be reduced from 4:58 min to 2:55 min (further parameters in Table 1).

Figure 4G–H: Due to the unusual position of the lesion an additional DWI scan with a very high b-value of 1600 s/mm^2 was performed in the sagittal plane, which confirmed the suspicion and was rated PI-RADS 4.

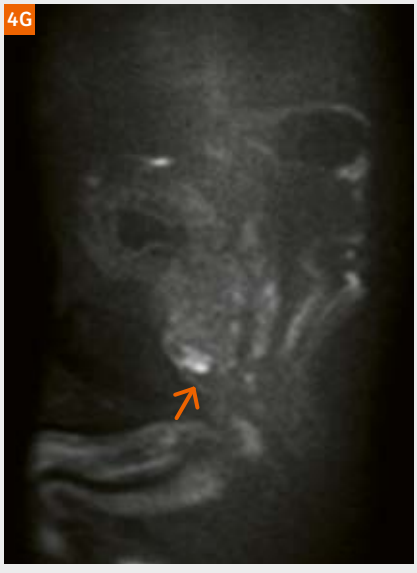

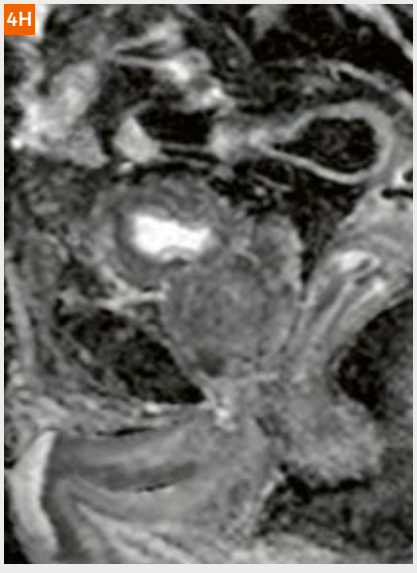

Case 5

65-year-old male patient with sigmoid carcinoma.

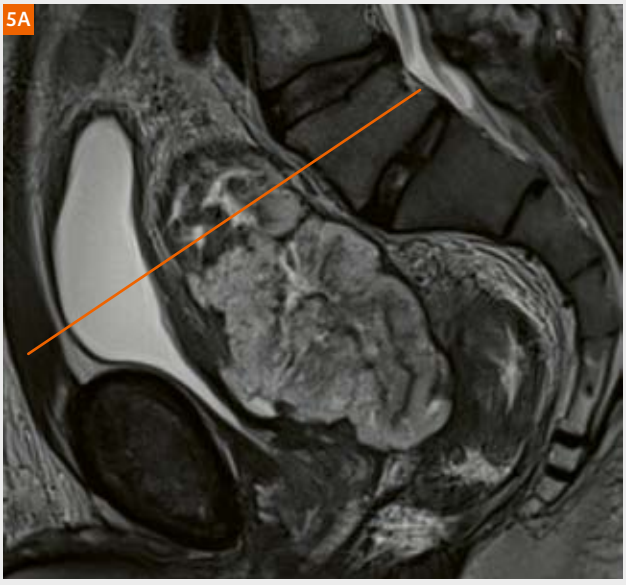

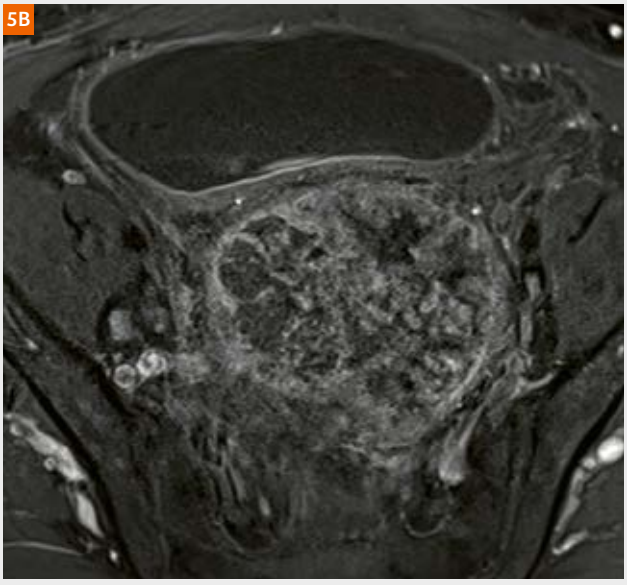

Figure 5A–B: T2w images show a hyperintese, regularly structured mass in the pelvis, most probably originating from the sigma. Towards caudal, the tumor touches the seminal vesicles or potentially infiltrates these. Metastatis of lumbar vertebra 4 and iliac lymph nodes are likely to be present. In postcontrast T1 images, the tumor shows irregular, enhancement from parietal aspects towards the center.

Figure 5C–F: Corresponding sagittal **(5C, D)** and axial **(5E, F)** diffusion-weighted images (b800) and ADC maps show a very inhomogeneous pattern in the tumor corresponding to the anatomical appearance and with aspects, especially towards cranial and in the center, showing strongly restricted diffusion.

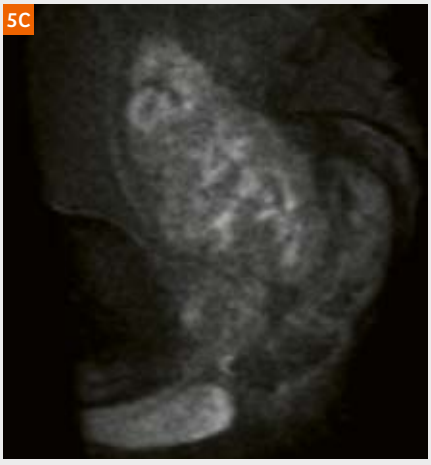

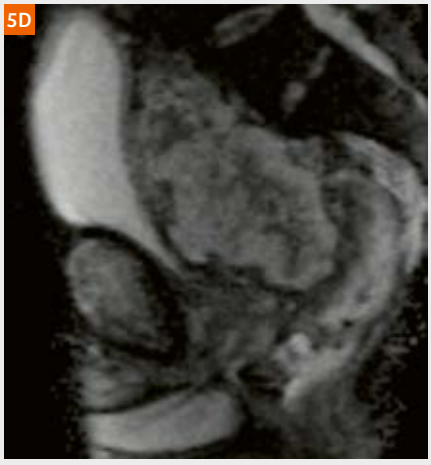

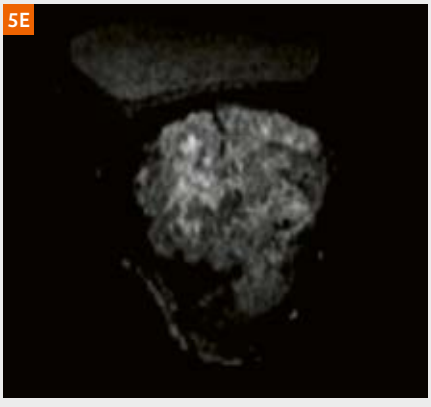

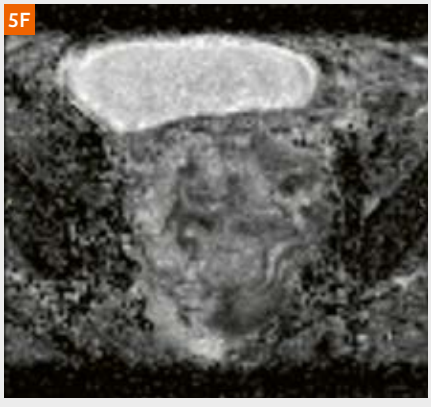

Technically, however, DWI is commonly based on a single-shot, 2D EPI sequence, which is a highly inefficient approach of image acquisition. Every imaging slice has to be excited individually, then the diffusion encoding gradients are played out and finally the image information is acquired with EPI encoding [1]. This process is repeated multiple times, once for each imaging slice, until the entire volume of interest is covered. This inefficient approach can be overcome with Simultaneous Multi-Slice. Instead of a successive excitation of slices, slices are exited simultaneously with a multiband pulse and blipped-CAIPIRINHA SMS-EPI ensures preservation of high SNR and low artifact levels [2].

Motivated by the promising results with Simultaneous Multi-Slice accelerated abdominal imaging presented by the NYU group [3], we decided to evaluated the benefits of Simultaneous Multi-Slice beyond neuro imaging and started to set up own protocols for imaging of various body regions with the support of our local application specialist.

6

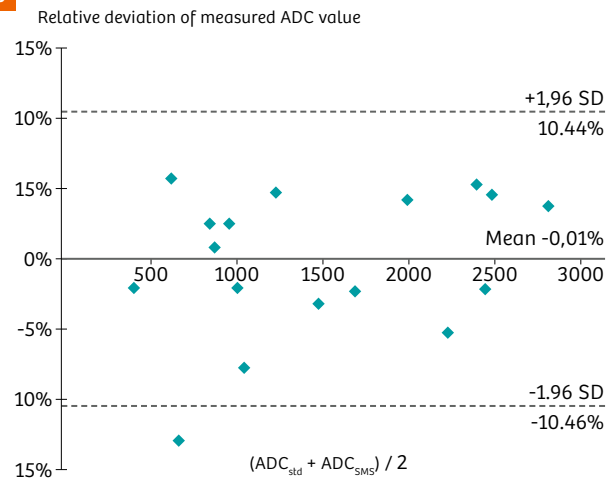

Figure 6: Bland-Altman-Diagram showing that ADC values are highly reproducible between the conventional and the accelerated technique.

Summary and Conclusion

As demonstrated with the cases presented here, Simultaneous Multi-Slice acceleration is a valuable technique for the acceleration of diffusion-weighted imaging in almost all clinical applications where DWI is commonly applied. Robust results and good image quality can be achieved with an SMS factor of 2, which allows to achieve near two-fold acceleration in DWI acquisitions. As shown in the Bland-Altman-Diagram (Fig. 6), ADC values are highly reproducible between the conventional and the accelerated technique.

In the meantime we have incorporated Simultaneous Multi-Slice Diffusion-weighted Imaging (SMS DWI) with 2-fold acceleration in our clinical protocol for various body regions, allowing shorter overall scan time, better slice coverage or improved resolution.

References

1 Setsompop K, et al. Advancing Diffusion MRI Using SMS EPI. MAGENTOM Flash 3(63): 2015; 16-22.
2 Breuer F, et al. CAIPIRINHA – Revisited. MAGENTOM Flash 3(63): 2015; 8-15.
3 Chandarana H, et al. Simultaneous Multi-Slice Accelerated Free-Breathing Diffusion-Weighted Imaging in Abdomen and Pelvis. MAGENTOM Flash 3(63): 2015; 32-35.

Contact

RValentin Tissot, M.D.
Morvan Hospital
Centre Hospitalier Regional Universitaire (CHRU)

2 Avenue Foch
29609 Brest cedex
France
Phone: +33 298223333
valentin.tissot@chu-brest.fr

GRASP: Tackling the Challenges of Abdominopelvic DCE-MRI

Kai Tobias Block
NYU Langone Medical Center, New York, USA

Learn more about Compressed Sensing in Body MRI at

www.healthcare.siemens.com/magnetic-resonance-imaging/magnetom-world/hot-topics/compressed-sensing

MAGNETOM Flash – Imprint

Publisher:
Siemens Healthcare GmbH
Magnetic Resonance,
Karl-Schall-Str. 6, D-91052 Erlangen, Germany

Editor-in-chief:
Antje Hellwich
(antje.hellwich@siemens-healthineers.com)

Editorial Board:
Reto Merges; Wellesley Were;
Sunil Kumar S.L., Ph.D.;
Gary R. McNeal, MS (BME)

Review Board:
Gregor Thörmer, Ph.D.; Berthold Kiefer, Ph.D.;
Peter Gall, Ph.D.; Hans Weber, Ph.D.

Production:
Norbert Moser,
Siemens Healthcare GmbH

Layout:
Agentur Baumgärtner,
Friedrichstr. 4, D-90762 Fürth, Germany

Printer:
Schmidl & Rotaplan Druck GmbH,
Hofer Str. 1, D-93057 Regensburg, Germany

We welcome your questions and comments about the editorial content of MAGNETOM Flash. Please contact us at magnetomworld.med@siemens.com.

Manuscripts as well as suggestions, proposals and information are always welcome; they are carefully examined and submitted to the editorial board for attention. MAGNETOM Flash is not responsible for loss, damage, or any other injury to unsolicited manuscripts or other materials. We reserve the right to edit for clarity, accuracy, and space. Include your name, address, and phone number and send to the editors, address above.

MReadings: Prostate MRI is also available online:

www.siemens.com/magnetom-world

Not for distribution in the US

On account of certain regional limitations of sales rights and service availability, we cannot guarantee that all products included in this brochure are available through the Siemens sales organization worldwide. Availability and packaging may vary by country and is subject to change without prior notice. Some/All of the features and products described herein may not be available in the United States.

The information in this document contains general technical descriptions of specifications and options as well as standard and optional features which do not always have to be present in individual cases, and which may not be commercially available in all countries.

Due to regulatory reasons their future availability cannot be guaranteed. Please contact your local Siemens organization for further details.

Siemens reserves the right to modify the design, packaging, specifications, and options described herein without prior notice. Please contact your local Siemens sales representative for the most current information.

Note: Any technical data contained in this document may vary within defined tolerances. Original images always lose a certain amount of detail when reproduced.

Siemens Healthineers Headquarters
Siemens Healthcare GmbH
Henkestr. 127
91052 Erlangen
Germany
Phone: +49 9131 84-0
siemens.com/healthineers

Published by Siemens Healthcare GmbH · Order No. A91MR-1100-90C-7600 · Printed in Germany · PS MR 5104 09170.075 ·